MODELING AND DESIGN OF INTRA-CAVITY FREQUENCY DOUBLED GREEN LASERS

MODELING AND DESIGN OF INTRA-CAVITY FREQUENCY DOUBLED GREEN LAERS

By

QINGYANG XU, B.S., M.E.

A Thesis
Submitted to the School of Graduate Studies
in Partial Fulfillment of the Requirements
for the Degree
Doctor of Philosophy

McMaster University

DOCTOR OF PHILOSOPHY (2011)
(Engineering Physics)

McMaster University
Hamilton, Ontario

TITLE: Modeling and Design of Intra-cavity Frequency Doubled Green Lasers

AUTHOR: Qingyang Xu
B.A. (McMaster University),
M.E. (Institute of Semiconductors, Chinese Academy of Sciences)

SUPERVISOR: Professor Chang-Qing Xu
Professor Xun Li

NUMBER OF PAGES: xii, 102

ABSTRACT

This thesis is an exploration of numerical modeling and design of intra-cavity frequency doubled green lasers, which is one of the three key light sources in laser display systems.

In this thesis the time-domain traveling wave (TDTW) model, which is well developed to model integrated photonic devices, is derived for modeling and design of a new proposed device. The device is based on the intra-cavity frequency doubling of high power distributed Bragg reflector laser diodes (DBR-LD) and MgO-doped periodically poled lithium niobate (MgO:PPLN) waveguides. The numerical modeling and design suggest the superiority of the proposed intra-cavity frequency doubled DBR-LD/MgO:PPLN green laser over traditional single-pass frequency doubled DBRLD-LD/MgO:PPLN green laser.

A plane-wave based coupled-wave model is implemented to model miniature intra-cavity frequency doubled DPSS lasers. Good agreement between the plane-wave model and experiment has been obtained. By employing the plane-wave model, we have explained the phase problem in our optical contact Nd:YVO_4/MgO:PPLN green laser. Design examples of wide temperature operation of Nd:YVO_4/MgO:PPLN green lasers are also completed by this numerical method.

Finally, to model high power bulk intra-cavity frequency doubled diode-pumped solid-state (DPSS) green lasers, a three-dimensional coupled-wave model is developed and compared with experimental results. A two-dimensional thermal model is incorporated into the three-dimensional coupled-wave equations to model thermal lensing and thermal de-phasing effects in intra-cavity frequency doubled DPSS lasers. The numerical models we developed are validated by the experimental results.

Acknowledgements

I would like to express my gratitude to my supervisor, Professor Chang-Qing Xu, for providing me with the opportunity to work in the area of nonlinear optics and for his expert guidance and invaluable assistance throughout the course of my doctoral studies. If not for his support I likely would not have completed the doctoral program. I am fortunate to have had him as my supervisor.

I would also like to express my gratitude to my co-supervisor, Professor Xun Li, for his guidance in numerical modeling. Without his insight, knowledge and patience, the thesis would not have been possible. I would like to thank my other committee members, Professor Shiva Kumar and Professor Qiyin Fang, for their generous help and valuable suggestions.

I wish to thank Dr. Xu's former group members, Dr. Hong-Gang Yu, Dr. Bo Chen, Dr. Jian Yang and Jorge Fonseca Campos, Joh Markle, who have helped me a lot since I joined the group five years ago. Special thanks should be given to Dr. Hong-Gang Yu, who has passed his research experience and research spirit to me when I stated the program at McMaster. I would also like to give special thanks to Dr. Wanguo Liang, who I have been working with for more than five years. His encouragement and enthusiasm has always inspired me throughout my research work. I would like to thank the current group members in Dr. Xu's group: Ben Watts for his help in preparation of journal papers, Yi Gan, Jian Sun for their help in my research; and Dr. Yang Lu for his unselfish sharing and discussing during the experiments.

I would never have been able to complete my thesis without the love and support of my family. I would like to thank my wife: thank you. For the past five, and most difficult years of my doctoral studies, you have been my strongest supporter. Our little daughter is the best gift you gave me. Finally thank my parents for their unconditional support and love.

Contents

List of Tables

List of Figures

CHAPTER 1

INTRODUCTION

1.1 Introduction

Since the invention of the first Ruby laser (light amplification by stimulated emission of radiation) a half-century ago [1], the laser industry has grown rapidly. Lasers have met various industrial and scientific application needs with their versatile wavelength ranges, operation modes and power levels. Visible lasers are generally considered as the "ultimate" light sources for display applications due to their high brightness, high directionality and high color saturation [2-5]. In particular, the vast potential demand from the optoelectronic display industry in recent years has pushed the fast development of red, green and blue (RGB) lasers used as replacements of the traditional light sources. It is promising that a new generation of laser display systems such as mobile projector, laser TV, and laser cinema will bloom in the near future, according to a recent market analysis [5]. Red laser diodes (LD) lasing around 630 nm based on AlGaInP material system have been developed [6, 7]. Since their first demonstration in 1996 [8] blue laser diodes are getting matured. Development of green laser diodes, which share the same material with blue LD, is still at its infancy stage. In addition to applications in the display system, highly efficient and high power continuous wave (CW) green lasers have also attracted attention from other fields such as bio-photonics and undersea communications [2]–[5].

This thesis focuses on the numerical modeling and design of intra-cavity frequency doubled (IC-FD) green lasers using several different technical approaches. In this chapter, we review two state-of-the-art approaches to generate green light, GaN semiconductor laser diodes and frequency doubled solid-state lasers, and make comprehensive comparisons between these technologies.

1.2 Development of Green Lasers

1.2.1 GaN Green Laser Diodes

Semiconductor laser [9, 10] material system has been widely investigated since the 1960s. A wide band gap semiconductor material system, GaN/AlN/InN, can cover the wavelength from 200-nm to 650-nm. While GaN based violet and blue LDs are commercially available, there are several technical problems for developing green laser diodes by increasing the indium content of the InGaN. The first problem is the choice of substrate. GaN single-crystal substrate is an ideal one, however, the growth of GaN crystal is rather demanding. Second, high concentration p-doping in the GaN material is a difficult task [11]. Third, increasing the indium content in the InGaN quantum well will shift the lasing wavelength towards green, but the material growth by the metal organic chemical vapor deposition (MOCVD) is challenging [8, 11-14].

The research and development of green laser diodes are in rapid progress. In 2009 Sumitomo reported the longest wavelength (531 nm, pulse mode) for green with rather low electrical-optical (EO) efficiency (<1%) [13]. Now several research groups and companies reported lasing wavelength from 510 to 525 nm with slightly better performance [12-15]. On the other hand, at high power level, blue broad area LD (BALD) at 445 nm can deliver 1W by Nichia [16], and there are no reported results for high power green laser diodes to date.

1.2.2 Green Lasers by Means of Frequency Doubling

(a) Solid-State Lasers

For visible light generation, traditional solid-state laser materials can not fit this wavelength range well. Alternatively, nonlinear optical technology gives an indirect way to obtain wavelengths that are not covered by solid-state lasers. The first nonlinear optical phenomenon, namely second-harmonic generation (SHG) or frequency doubling (FD) through crystalline quartz, was observed by Franken [17] in 1961 soon after the first laser of the world. However, due to the second or higher order nonlinear effect, the optical frequency conversion efficiency is relatively low. Inserting a nonlinear optical crystal into the laser cavity is a highly efficient frequency conversion method as compared with the external cavity frequency conversion [18, 19].

To generate green light by means of single-pass frequency doubling (single-pass FD) or intra-cavity frequency doubling (IC-FD), an infrared laser emitting at 1064 nm is required. Diode pumped solid-state laser (DPSS laser) such as Nd:YAG and Nd:YVO_4 emit at 1064 nm. Using FD crystals, such as $KTiOPO_4$ (KTP), LiB_3O_5 (LBO) and periodically poled lithium niobate (PPLN), high power

and highly efficient green light has been generated [20-25]. Table 1.1 shows the specifications of widely used nonlinear crystals [26].

Recently, due to the success of fabrication of PPLN, FD by such promising materials is in rapid progress. A 12 W green light power was achieved with a Nd:YVO_4 planar waveguide laser array intra-cavity frequency doubled by MgO doped PPLN (MgO:PPLN) [22]. A single green emitter of 1.5 W was obtained with bulk intra-cavity frequency doubled Nd:YVO_4/MgO:PPLN laser pumped with a 3W 808 nm LD [23]. A 6 W green light was reported by a 20 W fiber pigtailed pump LD module [24].

Table 1.1. Comparison between widely used nonlinear optical crystals. [26]

	MgO:PPLN	KTP	LBO
Phase-matching type	QPM e+e→e	XY plane, $\theta=90^0$, $\varphi=23.5^0$ o+e→e(type II)	XY plane, $\theta=90^0$, $\varphi=11.4^0$ o+o→e (type I)
Effective nonlinear coefficient	16-22 pm/V	3.2 pm/V	0.96 pm/V
Photorefractive damage threshold	>2 MW/cm^2	Not clear	No
Optical absorption	0.004 cm^{-1}@1064 0.02 cm^{-1}@532	<0.006 cm^{-1}@1064 <0.02 cm^{-1}@532	0.0035 cm^{-1}
Thermal conductivity	4.6 W/m/K	3 W/m/K	3.5 W/m/K
Temperature tolerance	2.1 °C/cm	25 °C/cm	6.2 °C/cm
Transparency wavelength range	0.34~4.5 μm	0.35~4.5 μm	0.155~3.2 μm
phase matching range	Full transparent range	0.994~3.4 μm	0.551 ~ 3.23 μm
Walk-off angle	No	4.5	7
Green induced infrared absorption	Yes	Yes	No
Output Polarization	High	Change with T	High

(b) High Power Edge Emitting Semiconductor Lasers

High power InGaAs/GaAs lasers, originally developed as pump sources for Er and Yb doped fiber lasers, can emit from 900 nm to 1100 nm. The single-pass

FD technology has made blue-green laser covering 450 nm to 550 nm possible [27]. For efficient single-pass FD with bulk or waveguide nonlinear optical crystals, high power and high brightness semiconductor lasers and high efficiency nonlinear crystal are required. Fig. 1.1 is a schematic single-pass frequency doubled green laser, where a distributed Bragg reflector laser diode (DBR-LD) is amplified by a taper section, forming a master oscillator power amplifier (DBR-MOPA). The nonlinear crystal is a bulk PPLN.

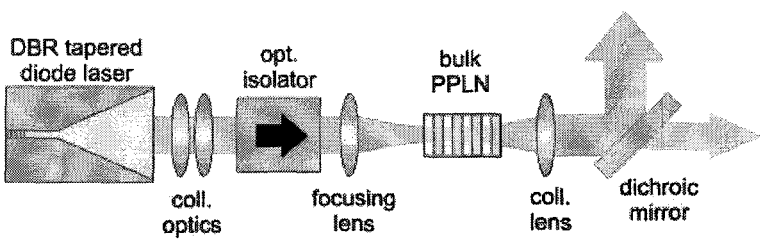

Fig. 1.1. Single-pass FD of DBR/MOPA with a bulk PPLN crystal [27]. Copyright Wiley-VCH Verlag GmbH & Co. KGaA. Reproduced with permission.

Single-pass FD of edge emitted semiconductor lasers by MgO:PPLN is under active development in recent years [28,29]. With a 30 mm long PPLN crystal, green output power up to 1.5 W was achieved by the DFB-MOPA technology with fundamental power of 7 W [29].

Optical waveguides formed on the periodically poled nonlinear optical crystals are also used for the single-pass FD of semiconductor lasers. Corning Inc. has made progress on high power distributed feedback laser diode (DFB-LD) and DBR-LD [30-34]. They reported that by using a 12 mm long MgO:PPLN ridge waveguide, 417 mW (>70%) of the high power DBR-LD was coupled into the waveguide by a pair of aspherical lenses, generating 304 mW green, corresponding to a conversion efficiency of 72.9% in the waveguide [33].

However, single-pass FD of semiconductor lasers suffers from complicated design problems, including low coupling efficiency from the semiconductor laser to the nonlinear crystal ridge waveguide, mechanical instability, long nonlinear crystal, and narrow temperature tolerance.

(c) Optical Pumped Semiconductors

A third configuration of green lasers is based on the IC-FD of optical pumped semiconductors (OPS), or so-called vertical extended cavity semiconductor emitting lasers (VECSEL) [35-39]. This concept combines the

merits of solid-state lasers and semiconductor lasers, by using a bulk semiconductor quantum well as the gain medium and a solid-state laser cavity. High modal gain of the specially designed periodically resonant gain (PRG) [35, 36] results in an extremely high absorption of the pump light with only μm-thick gain region. The quantum well structure of the PRG will absorb the pump light with a rather large wavelength tolerance while the bulk cavity structure will function similar to traditional solid-state lasers and extract more SH powers than the semiconductor laser frequency doubled lasers. Today IC-FD of OPS has generated 13 W in blue (using LBO) [37], 7 W in green (using BBO) [38], and 5 W (using LBO) in yellow [39].

Electrically pumped VESEL developed by Novalux (they call it NECSEL, Fig. 1.2) [40] has a further advantage that this devices is electrically injected and has potentially high EO efficiency. By neglecting the optical pump, where usually about 40% of the pump laser's EO efficiency is wasted, a direct electrical injection will increase the total EO efficiency if the carrier injection is well designed and fabricated. However, the injection area of the NCSEL cannot be scaled for larger fundamental mode operation, because the larger injection area will result in non-uniform distributions of the injected carriers and multimode optical field. In such multimode cavity the IC-FD process will not be as efficient as in a single mode cavity. However, by fabricating the two-dimensional NECSEL array, high power red, green and blue of 3 W each has been reported [41].

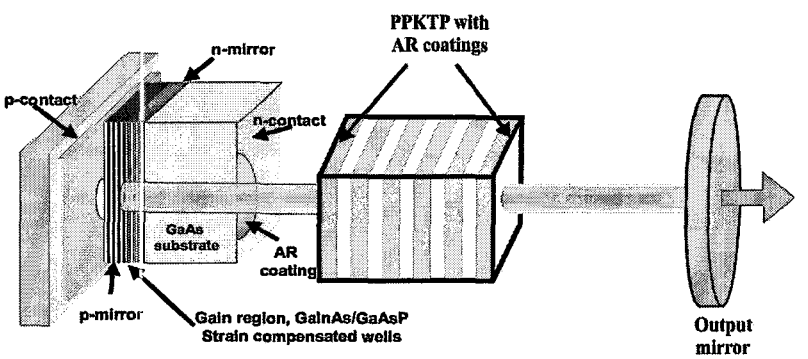

Fig. 1.2. Electrically pumped VECSEL structure [40]. Copyright OSA. Reproduced with permission.

Disadvantages of VECSEL structure include critical PRG design and growth, very high DBR mirror reflectivity growth, and heat dissipation in the active region under high power operation [37].

(d) IC-FD of Edge Emitting Semiconductor Lasers

A fourth method is to introduce the IC-FD concept into the high power semiconductor lasers. This can also combine the merits of semiconductor gain medium and IC-FD with nonlinear optical waveguides. However, historically little work has been done by this method, especially in green. This is partially due to the unavailability of laser diode emitting at 1060 nm. In 1993, Laurell [42] first used a grating stabilized narrow stripe diode laser emitting at 853 nm and a 5-mm long PPKTP waveguide to generate 1.35 mW blue light. Yamamoto et al. adopted a similar Littrow grating configuration. By placing a PPLT waveguide crystal between the grating and the diode laser, they were able to generate blue light with an average power of 4.5mW at a wavelength of 428 nm and an opto-optical conversion efficiency exceeding 13% in pulse mode [43]. Recently, IC-FD of 1060 nm high power broad area laser diode bar [44] has been reported. With a 10 mm MgO:PPLN bulk crystal, they generated 1.31 W green by a 49-emitter laser bar operated at 45 A (35W pump power).

The main concern for the IC-FD of semiconductor laser was argued as the LD facet loading [27]. When the fundamental power is resonated for the IC-FD structure, the light intensity is so high that the LD facet may be degraded and damaged. With today's advanced fabrication process of high power laser diode, this issue may be alleviated. We will discuss the facet loading issue in Chapter 3 in more details.

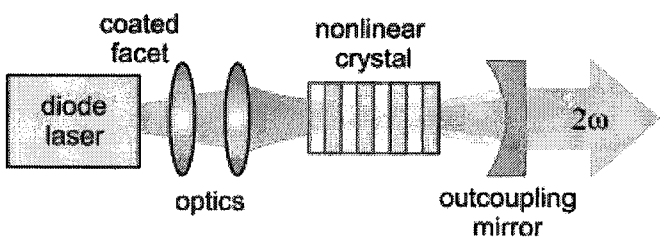

Fig. 1.3. Intra-cavity frequency doubling of semiconductor lasers [27]. Copyright Wiley-VCH Verlag GmbH & Co. KGaA. Reproduced with permission.

1.2.3 Brief Summary

Table 1.2. Comparison of green lasers with different technologies.

	GaN LD	IC-FD of DPSS	Single-pass FD of LD	IC-FD of OPS	IC-FD of LD

Power	50-100 mW N.A.	100 mW >10 W	300 mW 1.6 W	100 mW >10 W	N.A. 1.3 W
Wavelength	<532 nm N.A.	532 nm	530 nm	532 nm	532 nm
Beam quality	Elliptical Expect bad	Excellent Excellent	Good N.A.	Excellent Fair	Good N.A.
Efficiency	1-3% N.A.	15% >20%	10-15% <10%	5-10% <20%	10-20% 1%
Cost	N.A. High	Low Low	Fair High	Fair High	Fair High
Volume	Smallest N.A.	Small Large	Medium N.A.	Small large	Small Large
Noise	Low Low	Medium Medium	Low N.A.	Low Low	Low N.A.

In order to get a clear idea about current state-of-the-art technologies for generation of green laser light, we summarize in Table 1.2 the key device specifications at low power (upper row) and high power levels (lower row) in each cell. Each technology has advantages and disadvantages and it seems not clear which one would finally dominate in the future. IC-FD of DPSS lasers and IC-FD of LD technologies have comparative advantages in terms of cost and efficiency, which initiates our research.

1.3 Introduction to Lithium Niobate [45]

The widely explored nonlinear crystal that can achieve QPM is lithium niobate. Lithium niobate, a popular nonlinear optical crystal in the field of nonlinear optics, was developed in the 1960's. It is a ferroelectric crystal belonging to trigonal system (3m point group). Fig.1.4 shows the crystal structure of $LiNbO_3$ +c and –c polarizations. Lithium ions (Li^+) are sited at the upper or lower side of the center of the oxygen triangles. Commercially available crystals are "poled" so that all of the lithium ions are sited at the same side (Fig.1.4) and therefore they have spontaneous polarization Ps. The lithium ion has an electric charge, which can be shifted to the other side by applying external electric field E anti-parallel to Ps. The portion of the crystal where the ions are shifted is called a

domain inversion (180^0 domain reversal). Domain inversion is associated with inversion of the spontaneous polarization and crystallographic c and y axes. The

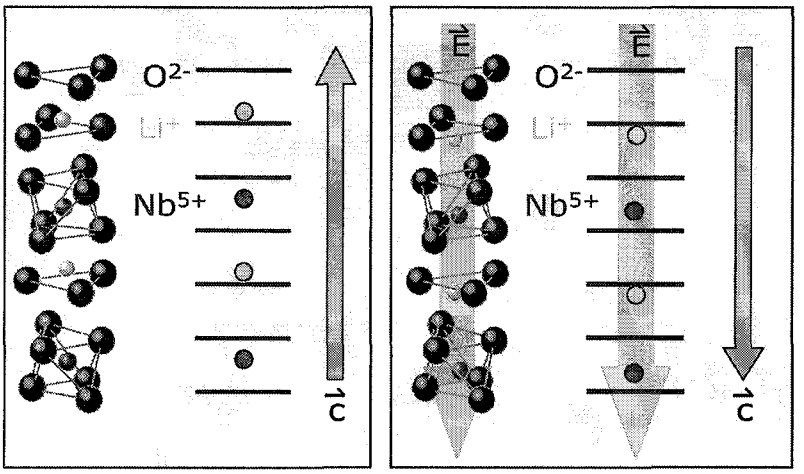

Fig. 1.4. Atomic lattice structure of lithium niobate, showing spontaneous polarization along +c (left) and (-c) (right) axis, respectively. (Adopted from www.photonik.uni-bonn.de/Papers/talks/080624_Buse.pdf)

sign of nonlinear optical coefficient is inverted simultaneously with the inversion of spontaneous polarization. Thus the domain inversion provides the possibility of producing quasi-phase matched gratings, as will be discussed in Chapter 2.

The widely used congruent $LiNbO_3$ crystal with the congruent composition Li_2O:Nb_2O_5 is around 48.5:51.5, where a few percent of Li site is substituted by Nb (antisite-defect) [46]. These non-stoichiometric defects will cause the photorefractive damage problem and can be significantly reduced with MgO doping of the crystal (typically 5 mol%) [47]. Anxuxother method to reduce defect density is to grow stoichiometric crystals by double-crucible Czochralski method [48].

1.4. Research Motivation

The urgent demand of high efficient, high power green lasers is the main motivation of designing and developing new compact green lasers. As is seen from the summary above, on the low power application side, the most straightforward method except direct InGaN LDs is FD of semiconductor lasers. Since IC-FD is an efficient method for frequency conversion, the method of IC-FD of semiconductor lasers is an elegant solution. Therefore designing an IC-FD

green laser with advanced nonlinear crystal is one motivation of this thesis. As will be shown in Chapter 3, we design such a green laser composed of a high power DBR-LD and a MgO:PPLN waveguide. Furthermore, numerical modeling with time-domain traveling wave (TDTW) method demonstrates the advantages of the proposed device over the traditional single-pass FD devices.

Intra-cavity frequency doubled DPSS lasers, which can be miniaturized with optical contacting technology, and can generate high power with bulky components, are candidates for both low power and high power green lasers. By employing the advanced nonlinear optical materials such as MgO:PPLN, the performance of the bulk green lasers has been experimentally investigated widely. However, how to accurately model intra-cavity frequency doubled DPSS lasers and design such lasers with the aid of numerical models, have not been well developed yet. This thesis attempts to model and design intra-cavity frequency doubled green lasers by numerical methods.

1.5 Main Contributions of Thesis

This research has the following contributions:

1. General time-domain traveling wave (TDTW) equations are implemented and extended to investigate a new type green laser: intra-cavity frequency doubled DBR-LD/MgO:PPLN green laser. Based on the numerical model derived, we complete the optimized design of such device and demonstrate its superiority in generating 530 nm green light as compared with current technologies.

2. A plane-wave based coupled-wave model is derived to describe simple intra-cavity frequency doubled DPSS lasers. The model is validated with experimental results and allows us to explain the phase problem present in optical contact Nd:YVO_4/MgO:PPLN green lasers.

3. To model bulk intra-cavity frequency doubled solid-state lasers, a three-dimensional (3D) coupled-wave model is implemented. The 3D model gives more detailed information on the optimal design of such lasers. Furthermore, a two-dimensional (2D) thermal model is incorporated into the 3D coupled-wave model to demonstrate the thermal lensing and thermal de-phasing effects involved in intra-cavity frequency doubled DPSS lasers.

1.6 Thesis Outline

This thesis is organized into six chapters. The first chapter provides the motivation and contribution of this research work. A brief introduction of green laser technologies and lithium niobate is also presented. Starting from the Maxwell equations, Chapter 2 gives detailed derivations of the governing equations discussed in the following chapters of the thesis. Chapter 3 extends the TDTW model to simulate frequency doubled DBR-LD/MgO:PPLN green lasers, and a new intra-cavity frequency doubled DBR-LD/MgO:PPLN green laser is proposed. The optimization design and comparison is made with available single-pass frequency doubled DBR-LD/MgO:PPLN green lasers. Chapter 4 derives a plane-wave based coupled-wave method to model optical contact Nd:YVO_4/MgO:PPLN green lasers. Phase problem in optical contact Nd:YVO_4/MgO:PPLN green lasers has been investigated and explained theoretically by this model. Several green laser design examples for the wide temperature operation are also demonstrated by this numerical model. In Chapter 5 a full 3D coupled-wave model and 2D thermal model are derived to model intra-cavity frequency doubled Nd:YVO_4/MgO:PPLN green lasers. Chapter 6 briefly concludes and outlines future work.

CHAPTER 2

THEORETICAL BACKGROUND AND GOVERNING EQUATIONS

2.1 Introduction

This chapter provides a basic theoretical background for intra-cavity frequency doubling (IC-FD) of lasers. We first review the numerical techniques required in modeling semiconductor lasers and solid-state lasers respectively. Next, the general time-domain traveling wave equations in optical nonlinear and gain media which are the governing equations in the following chapters are derived. Furthermore we introduce the concept of quasi-phase matching (QPM) in a nonlinear medium, especially in the widely used ferroelectric materials such as lithium niobate. Finally we describe the concept of intra-cavity second-harmonic generation briefly.

2.2 Numerical Techniques for Modeling Lasers

2.2.1 Modeling Semiconductor Lasers

Modeling active devices is much more time consuming than passive devices, since laser oscillation is usually needed for the field build-up in the laser cavity. For traditional passive photonic devices (optical waveguides, couplers and waveguide gratings) and advanced photonic devices, beam propagation method (BPM) [49] and finite-difference time-domain (FDTD) [49] techniques are well developed. Commercial simulators [50-52] are also available for the design and optimization of such devices. However, simulation design tools for active photonic devices, such as laser diode and other complex photonic integrated circuits [53], are not readily available due to the intrinsic complexity of active devices. In active photonic devices, optical field propagates and evolves in the laser cavity. Semiconductor energy band and the associated optical gain have to be calculated. In addition, carrier transportation and heat generation and

distribution in the active area should also be solved. All these modules are coupled such that a self-consistent solution can only be solved numerically [54].

In modeling the behavior of active photonic devices, the major interest is in their basic electrical-optical characteristics of the new device structures. Coupled-mode equations [55, 56] that describe wave propagating in both directions and coupling back and forth through some mechanism (for example Bragg grating feedback) are widely used for simple device modeling. Time-domain traveling wave (TDTW) equations [54] characterizing wave propagations in both time and space domain have the additional advantage of dynamic behavior modeling over the coupled mode equations, and therefore have broad applications in active device modeling [57-61].

2.2.2 Modeling Solid-State Lasers

For traditional solid-state lasers involving various cavity configurations, a Fresnel integral equation [62, 63] has been established to calculate the cavity eigen modes. Beam propagation method [64-66] that solves the beam propagation in the laser cavity has been under development since the 1970's by Seigman [64]. For example, the commercial solid-state laser CAD software LASCAD is based on this method [67]. This approach gives the full 3D information of the laser cavity and can incorporate thermal equations calculated by finite element method. Spatially dependent rate equations [68] have also been adopted to model CW and Q-switched operation of various solid-state lasers and intra-cavity frequency doubled solid-state lasers.

2.3 Maxwell Equations and Derivation of Governing Equations [54, 69]

The behavior of the optical wave is generally described by the Maxwell's equations

$$\nabla \times \vec{E}(\vec{r},t) = -\frac{\partial \vec{B}(\vec{r},t)}{\partial t}, \tag{2.1a}$$

$$\nabla \times \vec{H}(\vec{r},t) = \vec{J}(\vec{r},t) + \frac{\partial \vec{D}(\vec{r},t)}{\partial t}, \tag{2.1b}$$

$$\nabla \cdot \vec{D}(\vec{r},t) = \rho(\vec{r},t), \tag{2.1c}$$

$$\nabla \cdot \vec{B}(\vec{r},t) = 0, \tag{2.1d}$$

where $\vec{E}$ is the electric field (V/m), $\vec{B}$ is the magnetic flux density (Wb/ m^2), $\vec{H}$ is the magnetic field (A/m), $\vec{J}$ is the free current density (A/m^2), $\vec{D}$ is the electric displacement, and ρ is the free charge density (C/m^3).

For a dielectric material (or called passive medium) that contains no free charges,

$$\rho = 0, \tag{2.1e}$$

and that contains no free currents,

$$\vec{J} = 0. \tag{2.1f}$$

By assuming that the material is nonmagnetic ($\mu_r = 1$), the constitutive relations are

$$\vec{B}(\vec{r},t) = \mu_0 \vec{H}(\vec{r},t), \tag{2.1g}$$

$$\vec{D}(\vec{r},t) = \varepsilon_0 \vec{E}(\vec{r},t) + \vec{P}(\vec{r},t). \tag{2.1h}$$

The material polarization resulted from the movement of the electron cloud in response to the electrical field is given by

$$\vec{P} = \varepsilon_0 \chi \vec{E} = \varepsilon_0 \left(\chi^{(1)} \vec{E} + \chi^{(2)} : \vec{E}\vec{E} + \chi^{(2)} : \vec{E}\vec{E}\vec{E} + \cdots \right). \tag{2.2}$$

The first term stands for the linear response to the electric field in frequency space, and the second, third and higher order terms correspond to the nonlinear responses.

By taking the curl of Eq. (2.1a), and using Eqs. (2.1b), (2.1f) and (2.1g), we can obtain

$$\nabla \times \nabla \times \vec{E} + \mu_0 \frac{\partial^2 \vec{D}}{\partial^2 t} = 0. \tag{2.3}$$

Using Eq. (2.1h) to eliminate $\vec{D}$, we can find the wave equation

$$\nabla \times \nabla \times \vec{E} + \frac{1}{c^2}\frac{\partial^2 \vec{E}}{\partial t^2} = -\mu_0 \frac{\partial^2 \vec{P}}{\partial t^2}. \tag{2.4}$$

By using the identity from vector calculus, we get

$$\nabla \times \nabla \times \vec{E} = \nabla\left(\nabla \cdot \vec{E}\right) - \nabla^2 \vec{E}\ . \tag{2.5}$$

In the linear optics of isotropic source-free media, the first term on the right-hand side vanishes due to Eqs. (2.1c) and (2.1d). In the nonlinear optics this term is small enough to be negligible so that the wave equation can be taken to have the form

$$\nabla^2 \vec{E} - \frac{1}{c^2}\frac{\partial^2 \vec{E}}{\partial t^2} = \mu_0 \frac{\partial^2 \vec{P}}{\partial t^2}. \tag{2.6}$$

The polarization can be split into its linear and nonlinear parts as

$$\vec{P} = \vec{P}^{(1)} + \vec{P}^{NL}. \tag{2.7}$$

The displacement field $\vec{D}$ can also been decomposed into its linear and nonlinear parts as

$$\vec{D} = \vec{D}^{(1)} + \vec{P}^{NL}, \tag{2.8}$$

where the linear part is given by

$$\vec{D}^{(1)} = \varepsilon_0 \vec{E} + \vec{P}^{(1)} = \varepsilon_0\left(1 + \chi^{(1)}\right) \cdot \vec{E} = \varepsilon_0 \vec{\varepsilon}^{(1)} \cdot \vec{E}. \tag{2.9}$$

In the linear optics, the free wave propagating in a source free, non-resonant media gives

$$\nabla^2 \vec{E} - \mu_0 \frac{\partial^2 \vec{D}^{(1)}}{\partial t^2} = 0. \tag{2.10}$$

In the nonlinear optics, the wave equation becomes

$$\nabla^2 \vec{E} - \mu_0 \frac{\partial^2 \vec{D}^{(1)}}{\partial t^2} = \mu_0 \frac{\partial^2 \vec{P}^{NL}}{\partial t^2}. \tag{2.11}$$

2.3.1 Wave Equations in Gain Medium

In a resonant medium where the EM wave frequency is coincidence with the resonant frequency of the medium, for example, in semiconductor or solid-state gain media the linear susceptibility $\chi^{(1)}$ is a complex value, and can be written as

$$\chi^{(1)} = \chi' - i\chi''. \tag{2.12}$$

Then the wave equation Eq. (2.10) for an isotropic gain medium or a specific polarization direction becomes

$$\nabla^2 \vec{E} = \frac{1}{c^2}\left(1 + \chi' - i\chi''\right)\frac{\partial^2 \vec{E}}{\partial t^2}. \tag{2.13}$$

2.3.2 Nonlinear Polarizations in Nonlinear Medium

In terms of second-order nonlinearity, the two waves interact through the second-order polarization $\vec{P}^{(2)}$ .We take a general case of sum-frequency generation (SFG), where the interacting waves ω_1 and ω_2 generate a new wave ω_3 ($\omega_3 = \omega_1 + \omega_2$). The associated polarizations of each wave in frequency domain are written as

$$\vec{P}^{(2)}(\omega_1) = \varepsilon_0 \chi^{(2)}(-\omega_1; \omega_2 - \omega_3) E(\omega_2) E(-\omega_3), \tag{2.14a}$$

$$\vec{P}^{(2)}(\omega_2) = \varepsilon_0 \chi^{(2)}(-\omega_2; \omega_1 - \omega_3) E(\omega_1) E(-\omega_3), \tag{2.14b}$$

$$\vec{P}^{(2)}(\omega_3) = \varepsilon_0 \chi^{(2)}(-\omega_3; -\omega_1 - \omega_2) E(\omega_1) E(\omega_2). \tag{2.14c}$$

2.3.3 Time-domain Traveling Waves in Gain and Nonlinear Media

We assume that we can represent the electric field vector of the optical wave as n harmonic waves with discrete frequencies (ω_n) and relatively slow-varying envelopes

$$\vec{E}(\vec{r},t) = \frac{1}{2}\sum_n \vec{E}_n(\vec{r},t) e^{-i\omega_n t} + c.c.. \tag{2.15}$$

We can also assume the optical wave is composed of plane waves with wave vector k_n and spatially slow varying field amplitude $A_n(r, t)$ in the positive propagation direction (+z) by

$$\vec{E}_n = \vec{A}_n e^{ik_n z}. \tag{2.16}$$

So the total electrical field can be represented by

$$\vec{E}^{+}(\vec{r},t) = \frac{1}{2}\sum_n \vec{A}_n^{+}(\vec{r},t)e^{i(k_n z - i\omega_n t)} + c.c.. \tag{2.17}$$

And similarly, the nonlinear polarization $\vec{P}^{NL}$ can be represented by

$$\vec{P}^{NL+}(\vec{r},t) = \frac{1}{2}\sum_n \vec{P}_n^{+}(\vec{r},t)e^{i(k_n z - i\omega_n t)} + c.c.. \tag{2.18}$$

In the reverse propagation direction (-z), the electrical field and nonlinear polarization can be expressed as

$$\vec{E}^{-}(\vec{r},t) = \frac{1}{2}\sum_n \vec{A}_n^{-}(\vec{r},t)e^{i(-k_n z - i\omega_n t)} + c.c., \tag{2.19}$$

$$\vec{P}^{NL-}(\vec{r},t) = \frac{1}{2}\sum_n \vec{P}_n^{-}(\vec{r},t)e^{i(-k_n z - i\omega_n t)} + c.c.. \tag{2.20}$$

Taking the second derivative of Eq. (2.17) respect to z and t respectively, and by assuming the slow varying amplitude approximation in time and space domain, i.e.,

$\left|\frac{\partial^2 \vec{A}}{\partial t^2}\right| << \left|\omega\frac{\partial \vec{A}}{\partial t}\right|$, and $\left|\frac{\partial^2 \vec{A}}{\partial z^2}\right| << \left|k\frac{\partial \vec{A}}{\partial z}\right|$, the wave equation (2.13) can be written as [65]

$$\frac{1}{v_g}\frac{\partial \vec{A}_1^{+}(\vec{r},t)}{\partial t} + \frac{\partial \vec{A}_1^{+}(r,z)}{\partial z} = \frac{1}{2jk_1}\nabla_T^2 \vec{A}_1^{+}(r,z) + \left[\frac{1}{2}g(r,z) - \frac{1}{2}\alpha_1 - jk_0\Delta n(r,z)\right]\vec{A}_1^{+}(r,z) \tag{2.21}$$

in the gain medium, where $\vec{A}_1^+(\vec{r},t)$ is the fundamental wave, v_g is the group velocity, k_1 is the wave vector in the gain medium, gain (loss) and refractive index change terms are related to the imaginary and real parts of $1+\chi^{(1)}$.

With the approximation of $\partial^2\vec{P}^{NL}/\partial^2 t \approx -\omega^2\vec{P}^{NL}$ [70], the nonlinear wave equation (2.11) becomes

$$\frac{1}{v_g}\frac{\partial\vec{A}_i(\vec{r},t)}{\partial t}+\frac{\partial\vec{A}_i(r,z)}{\partial z}=\frac{1}{2jk_i}\nabla_T^2\vec{A}_i(r,z)+\frac{j\mu_0\omega_i^2}{2k_i}P_i^{NL}(\vec{r},t)e^{i(k_i z-\omega_i t)}, \tag{2.22}$$

where i=1,2,3 stands for the waves with frequency of ω_1, ω_2 and ω_3. In terms of second-harmonic generation in the +z direction ($\omega_1=\omega_2$, $\omega_3\rightarrow\omega_2$), insert Eq. (2.14) into Eq. (2.22) and we have

$$\frac{1}{v_g}\frac{\partial\vec{A}_1^+(\vec{r},t)}{\partial t}+\frac{\partial\vec{A}_1^+(r,z)}{\partial z}=\frac{1}{2jk_1}\nabla_T^2\vec{A}_1^+(r,z)+jk_1\chi^{(2)}\vec{A}_1^{+*}(r,z)\vec{A}_2^+(r,z)e^{-j\Delta_{SH}z}, \tag{2.23}$$

$$\frac{1}{v_g}\frac{\partial\vec{A}_2^+(\vec{r},t)}{\partial t}+\frac{\partial\vec{A}_2^+(r,z)}{\partial z}=\frac{1}{2jk_2}\nabla_T^2\vec{A}_2^+(r,z)+jk_1\chi^{(2)}\left[\vec{A}_1^+(r,z)\right]^2e^{+j\Delta_{SH}z}, \tag{2.24}$$

where $\vec{A}_1^+(\vec{r},t)$ is the fundamental wave and $\vec{A}_2^+(\vec{r},t)$ is the second-harmonic wave. The phase mismatch factor is

$$\Delta_{SH}=2k_1-k_2. \tag{2.25}$$

Similarly, in the backward direction, in the laser medium, the traveling wave equation is

$$\begin{aligned}\frac{1}{v_g}\frac{\partial\vec{A}_1^-(\vec{r},t)}{\partial t}-\frac{\partial\vec{A}_1^-(r,z)}{\partial z}&=\frac{1}{2jk_1}\nabla_T^2\vec{A}_1^-(r,z)\\&+\left[\frac{1}{2}g(r,z)-\frac{1}{2}\alpha_1-jk_1\Delta n(r,z)\right]\vec{A}_1^-(r,z)\end{aligned}. \tag{2.26}$$

And in the nonlinear medium,

$$\frac{1}{v_g}\frac{\partial\vec{A}_1^-(\vec{r},t)}{\partial t}-\frac{\partial\vec{A}_1^-(r,z)}{\partial z}=\frac{1}{jk_1}\nabla_T^2\vec{A}_1^-(r,z)+jk_1\chi^{(2)}\vec{A}_1^{-*}(r,z)\vec{A}_2^-(r,z)e^{+j\Delta_{SH}z}, \tag{2.27}$$

$$\frac{1}{v_g}\frac{\partial \vec{A}_2^-(\vec{r},t)}{\partial t} - \frac{\partial \vec{A}_2^-(r,z)}{\partial z} = \frac{1}{jk_2}\nabla_T^2 \vec{A}_2^-(r,z) + jk_1\chi^{(2)}\left[\vec{A}_1^-(r,z)\right]^2 e^{-j\Delta_{SH}z}. \qquad (2.28)$$

Eqs. (2.21) and (2.26) are general time-domain traveling wave (TDTW) equations governing wave propagations in the gain medium. Similarly, Eqs. (2.23), (2.24), (2.27) and (2.28) are TDTW equations governing wave propagations in the nonlinear medium with second-order polarizations. In the next three chapters we will use these equations and make further simplifications to deal with specific problems.

2.4 Quasi-phase Matching Technique

2.4.1 Basic Principle

In the second-order nonlinear optical interaction such as second-harmonic generation, the fundamental and SH wave vectors should be matched ($\Delta k = 0$), as indicted in Eq. (2.25). Besides the well known birefringence phase-matching and non-critical phase-matching, an alternative technique for achieving phase-matching in ferroelectric crystals is called quasi-phase matching (QPM) [69]. The crystal is arranged by some methods such that the direction of one principle axis is reversed periodically. By properly choosing the crystal orientation and polarization directions of the participating optical fields, a periodically modulation of the nonlinear coefficient tensor element can be obtained.

In QPM, only one polarization of the interacting waves is involved. For example, for the second-harmonic generation in lithium niobate, the polarization of the pump wave (ω_1) is polarized along the optical axis of the crystal (z). If the generated second-harmonic wave (ω_2) is also along z axis, through the nonlinear polarization (2.14c), the maximum second-order susceptibility element d_{zzz} (or d_{33}) could be accessed.

Phase matching requires that the wave vectors of the interacting waves should be matched. In terms of the second-harmonic generation, the phase matching is:

$$k_1 + k_1 = k_2, \text{ or } \frac{2\pi n_1}{\lambda_1} + \frac{2\pi n_1}{\lambda_1} = \frac{2\pi n_2}{\lambda_2}. \qquad (2.29)$$

If the refractive index of the nonlinear optical crystal is non-dispersive, i.e., n does not change with respect to wavelength, Eq.(2.29) is satisfied automatically for the interacting waves with one polarization. Unfortunately the refractive indices of materials are usually dispersive such that (2.29) cannot be satisfied at all. Typical dispersion curves for 5% MgO doped LN are shown in Fig. 2.1 as an example. In the angled phase matching technique, the refractive indices of both ordinary and extraordinary waves are involved and the associated phase velocities are matched at certain wavelengths. QPM only involves one polarization and the phase matching condition cannot be satisfied. Therefore a phase vector (k_G) is introduced to compensate the phase mismatch at the two wavelengths:

$$k_1 + k_1 + k_G = k_2 \text{ or } \frac{2\pi n_1}{\lambda_1} + \frac{2\pi n_1}{\lambda_1} + \frac{2\pi}{\Lambda} = \frac{2\pi n_2}{\lambda_2}, \tag{2.30}$$

where Λ is the period of the QPM grating.

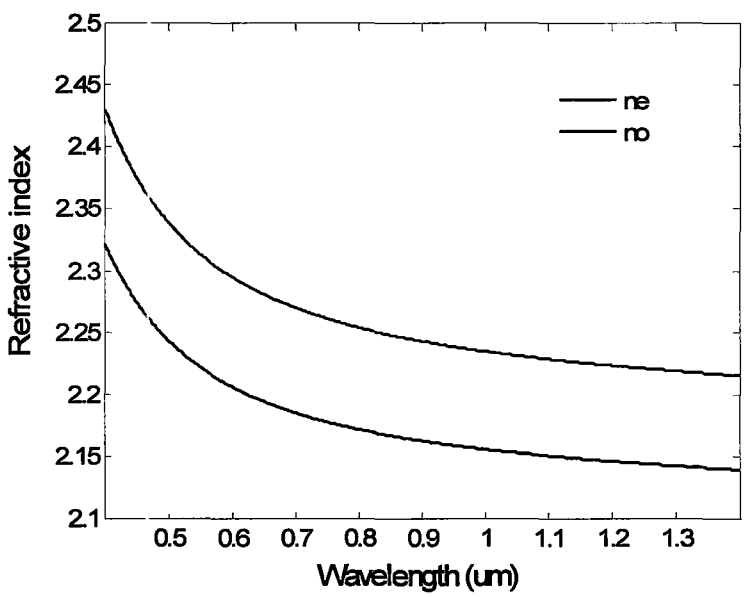

Fig. 2.1 Dispersion curves of 5%-MgO:LN [71].

Fig. 2.2 shows schematically the SHG field amplitude with nonlinear optical crystal length, for different phase matching conditions [69]. Under the phase matching condition, the interacting fundamental and SH waves always have a fixed phase relationship during the propagation in the nonlinear crystal; therefore

the SH power always increases with propagation distance; However, under a phase mismatching condition, after a coherent length defined as

$$L_{coh} = \frac{\pi}{2k_1 - k_2}, \tag{2.31}$$

the generated SH power will be converted back to the fundamental power. The QPM condition is that, at each time the field amplitude of the generated SH wave is about to decrease as a consequence of the wave vector mismatch, a reversal of the sign of d_{33} occurs which allows the field amplitude to continue to grow monotonically.

QPM has several advantages over traditional phase-matching techniques. First it can make use of the largest nonlinear coefficient ($d_{33} \approx 27$ pm/V for LN) of nonlinear crystals. Second it can cover the whole transparent range of the nonlinear crystal by choosing and fabricating proper grating periods. Finally QPM does not have "walk-off" effect as in the birefringence phase-matching crystals, since the polarizations of the fundamental and SH waves are both along the optical axis of the nonlinear crystal (e+e→e).

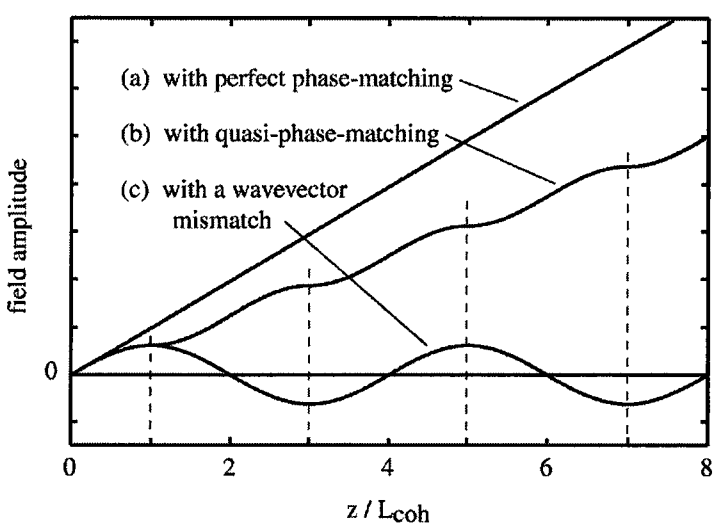

Fig. 2.2. QPM vs. phase-matching and phase-mismatching conditions [69].

2.4.2 Fabrication

Several methods have been demonstrated for the fabrication of QPM grating, which is called periodic poling in both bulk and waveguide ferroelectric materials

such as $LiNbO_3$ and $LiTaO_3$. Early methods include e-beam writing [72], corona discharging [73], etc. The most successful approach to date is the high voltage electric field application method [74-76] as shown schematically in Fig. 2.3.

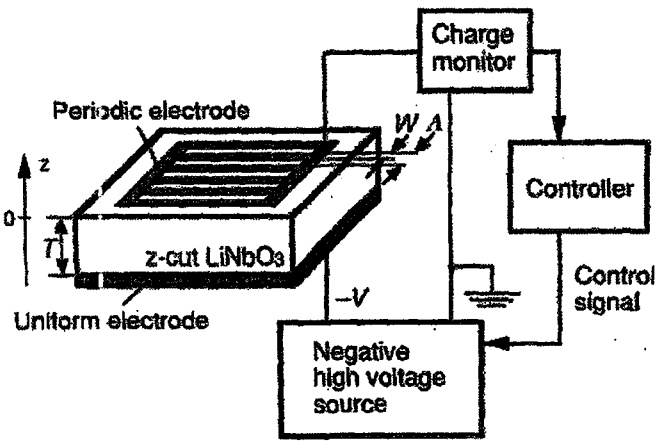

Fig. 2.3. Schematic setup of periodic poling [75].

The whole process occurs in two steps: poling electrode fabrication and high voltage application. The electrode fabrication includes (i) deposition of metal on the +z surface (and/or –z surface) by e-beam evaporation or sputtering; (ii) lithography with a metal photo-mask; (iii) develop of photo-resist and etching. The first step produces a metal electrode with the metal grid width W and grid period Λ. The second step, high voltage application, includes the application of high voltage pulses between the electrodes on the +z and –z surfaces under the total charge monitoring [75].

2.5 Second-harmonic Generation in a Laser Cavity

As introduced in Chapter 1, IC-SHG or IC-FD performs much better compared with the straightforward single-pass FD process. By placing a nonlinear crystal within the laser resonator the FD process can be greatly enhanced because the fundamental wave intensity inside the laser resonator is enhanced as the output mirror's reflectivity R is close to 1. Experiment of solid-state intra-cavity frequency doubled laser at 532 nm was first demonstrated in 1968 by R. G. Smith with a lamp pumped Nd:YAG laser, frequency doubled by a $BaNaNO_3$ crystal [18], and analyzed theoretically in 1970 [19]. It was concluded experimentally

and later theoretically that under proper/optimum conditions, all of the available fundamental power that can be extracted from the laser resonator was converted to the SH power. In this sense the total conversion efficiency is 100%.

2.6 Summary

This chapter deals with the basic theoretical background for the following chapters in this thesis. We first reviewed the numerical techniques for modeling semiconductor lasers and solid-state lasers. Then we derived the general time-domain traveling wave equations from the Maxwell equations in both gain and optical nonlinear media, which are the governing equations in the following chapters. Then we introduced the concept of quasi-phase matching (QPM) in nonlinear medium and related fabrication methods, and introduced the concept of IC-FD.

CHAPTER 3

DBR-LD/MgO:PPLN GREEN LASER MODELING AND DESIGN

3.1 Introduction

Efficient and high power continuous wave (CW) green lasers are of great interest for many applications, including bio-photonics, undersea communications and laser displays as reviewed in Chapter 1. This chapter is mainly focused on a new green laser device modeling and design, demonstrating its high efficiency, high output power and high modulation capability.

The efficiency of green lasers is one of the most critical parameters in many mobile projection systems where battery power is a concern for long-time operation. Direct InGaN green laser diodes are still under intensive research and development and far from mature. The total electrical-to-optical (EO) efficiency is only <1% at 531 nm, and 3-5% at around 521 nm [13-15]. One popular method to efficiently generate green light currently is based on intra-cavity frequency doubling (IC-FD) (or intra-cavity second-harmonic generation (IC-SHG)) of DPSS lasers. Currently the EO efficiency at several Watts of green light is about >20% [22-24]; At low green light power level, optical contact Nd:YVO_4/MgO:PPLN green lasers can reach 10-15% [77,78].

On the other hand, a more straightforward method to generate green light is to employ single-pass FD of semiconductor lasers. It is obvious that direct FD of semiconductor lasers with bulk or waveguide nonlinear crystals has the least number of conversion steps (except direct InGaN LDs), e.g., electrical to 1064 nm to 532 nm for single-pass FD, instead of electrical to 808 nm to 1064 nm to 532 nm for the IC-FD of DPSS laser configuration. Therefore, potentially higher EO conversion efficiencies (>30%) for waveguide devices are possible, even at a relatively low pump power range (<1 W). It has been reported by Corning Inc. that they achieved a wall-plug efficiency of 10% including the power consuming of temperature controlling of the whole device. We can estimate from their published papers [30-34] that the EO efficiency is larger than 15% when the green light power is 304-mW (forward voltage was 2.2V@800mW) [33] if other power

consuming mechanism is ignored here. Such device performance sets a benchmark for other high efficiency and low power green lasers. Other advantages of single-pass FD of semiconductor lasers over IC-FD of DPSS lasers include low noise, high frequency modulation capability, compactness and potentially low cost, which is especially suitable for micro-mirror-based laser projection systems [79]. However, the necessity for a long nonlinear optical crystal, narrow temperature tolerance, and the waste of a portion of fundamental power, still cannot be avoided in the single-pass FD method.

These problems in single-pass frequency doubled green lasers are solved by the design of IC-FD of semiconductor lasers theoretically and experimentally [19, 44, 80]. Based on the reported structure of single-pass FD of a high power distributed Bragg reflector laser diode (DBR-LD) by a MgO:PPLN ridge waveguide, which we call here a singe-pass frequency doubled DBR-LD/MgO:PPLN green laser, we propose a new device called intra-cavity frequency doubled DBR-LD/MgO:PPLN green laser. General time-domain traveling wave (TDTW) rate equations [57-59] are implemented to model the characteristics of these two types of green lasers. Comparisons are made between the numerical simulations and published experimental results from the reported single-pass frequency doubled DBR-LD/MgO:PPLN green lasers to verify the numerical model. After the confirmation of our numerical model, it is then extended to the proposed IC-FD device, in which the dependence of the SHG power upon the pump current, nonlinear crystal length and coupling efficiency are simulated and compared with the single-pass FD device, showing the advantages

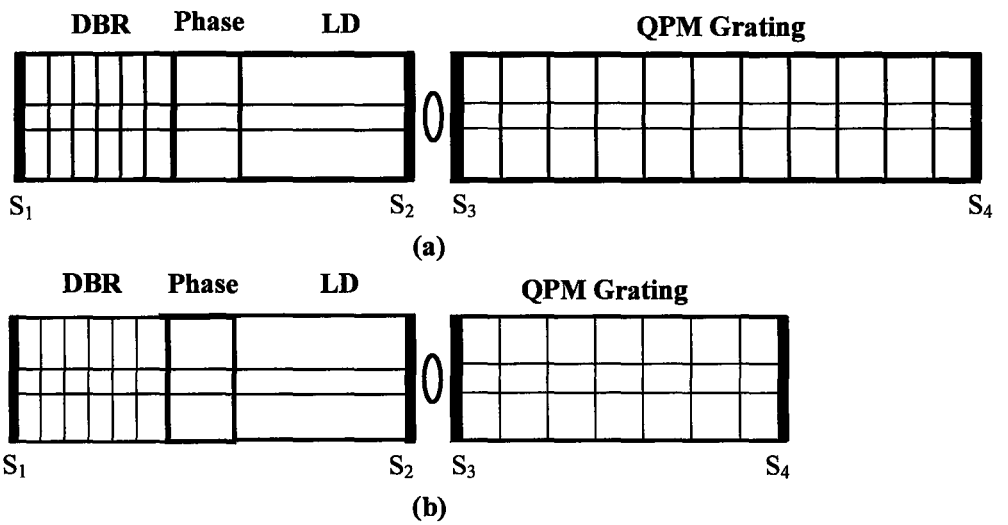

Fig. 3.1. Schematic device structure of (a) single-pass frequency doubled DBR-LD/MgO:PPLN green laser; and (b) intra-cavity frequency doubled DBR-LD/MgO:PPLN green laser.

of the proposed device. Furthermore, by the numerical method we also investigate the IC-FD of a semiconductor laser with a bulk MgO:PPLN. Simulations show that with the enhancement of the SH wave as well, the conversion efficiency is high enough for practical applications as well.

3.2 Device Structures and Numerical Method

3.2.1 Schematic Device Structures

The schematic device structures employed in our simulations are shown in Fig. 3.1. The first device structure, shown in Fig. 3.1(a), is a waveguide type single-pass FD configuration, which is the same as the reported structures [30-34]. The high power laser diode is a strained InGaAs/AlGaAs single quantum-well DBR laser emitting at 1060 nm and the FD device is a MgO: PPLN ridge waveguide. High coupling efficiency between the DBR laser and the MgO: PPLN is realized by collimation and focusing lenses. The second structure, shown in Fig. 3.1 (b), is a modification of Fig. 3.1 (a). In this structure, the DBR section has an even higher reflection at the fundamental wavelength. The left facet (S_3) of the MgO: PPLN waveguide is anti-reflection (AR) coated at the fundamental wavelength and high-reflection (HR) coated at the SH wavelength. The right facet (S_4) is HR coated at the fundamental wavelength and AR coated at the SH wavelength, thus forming an IC-FD configuration.

3.2.2 Traveling Wave Equations for the Semiconductor Laser Section [57-59]

We define forward (+) and backward (-) traveling waves propagating along z in a single mode waveguide with an effective mode area of A_{eff} as follows:

$$E_1(z,t) = E_1^+(z,t) + E_1^-(z,t) = \sqrt{2h\nu_1/\varepsilon_0\varepsilon_1}[F_1(z,t)e^{+i\beta_1 z} + R_1(z,t)e^{-i\beta_1 z}]e^{-i\omega_1 t} \quad , \quad (3.1a)$$

$$E_2(z,t) = E_2^+(z,t) + E_2^-(z,t) = \sqrt{2h\nu_2/\varepsilon_0\varepsilon_2}[F_2(z,t)e^{+i\beta_2 z} + R_2(z,t)e^{-i\beta_2 z}]e^{-i\omega_2 t} \quad , \quad (3.1b)$$

where h is the Plank constant, ε_0 is the permittivity in vacuum, ε_1 and ε_2 are the relative dielectric constants, ν_1 and ν_2 are the optical frequencies, β_1 and β_2 are the propagation constants, E_1 and E_2 (in V/cm) are the electrical fields, and F_1 and F_2 (in $cm^{-3/2}$) are the forward envelop fields while R_1 and R_2 (in $cm^{-3/2}$) are the backward envelope fields of the fundamental and second-harmonic (SH) waves, respectively.

The envelope fields are normalized to the photon density S (in cm^{-3}) through

$$S_i(z,t) = |F_i(z,t)|^2 + |R_i(z,t)|^2, \tag{3.2}$$

where i = 1 and 2 for the fundamental and the SH waves respectively.

Based on Eq. (2.21) and (2.26), the fundamental envelope equations in the DBR laser section are rewritten as

$$\frac{1}{v_g}\frac{\partial F_1(t,z)}{\partial t} + \frac{\partial F_1(t,z)}{\partial z} = \left[\frac{1}{2}(\Gamma g - \alpha) + i\delta\right]F_1(t,z) + i\kappa R_1(t,z) + s_f, \tag{3.3a}$$

$$\frac{1}{v_g}\frac{\partial R_1(t,z)}{\partial t} - \frac{\partial R_1(t,z)}{\partial z} = \left[\frac{1}{2}(\Gamma g - \alpha) + i\delta\right]R_1(t,z) + i\kappa F_1(z,t) + s_r, \tag{3.3b}$$

where v_g is the group velocity in the medium, g is the gain of the active section, α is the total cavity internal loss including the cladding layer free carrier absorption loss and the waveguide scattering loss, κ is the coupling coefficient in the DBR section, and s_r and s_f are the spontaneous noises coupled to forward and backward fields, which can be simulated by a Gaussian distributed random number generator that satisfies the correlation

$$\langle s(z,t)s^*(z't')\rangle = \beta K R_{sp}\delta(t-t')\delta(z-z')/v_g, \tag{3.4}$$

where $R_{sp}=BN^2/L$ is the bimolecular recombination per unit length contributed to spontaneous emission, and K is the transverse Petermann factor.

The confinement factor Γ is defined as the ratio of the active region area to the optical mode field area through

$$\Gamma = \frac{W \cdot d}{A_{eff}}, \tag{3.5}$$

where W is the width of the waveguide, and d is the thickness of the quantum well layers.

The Bragg grating detuning factor δ is

$$\delta(N,\lambda_1)=\frac{\omega_1}{c}n_{eff}(N)-\frac{\pi}{\Lambda}, \tag{3.6}$$

where Λ is the period of the Bragg grating, which satisfies the Bragg reflection condition

$$\beta_1-(-\beta_1)=\frac{2\pi m}{\Lambda}, \tag{3.7}$$

where m is the order of Bragg reflection, κ is the coupling coefficient for the mth-order of the Bragg grating.

Optical gain for quantum well materials can be modeled as

$$g(N)=g_0\ln(N/N_{tr}), \tag{3.8}$$

where g_0 is the differential gain coefficient, and N_{tr} is the transparency carrier density.

Refractive index change in the semiconductor gain medium is related to the line-width enhancement factor through

$$n_{eff}(N)=n_{eff0}-\frac{\lambda_1}{4\pi}\Gamma\alpha_{LEF}g(N), \tag{3.9}$$

where n_{eff0} is the effective index of the cold laser cavity, and α_{LEF} is the line-width enhancement factor.

The carrier density equation in the DBR laser section is

$$\frac{dN(z,t)}{dt}=\frac{J(z,t)}{ed}-\frac{N(z,t)}{\tau}-v_g g(N)S_1(z,t), \tag{3.10}$$

where J is the injected current density, τ is the carrier lifetime, and e is the electron charge.

3.2.3 Traveling Wave Equations in QPM Waveguide [81]

According to Eqs. (2.23), (2. 24), (2.27) and (2.28) in Chapter 2, in the periodic poled nonlinear crystal waveguide section, by using

$A_1^+ = \sqrt{2h\nu_1/\varepsilon_0\varepsilon_1}F_1\exp(-j\delta_{SH})$, $A_2^+ = \sqrt{2h\nu_2/\varepsilon_0\varepsilon_2}F_2\exp(-j\delta_{SH})$ in the forward direction, and

$A_1^- = \sqrt{2h\nu_1/\varepsilon_0\varepsilon_1}R_1\exp(+j\delta_{SH})$, $A_2^- = \sqrt{2h\nu_2/\varepsilon_0\varepsilon_2}R_2\exp(+j\delta_{SH})$ in the backward direction, the TDTW equations are derived in forms similar to those in the DBR laser section

$$\frac{1}{v_{g1}}\frac{\partial F_1(t,z)}{\partial t}+\frac{\partial F_1(t,z)}{\partial z}=\left[j\delta_{SH}-\frac{1}{2}(\alpha_1+\alpha_{NL})\right]F_1(t,z) - j\kappa_{SH2}F_1^*(t,z)F_2(t,z), \tag{3.11a}$$

$$\frac{1}{v_{g2}}\frac{\partial F_2(t,z)}{\partial t}+\frac{\partial F_2(t,z)}{\partial z}=\left(j\delta_{SH}-\frac{1}{2}\alpha_2\right)F_2(t,z) - j\kappa_{SH1}\left[F_1(t,z)\right]^2, \tag{3.11b}$$

$$\frac{1}{v_{g1}}\frac{\partial R_1(t,z)}{\partial t}-\frac{\partial R_1(t,z)}{\partial z}=\left[-j\delta_{SH}-\frac{1}{2}(\alpha_1+\alpha_{NL})\right]R_1(t,z) - j\kappa_{SH2}R_1^*(t,z)R_2(t,z), \tag{3.11c}$$

$$\frac{1}{v_{g2}}\frac{\partial R_2(t,z)}{\partial t}-\frac{\partial R_2(t,z)}{\partial z}=\left(-j\delta_{SH}-\frac{1}{2}\alpha_2\right)R_2(t,z) - j\kappa_{SH1}\left[R_1(t,z)\right]^2, \tag{3.11d}$$

where α_1 (α_2) is the linear absorption coefficient for the fundamental (SH) wave, α_{NL} is the green induced infrared absorption (GRIIRA) coefficient. κ_{SHi} is the nonlinear coupling coefficient, which is normalized to the envelope fields and is given by

$$\kappa_{SHi}=\sqrt{\frac{2h\nu_1^2}{\varepsilon_0\varepsilon_i v_i}}\frac{\pi}{n_1\lambda_1}d_{eff}, \tag{3.12}$$

where d_{eff} is the effective second-order nonlinear coefficient, and $d_{eff}=2d_{33}/\pi$ for the first order QPM grating. δ_{SH} , the quasi-phase matched (QPM) mismatch factor in the nonlinear crystal, is given by

$$\delta_{SH} = 2k_1 - k_2 - \frac{2\pi}{\Lambda_Q}, \tag{3.13}$$

where Λ_Q is the period of the QPM grating and $k_i = 2\pi n_i / \lambda_i$, n_i is the refractive index of the nonlinear optical crystal at λ_i.

Optical power inside the cavity is related to the envelop fields through

$$P_i^{\pm} = h\nu_i \cdot A_{effi} \cdot v_{gi} \cdot |F_i, R_i|^2. \tag{3.14}$$

3.3 Numerical Implementation

Fig. 3.2 shows the mesh discretization for the forward and backward fundamental and SH wave field propagation in (a) the gain (and phase) section, (b) the Bragg grating section, (c) the gap region between the semiconductor laser diode (LD) and the waveguide, and (d) the SHG section. By using the finite difference scheme [57], at each time step defined by $\Delta t = \Delta z / v_g$, in the DBR laser

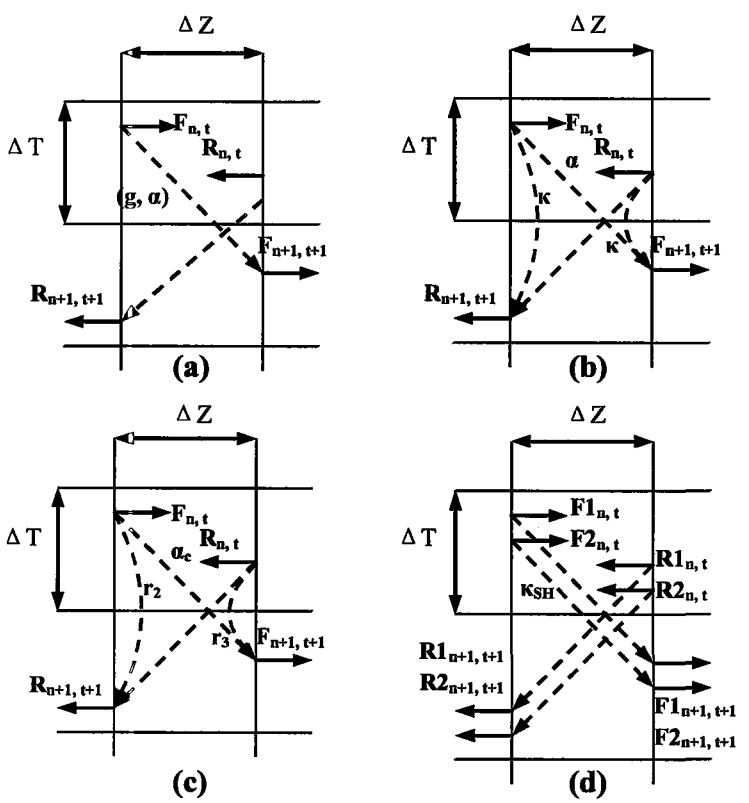

Fig. 3.2. Mesh discretization for (a) active and phase section; (b) Bragg grating section; (c) gap between LD and MgO: PPLN waveguide; and (d) MgO: PPLN section.

section, the fundamental envelope fields (F_n, R_n) are calculated with initial noise terms in each section. Carrier density in each section is simultaneously calculated with (3.10). When the envelope fields propagate in the MgO: PPLN section, both fundamental ($F1_n$, $R1_n$) and SH waves ($F2_n$, $R2_n$) are calculated through (3.11). Modulation can be readily modeled by directly applying current modulation in the semiconductor gain section.

3.4 Single-pass Frequency Doubled DBR-LD/MgO:PPLN Green Laser Modeling and Validation

3.4.1 Device Parameters Extraction

As a validation of our numerical model and a reference to the calculation of the proposed intra-cavity frequency doubled DBR-LD/MgO:PPLN green laser, performances of the single-pass frequency doubled DBR-LD/MgO:PPLN green laser was simulated and compared with the reported results first. Detailed device structure and parameters are mainly adopted from [30-34] and are listed in Table 3.1. They are briefly summarized below:

Table 3.1. Material and device parameters used in the simulation [30-34]

Parameters	Values
Nonlinear coefficient (d_{33})	25 pm/V
MgO: PPLN fundamental absorption coefficient (a_1)	0.002 cm^{-1}
SH absorption coefficient in MgO: PPLN (a_2)	0.01 cm^{-1}
Green induced infrared absorption coefficient (α_{NL})	0.006 cm^{-1}
Gain coefficient (g_0)	1000cm^{-1}
Quantum well thickness (d)	8 nm
Carrier lifetime (τ)	2.5 ns
LD internal loss (a)	2 cm^{-1}
Confinement factor (Γ)	1%
Transparency carrier density (N_{tr})	1.7×10^{18}c m^{-3}
Linewidth enhancement factor (α_{LEF})	2
DBR coupling coefficient (κ)	13 cm^{-1}
Effective phase refractive index (neff)	3.4

(a) MgO:PPLN Ridge Waveguide

The nonlinear material used in the simulation was an x-cut MgO: PPLN waveguide with polarization compatibility with the TE polarization of the 1060 nm InGaAs/GaAs laser diode. Since the ridge waveguide dimension is unavailable from the reported results, a single mode MgO: PPLN ridge waveguide with the dimensions of 3 μm by 5 μm is used in the simulations [82]. The ridge waveguide loss fabricated by the optical bonding and precise grinding method [82] has a loss of 0.3 dB/cm (0.07 cm^{-1}). This value will be incorporated into the intrinsic loss coefficients (α_1 and α_2) in Eq. (3.9) to account for the total waveguide losses. In order to keep the light power far below the photorefractive damage threshold of the 5 mol% MgO-doped LN [83], [84], the highest input pump power into the MgO: PPLN waveguide was about 500 mW, corresponding to an intensity of 3 MW/cm^2 at the fundamental wavelength in the waveguide. AR coatings at 1060 & 530 nm were deposited on both facets (S_3 and S_4) with reflectivity assumed to be 0.1%.

(b) High Power DBR-LD

The high power pump laser diode was an InGaAs/AlGaAs single quantum well ridge waveguide DBR laser [30-34]. A 2250 μm gain section, 450 μm phase tuning section, and 1400 μm DBR section were used in the simulation based on the estimation of the reported 0.054 nm longitudinal mode interval in the optical spectrum [33], resulting in an effective cavity length of about 3.1 mm. The DBR section was assumed to have a reflectivity of 90% with $\kappa = 13$ cm^{-1}. Usually, the front facet, S_2, of the LD is windowed by a non-pumped region, and/or passivated and AR coated to reduce the facet loading in case catastrophic optical mirror damage (COMD) occurs under high facet intensity. In our simulation, this window region is neglected and the facet intensity loading is monitored to be below the COMD power density $\overline{P}_{COMD}$ [85]:

$$P_{\max,CW} = \left(\frac{d}{\Gamma}\right) W \left(\frac{1-R}{1+R}\right) \overline{P}_{COMD} , \tag{3.15}$$

where W is the active region waveguide width. The effective mode profile in the active region is estimated to be approximately 4 μm by 1 μm [86] with the far field full-width half-maximum (FWHM) divergence angles of 7° laterally and 22° vertically, according to [33], [87]:

$$\theta_{1/2} = 2\tan\left(\frac{0.59\lambda}{\pi w}\right), \tag{3.16}$$

where $\theta_{1/2}$ is the FWHM divergence angle, and w is the beam waist in the waveguide. With a maximum output power of 800 mW, and no thermal roll over or COMD [32], the COMD power density for Corning's high power LD is estimated to be > 30 MW/cm^2, which is even larger than that of the reported 980 nm InGaAs broad area laser diodes [88].

(c) Coupling

Coupling between the LD waveguide and the MgO: PPLN waveguide was realized by two identical aspherical lenses [30-34]. A high coupling efficiency from the LD to the MgO: PPLN waveguide was achieved by matching the modal fields of the LD and MgO: PPLN waveguide through proper selection of lenses. We did not consider the details of coupling elements used in the experiments, and a simple coupling coefficient was used instead without losing generalities. The typical experimental value of 0.836 [33] (corresponding to a power coupling coefficient of 70%) is used in calculations. Therefore the coupling loss term α_c in the gap region is -0.356, resulting in a total power loss of *exp* (-0.356) = 30%.

3.4.2 Performance Modeling and Validation

For the single-pass frequency doubled DBR-LD/MgO:PPLN green lasers, the optimization of the device is done separately for the high power DBR-LD and MgO: PPLN waveguide. For the laser diode, a high output power with good single transverse mode profile and single longitudinal mode spectrum, lower threshold current, and higher slope efficiency are key design parameters. A reported Fabry-Perot (FP) LD with a cavity length of 3-mm long and facet reflectivity of 95% and 5% for the S_1 and S_2 facets, respectively, is simulated and compared with experimental results [32] (not shown here). The calculated threshold current of 40 mA and slope efficiency of 78% fits the experimental data very well.

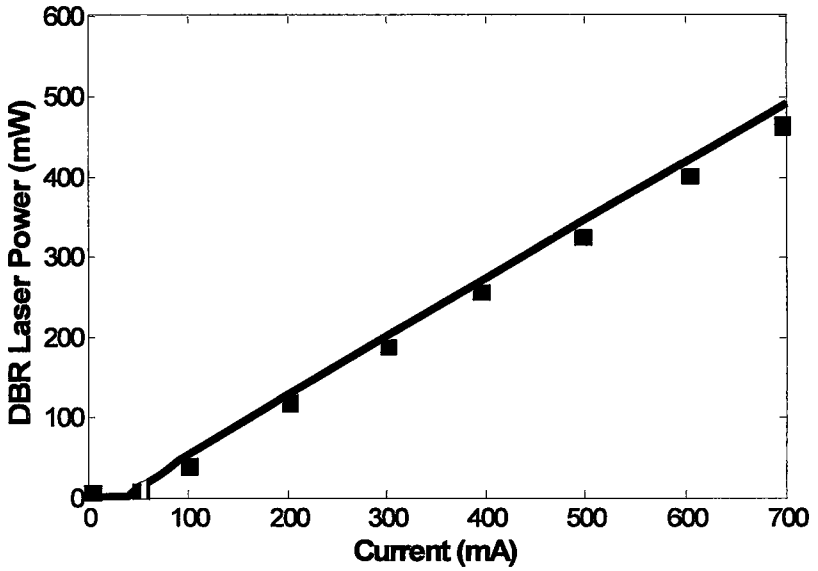

Fig. 3.3(a). P-I curve of the calculated (line) and experimental (square) results of the reported DBR laser diode. Inset is the calculated optical spectrum at 700 mA.

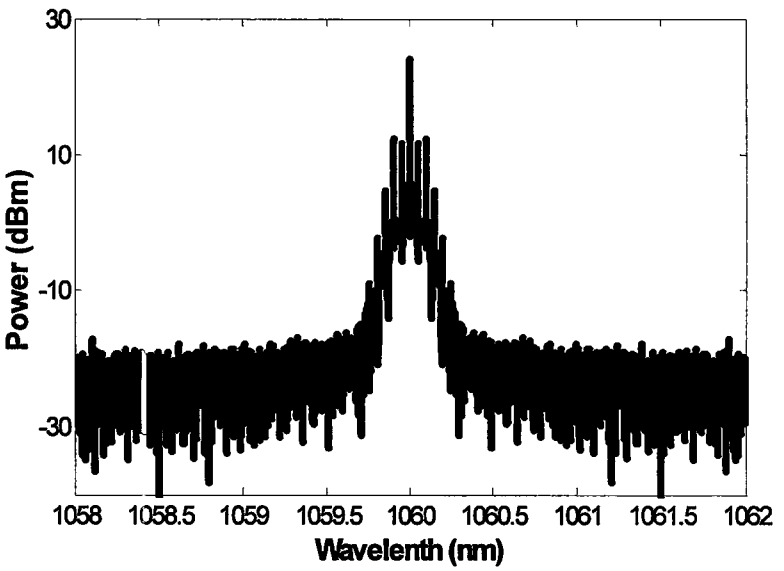

Fig. 3.3(b). Calculated optical spectrum at 700 mA for the DBR laser diode.

Second, we simulated the reported DBR laser [34], which has the same device structure and parameters. Fig. 3.3(a) shows the P-I curve of the simulated and experimental results [34] of the DBR laser. The corresponding optical

spectrum with a calculated resolution of 0.6257 pm (0.167 GHz) is shown in Fig. 3.3(b). The simulated results agree quite well with the experimental results. Finally, we calculated the reported single-pass frequency doubled DBR-LD/MgO:PPLN green laser [34] to further validate the numerical model. Fig. 3.4 shows simulated and experimental results [34] of the single-pass frequency doubled DBR-LD/MgO:PPLN laser power with pump power coupled into the 12 mm-long MgO: PPLN waveguide. The simulation results are in good agreement with the experimental data.

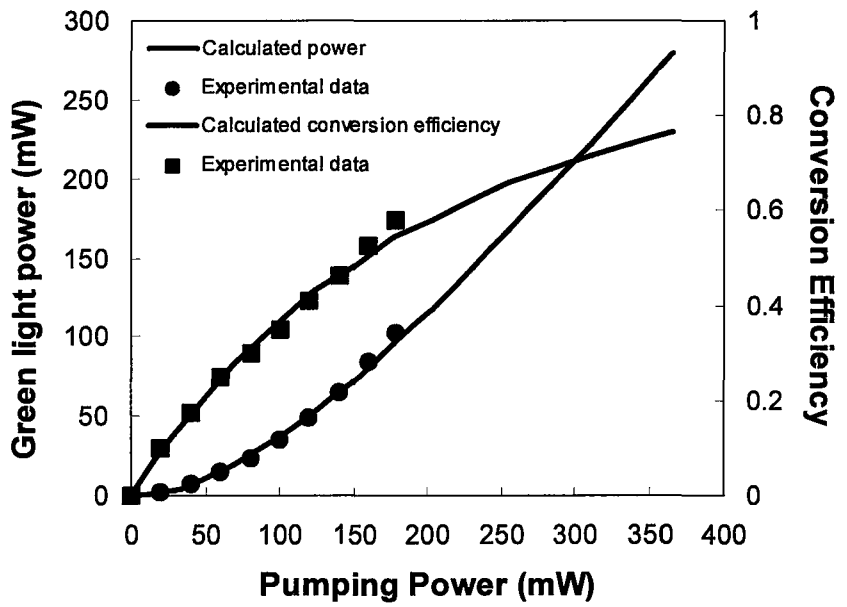

Fig. 3.4. Simulated and experimental results on green light power and conversion efficiency with pump power coupled into the waveguide, for the single-pass DBR-LD/MgO:PPLN green laser.

3.5 Intra-cavity Frequency Doubled DBR-LD/MgO:PPLN Green Laser Design

Disadvantages of the single-pass frequency doubled DBR-LD/MgO:PPLN green lasers are obvious: 1) a long nonlinear crystal is required for high conversion efficiency, thus narrowing temperature and wavelength tolerances and possibly inducing a thermal de-phasing effect; 2) a portion of the fundamental power is wasted as a result of incomplete frequency conversion. In this section,

we will investigate our proposed intra-cavity frequency doubled DBR-LD/MgO:PPLN green laser structure, where some of the problems are solved.

3.5.1 Modified Device Parameters

The modified structure shown in Fig. 3.1(b) forms an intra-cavity configuration. The IC-FD design may overcome the mentioned disadvantages above with minimum device modification from the single-pass FD device. However, since high power semiconductor LDs are high optical gain devices, the power density in the semiconductor laser cavity is very high and a low front facet reflectivity (5% or lower) is needed to extract the energy and to avoid high circulation power density in the cavity. Therefore, the intra-cavity intensity is slightly larger than the output power density for a high power LD. In the simulation, material parameters used to calculate the intra-cavity frequency doubled DBR-LD/MgO:PPLN green laser are essentially the same as those used in the single-pass frequency doubled DBR-LD/MgO:PPLN green laser, except that the Bragg grating has a higher coupling coefficient ($\kappa = 25\ cm^{-1}$), resulting in a higher left facet (S_1) reflectivity (99.9%). An AR coating (R=0.1%) at the fundamental wavelength is fabricated on the front facet of the LD (S_2) to reduce back reflection. The left facet of the MgO: PPLN waveguide (S_3) is AR coated (T=99.85%) at the fundamental wavelength and HR coated (R=95%) at the SH wavelength. The right facet of the MgO: PPLN waveguide (S_4) is HR coated (R=99.85%) at the fundamental wavelength and AR coated (T=99%) at the SH wavelength. Coupling from the LD to the waveguide is assumed to be the same as the single-pass configuration, for best comparison. Facet coating data of the MgO:PPLN waveguide are adopted according to commercial coating companies. Coatings at fundamental wavelength is more critical since the SH wave is not enhanced in the cavity, whereas the fundamental wave is enhanced by the cavity. On the other hand, the intra-cavity fundamental power is much more influenced by the fundamental power losses in the cavity and is linked with the conversion efficiency of IC-FD process directly.

3.5.2 Design and Comparison

In this section, general device design and comparisons of the two devices are presented. Fig. 3.5 shows typical intra-cavity power distributions for both fundamental and SH waves when the coupling efficiency is 70% and the LD is

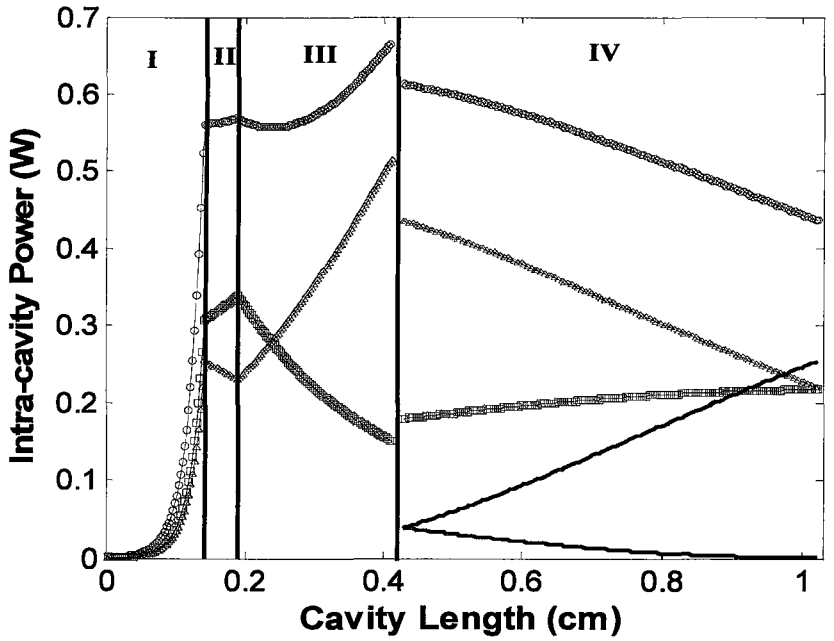

Fig. 3.5. Intra-cavity power distributions for both fundamental and SH waves. Red: total cavity power; Purple: forward fundamental power; Blue: backward fundamental power; Green: forward and backward SHG power. The MgO: PPLN is 6 mm, the coupling efficiency is 70%, and injection current is 700 mA. Sections of Bragg grating, phase, gain, and MgO: PPLN are divided by back vertical lines, denoted as region I, II, III and IV.

pumped at 700 mA. This shows clear fundamental power depletion distribution along the total cavity. At the gap region, the large power drop is due to the coupling loss. Obviously, this will decrease the fundamental wave intensity in the MgO: PPLN waveguide and thus, the SHG efficiency.

(a) Generation of Green Light Power

Fig. 3.6 shows the SHG power vs. injection current for two MgO: PPLN waveguide lengths of 6-mm and 12-mm. Compared with the 12-mm-long single-passed frequency doubled DBR-LD/MgO: PPLN device, at the same pump current (700 mA), the 6 mm MgO: PPLN waveguide will generate a slightly larger green light power in the IC-FD configuration. The 6 mm-long MgO: PPLN

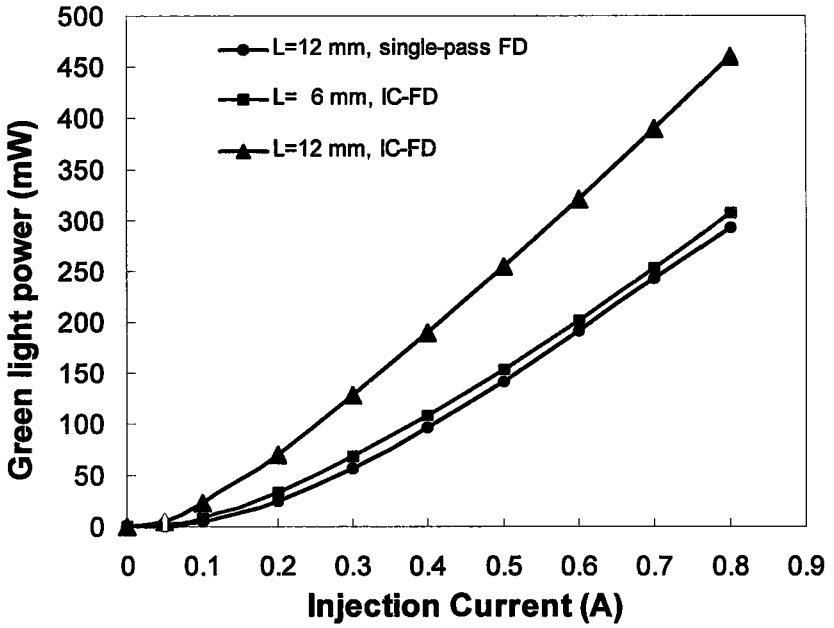

Fig. 3.6. IC-FD laser power with injection current for two MgO: PPLN lengths. A single-pass FD laser with the same parameters is also shown for comparison. The coupling efficiency is 70%.

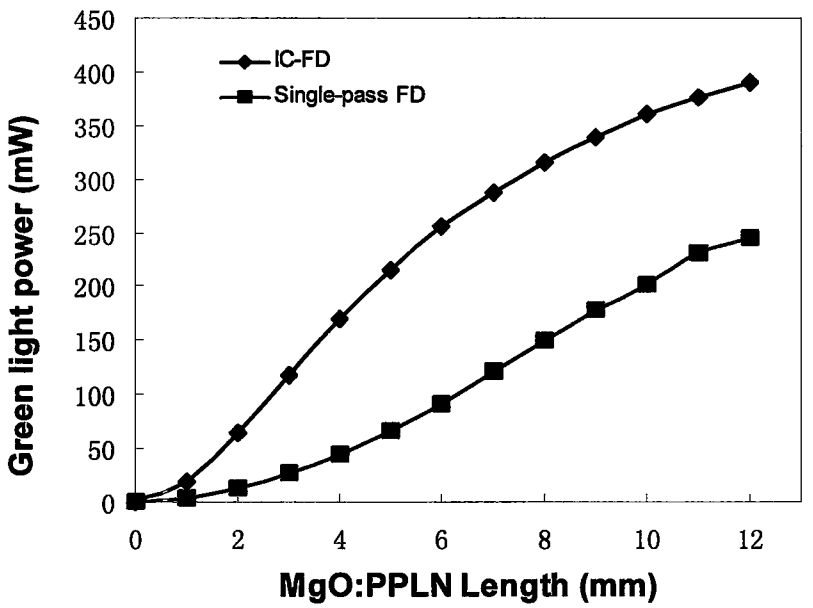

Fig. 3.7. Green light power with different MgO: PPLN lengths for IC-FD and single-pass FD devices, with pump current of 700 mA and coupling efficiency of 70%.

waveguide in the intra-cavity configuration functions equivalently to a double-pass SHG, such that in principle it may generate the same green light power as a

12 mm MgO: PPLN in the single-pass configuration. As comparisons, if the MgO: PPLN used in the IC-FD configuration has the same length (12 mm) as that in the single-pass FD configuration, much more power can be generated. Fig. 3.7 shows calculated green light power with different MgO: PPLN lengths for IC-FD and single-pass FD devices, with pump current of 700 mA and coupling efficiency of 70%. It is evident that the IC-FD device is much more efficient than singe-pass FD.

(b) Temperature Tuning

Temperature dependent extraordinary refractive index dispersion [71] of the MgO:LN material will contribute to the phase mismatch factor through (3.11). Therefore the phase-mismatch factor is a function of temperature. Calculated temperature tuning curves for the single-pass FD device with 12-mm waveguide

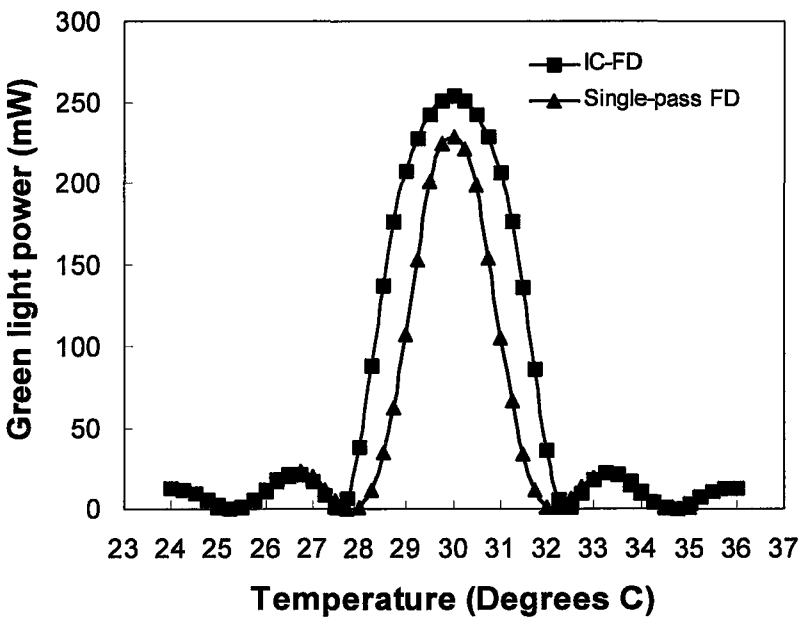

Fig. 3.8. Temperature tuning curves for the single-pass FD with a 12-mm MgO: PPLN waveguide and IC-FD with a 6-mm waveguide, when pumped at 700 mA. The coupling efficiency is 70%.

and IC-FD device with 6-mm waveguide are shown in Fig. 3.8. The 3-dB temperature bandwidth is 2 °C for the single-pass FD and about 3.6 °C for the IC-FD with the 6-mm MgO: PPLN waveguide. The enlarged temperature tolerance is another advantage of the IC-FD over the single-pass FD configuration, which means less crucial temperature control is needed for the IC-FD device.

(C) Influence of Coupling Efficiency

The coupling efficiency between the LD and the MgO: PPLN waveguide is an important factor to scale conversion efficiency, due to the fact that the internal power density depends on the total cavity losses. Fig. 3.9 shows the SHG power with different coupling coefficients (i.e. different cavity losses) at a fixed pump current of 700 mA, for the single-pass FD and IC-FD devices. For example, comparing the two curves using 6-mm long waveguide for the single-pass FD and 3-mm long waveguide for the IC-FD device, the IC-FD device can generate more

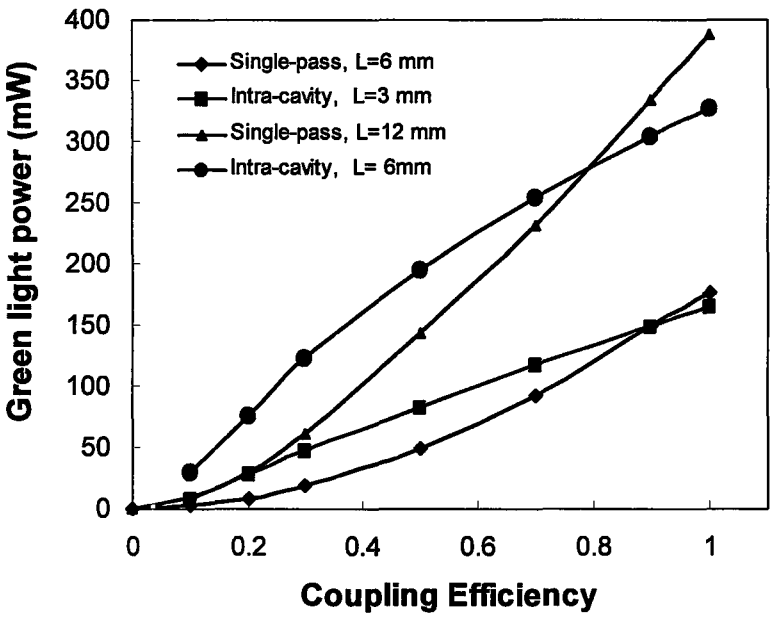

Fig. 3.9. SHG green light power for single-pass FD and IC-FD with different coupling efficiency between LD and MgO: PPLN waveguide, when pumped at 700 mA.

green light power than the single-pass FD device under coupling efficiency up to 90%. More importantly, under low coupling efficiency range, the generated green light power by IC-FD is even twice as high as that by single-pass FD. At higher coupling efficiency range, the advantage of IC-FD with half MgO: PPLN waveguide length is weakened and it may be surpassed by the single-pass FD. This is more obvious in the case of longer MgO: PPLN waveguide. As shown in Fig. 3.9, at the equal power point for the IC-FD device with 6-mm long waveguide and the single-pass FD device with 12-mm long waveguide, the coupling efficiency is nearly 80%. However, such a coupling efficiency range (>80% for the 6 mm MgO: PPLN waveguide, >90% for the 3 mm MgO: PPLN waveguide) is rarely achieved in practice. At lower coupling efficiencies, it is obvious that the IC-FD is much more efficient than the single-pass FD.

3.5.3 DBR laser Facet Loading Consideration

As discussed in the previous section, facet degradation is the leading cause of the failure of high power laser diodes. In order to decrease the facet loading of high power LDs, a common method is to design and fabricate a super large optical cavity (SLOC) to reduce the local optical power density at the facets [89,90]. In addition, the large waveguide core will decrease the far field divergence angle in the fast axis such that the coupling efficiency from the LD to the MgO: PPLN waveguide can be further increased. We investigated the LD front facet (S_2) intensity loading by calculating facet intensities with the parameters of MgO: PPLN length and coupling efficiency at the fixed pump current of 700 mA. Fig. 3.10 shows the calculated LD front facet (S_2) intensities for different MgO: PPLN lengths of up to 1.2 cm and coupling coefficients from 30% to 100%. It is found that the shorter the MgO: PPLN waveguide, the greater the intra-cavity fundamental intensity. Compared with the single-pass FD device, where a LD right facet (S_2) reflectivity of 5% gives a facet loading of 17 MW/cm^2 (dotted reference line in Fig. 3.10), the IC-FD device always has a higher facet intensity. The extreme case is with 100% coupling efficiency and without the MgO: PPLN waveguide, in which the S_2 facet loading is doubled (35 MW/cm^2). Such a high facet intensity would easily cause the COMD of the DBR laser, as we estimated in the reported experimental results (30 MW/cm^2, Section 3.4.1). With a reasonable coupling coefficient of 70% and MgO: PPLN length of 6 mm, the facet intensity

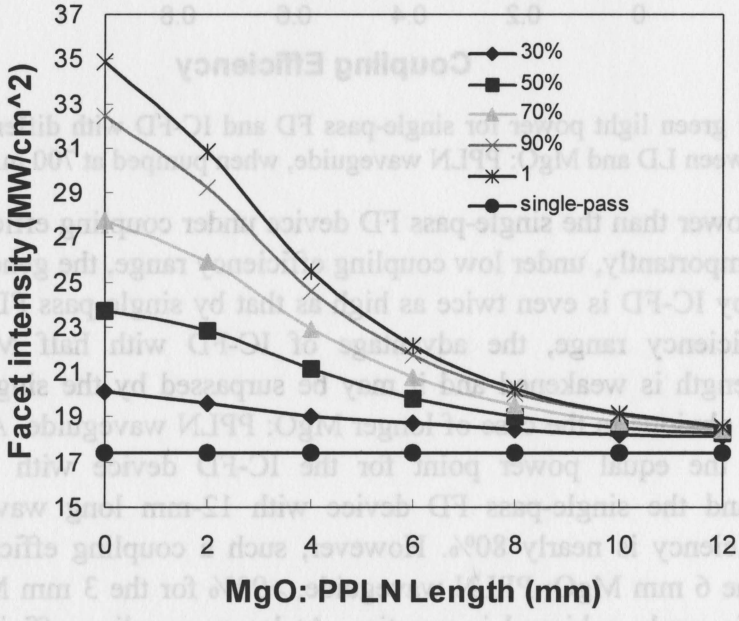

Fig. 3.10. DBR laser right facet fundamental intensity loading for different MgO: PPLN lengths with coupling efficiencies from 30% to 1, for the IC-FD device.

is calculated to be 21 MW/cm^2. This is only 24% higher than the single-pass configuration and is less susceptible to COMD. Therefore, in the optimization design of the IC-FD, the facet loading of he laser diode sets an upper constraint on the other parameters.

3.5.*4 Modulation Capability*

In this section we use the TDTW model to explore the dynamic characteristics of the proposed intra-cavity frequency doubled DBR-LD/MgO:PPLN green lasers. The modulated waveform of the green light power is calculated by direct current modulation of the LD section. Fig. 3.11 shows the square wave modulated green light with a modulation frequency of 100 MHz, current amplitude of 100 mA to 700 mA, and aspect ratio of 1:1. Due to the fast carrier lifetime of the semiconductor gain medium, and the high injection density (7.8 kA/cm^2) which results in a large small-signal gain, the modulation bandwidth is still high enough for scanning display systems [79], although a long cavity (L ≈ 1 cm with the 6 mm MgO:PPLN) is used. It should be mentioned that, parasitic parameters of the active region, which were not considered in the model, set another limitation on achieving the largest modulation bandwidth of the DBR-LD. An electrical modulation model could be incorporated into the TDTW model to fully describe the modulation characteristics of the proposed device.

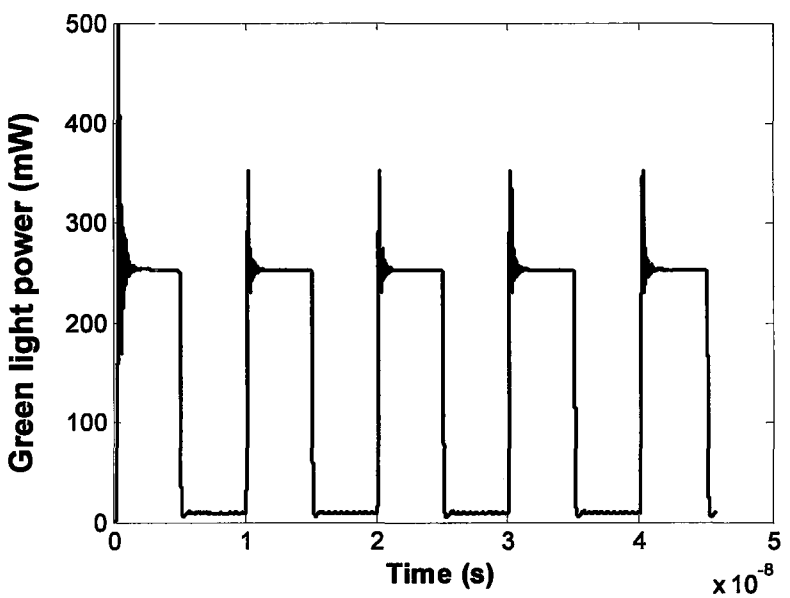

Fig. 3.11. Simulated square wave modulated green light for the IC-FD device.

3.6 Enhancement of SH Wave

There are two disadvantages of the proposed device, along with the reported single-pass frequency doubled DBR-LD/MgO:PPLN green lasers. One is the fabrication of MgO:PPLN waveguides, which shows both complexity and high loss. Second is the coupling of fundamental light from the DBR-LD to the waveguide and vise versa. IC-FD of semiconductor lasers with bulk MgO:PPLN crystal is a more elegant solution, as have been shown by the recent paper [44]. However, the low conversion efficiency is expected considering the large and divergent pump beam (due to the use of broad area laser diode with 100 to 200 μm emitting area width). Since the DBR-LD in our pervious calculation is with a single transverse mode, by collimating and focusing of the LD beam in the bulk MgO:PPLN crystal with proper lenses, it should get higher power conversion than that in [44]. In this calculation we still ignore the detail of the lenses and beam shape in the MgO:PPLN crystal and assume the beam is unchanged in beam spot size in the bulk crystal. Fig. 3.12 shows the green light power with respect to MgO:PPLN crystal length, for three beam diameters in the MgO:PPLN crystal. It is clear that the conversion efficiency drops dramatically with increasing the beam spot size in the MgO:PPLN crystal as a result of decreased fundamental beam intensity. For example, with the beam diameter of 30 and 50 μm in the MgO:PPLN, less than 50 mW is generated with crystal length as long as 1.2 cm. Therefore the IC-FD process with bulk MgO:PPLN is impractical. On the other hand, since the fundamental power is enhanced in the cavity, we can expect the enhancement of the SH power in the cavity as well by proper facet coating design. This enhancement can be accomplished, by partially reflecting of the 530 nm light at the right facet (S_4) of the bulk MgO:PPLN. Therefore both the fundamental and SH waves are significantly enhanced in the cavity and much more green light power can be extracted as well. To validate this, we simulated the green output power with power reflectivity of the S_4 facet at 530 nm, for the 6 mm long bulk MgO:PPLN crystal, which is shown in Fig. 3.13. It is clearly seen from this figure that when the facet S_4 is with higher reflectivity at 530 nm, the green light power is much more enhanced as expected. Temperature tuning curve for the 6 mm MgO:PPLN crystal in the IC-FD configuration is almost identical as in Fig. 3.8 by our calculation. However, it should be noticed that in this configuration both the fundamental and SH waves should satisfy the wavelength resonant conditions for the laser cavity, therefore more fine temperature control is needed.

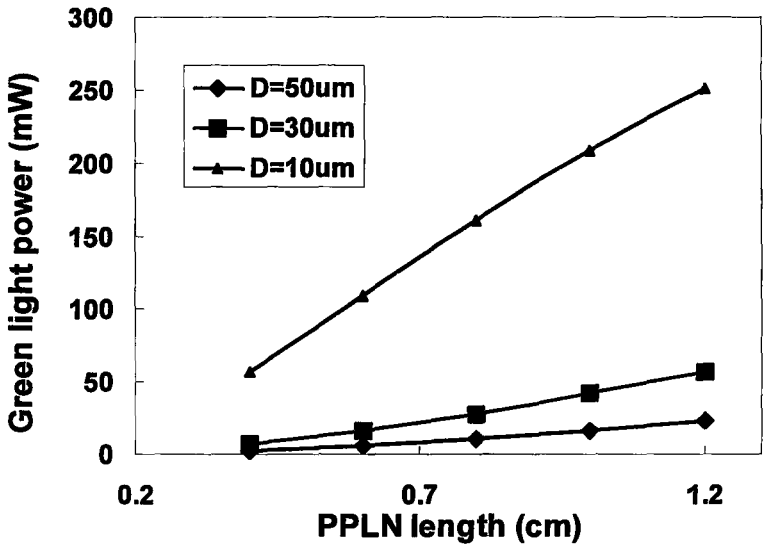

Fig. 3.12. Green light power with different MgO:PPLN waveguide length, for several beam diameters D. Pump current is 700 mA.

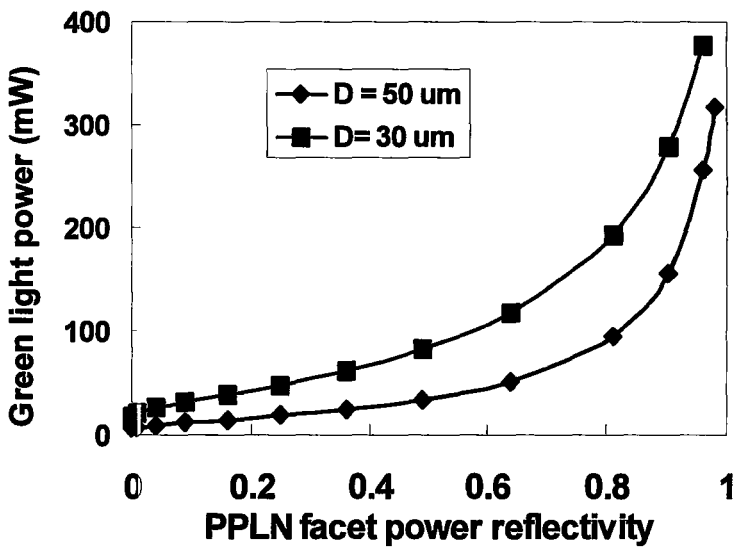

Fig. 3.13. Green output power with different power reflectivity of the S_4 facet at 530 nm, for two beam diameters in the MgO:PPLN crystal. Pump current is set to be 700 mA, and MgO:PPLN length is 6 mm.

3.7 Discussion and Summary

It is easily understood that our numerical simulation and design can be readily extended to the blue spectrum by the widely used 976 nm InGaAs high power laser diodes that generate 488 nm blue. Although the direct blue laser at 488 nm is almost ready for commercial applications, the direct 488 nm LD can still suffer from low power and low efficiency. Therefore the proposed device structure in this chapter can be extended to the design and fabrication of high efficient intra-cavity frequency doubled blue lasers as well.

To summarize, in this chapter, TDTW equations have been employed in the modeling of single-pass FD and IC-FD process in MgO: PPLN waveguide pumped by high power single-mode LDs. With properly chosen device and material parameters based on the reported results, the simulation results for single-pass FD of a high power semiconductor DBR-LD by the MgO:PPLN waveguide fit the published experimental results quite well. This validates the accuracy of the TDTW model in the modeling of FD process. An IC-FD configuration (intra-cavity frequency doubled DBR-LD/MgO:PPLN green laser) with similar components has been proposed and simulated accordingly. The simulations show that in the intra-cavity FD configuration, higher green output power and larger temperature tolerances can be achieved than those in the single-pass FD configuration, even as the MgO:PPLN waveguide length is reduced by half. The influence of coupling efficiency on the SHG power is less critical in the IC-FD than in the single-pass FD. The LD front facet intensity in the IC-FD device is found to be larger than that in the single-pass FD device, however, can still stay below the COMD value. The modulation of the proposed device at 100 MHz has been demonstrated by numerical calculation. And finally the enhancement of the SH wave in the bulk MgO:PPLN is discussed and shows that it is possible to use bulk MgO: PPLN crystal instead of waveguide to generate considerable green light powers, with the enhancement of the SH wave in the cavity.

CHAPTER 4

Optical Contact Nd:YVO_4/MgO:PPLN Green Laser Modeling and Experiment

4.1 Introduction

Optical contact Nd:YYO_4/MgO:PPLN green lasers are of great interest because of their small size and high efficiency in the last few years. As one of the promising green light sources in micro-projection systems, they are sometimes called microchip green lasers [77, 78, 91-96]. Optical contact Nd:YYO_4/MgO:PPLN green lasers are recently demonstrated [77, 78, 91-92], with the reported peak power of 500 mW and EO efficiency of >16% under modulation mode [78].

In this chapter we employ the plane-wave based coupled-wave equations to model intra-cavity frequency doubled DPSS lasers that have simple plano-parallel cavities. For low power and miniaturized intra-cavity frequency doubled DPSS lasers, where plano-parallel cavity structure is usually adopted such as the optical contact Nd:YVO_4/MgO:PPLN green laser, the plane-wave based coupled-wave model is a good approximation. Separated plano-parallel cavity structures [97], for instance, can also be modeled by the coupled wave equations. Furthermore, the developed plane-wave based coupled-wave model also allows us to explain the phase problem in optical contact Nd:YYO_4/MgO:PPLN lasers.

On the other hand, design of wide temperature operation of intra-cavity frequency doubled DPSS lasers has drawn much attention, especially when QPM nonlinear optical materials are used as frequency doublers [98-100]. A wider temperature operation tolerance will alleviate the need of accurate temperature controlling of the QPM crystal and the associated power consumption. It is well known that both the spectral and temperature bandwidth of QPM materials are narrow. This somehow undermines other advantages of QPM materials. Multi-section QPM gratings, chirped QPM gratings [98, 99] and aperiodic QPM gratings [100] are developed to realize a wide QPM bandwidth. In the last section we use the plane-wave model to design a multiple-section QPM grating and a chirped QPM grating which can be placed in the laser cavity.

4.2 Numerical Model

Starting from Eqs. (2.22-2.28), if we neglect both transverse spatial and time derivatives, the resulting plane-wave based coupled-wave equations in the laser crystal and nonlinear crystal are written as [101]

$$\pm\frac{dA_1^{\pm}}{dz}=\left[\frac{1}{2}g-\frac{1}{2}\alpha_0-jk_1\left(n^2-n_0^2\right)/n_0\right]A_1^{\pm}, \tag{4.1}$$

$$\pm\frac{dA_1^{\pm}}{dz}=-jk_1\chi^{(2)}A_1^{\pm *}A_2^{\pm}e^{\mp j\Delta_{SH}z}-\frac{1}{2}(\alpha_1+\alpha_{NL})A_1^{\pm}, \tag{4.2}$$

$$\pm\frac{dA_2^{\pm}}{dz}=-jk_1\chi^{(2)}A_1^{\pm 2}e^{\pm j\Delta_{SH}z}-\frac{1}{2}\alpha_2A_2^{\pm}. \tag{4.3}$$

The saturated gain in the laser crystal reads:

$$g=\frac{g_0}{1+I_1/I_{sat}}, \tag{4.4}$$

where I_1 is the total intensity of the fundamental wave in the cavity which relates to the forward and backward fundamental intensities by $I_i(r,z)=I_i^+(r,z)+I_i^-(r,z)$, and g_0 is the small-signal gain, related to the population inversion density ΔN (cm^{-3}) in the laser crystal through $g_0=\sigma\Delta N$.

Given a four-level laser, such as Nd:YVO_4 lasing at 1064 nm, the population inversion density ΔN is written as a z-dependent rate equation

$$\frac{d\Delta N(z)}{dt}=R_P(z)-\frac{\Delta N(z)}{\tau}-cg\left(\phi^+ +\phi^-\right), \tag{4.5}$$

where R_P is the pump rate ($cm^{-3}s^{-1}$) and ϕ is the photon density in the cavity (cm^{-3}), which is related to the envelope fields

$$\phi^{\pm}=I^{\pm}/ch\nu=\frac{1}{2}\varepsilon_0cn\left|A^{\pm}\right|^2/h\nu c=\frac{\varepsilon_0 n}{2h\nu}\left|A^{\pm}\right|^2, \tag{4.6}$$

where h is the Plank's constant, v is the frequency of the fundamental wavelength, n is the refractive index of the active material, and ε_0 is the permittivity in vacuum.

For end pump scheme, considering a uniform pump beam profile along z direction, the pump rate is simplified as

$$R_P(z) = \frac{2P_{in}}{h\nu_P} \frac{\alpha \exp(-\alpha z)}{\pi\omega_P^2[1-\exp(-\alpha l_1)]}, \tag{4.7}$$

where P_{in} is the incident pump power, α is the absorption coefficient at the pump wavelength, h is the Plank constant, ν_p is the pump frequency, and ω_{P0} is the pump beam waist radius.

Based on the single mode rate equation model and its steady state solutions [19, 63, 80, 102], an analytical expression for the SHG power of IC-FD is derived as [63]

$$P_{SHG} = \frac{A_1}{8B}\left[\sqrt{(2\alpha_0 L_1 + BI_s)^2 + 8BI_s(g_0 L_1 - \alpha_0 L_1)} - (2\alpha_0 L_1 + BI_s)\right]^2, \tag{4.8}$$

with

$$B = \frac{k\pi^2}{\varepsilon_0 c}\frac{A_1}{A_2}\frac{d_{eff}^2 L_2^2}{n_e^3 \lambda_1^2}, \tag{4.9}$$

where $k = 2$ for single-pass SHG, $k = 4$ for double-pass SHG, and A_1, A_2 are the cross-sectional areas of the fundamental beam in the active medium and in the nonlinear crystal, respectively.

4.3 Simulation and Comparison with Experiment

To validate the plane-wave model above, we compare the results from numerical simulation and experiment. The fourth-order Runge-Kutta method, a most often used numerical technique of the Runge-Kutta family, was used to calculate the forward and backward waves in Eqs. (4.1-4.5) until convergence was reached. Fig.4.1 shows the schematic structures of the optical contact Nd:YVO_4/MgO:PPLN green laser.

An 808 nm pump LD with an emitting area of 1 μm*100 μm (H*W) and power of 500 mW was collimated by a fast axis cylindrical micro lens. The resulting square spot emitting area with a divergence angle of 7 degree in both directions was then focused by a GRIN lens. The focused beam spot size on the Nd:YVO_4 was 70 μm. The monolithic optical contact Nd:YVO_4/MgO:PPLN green laser comprised a 3% doped Nd:YVO_4 of 0.5-mm-long and MgO:PPLN of 1-mm-long. The MgO:PPLN with an effective nonlinear coefficient of 17 pm/V was provided by the C2C Link Corp. The input facet was AR coated at 808 nm and HR coated for at 1064 nm and 532 nm (R<10%@808 nm, R>99.85%@1064 nm, 532 nm). The output facet was HR coated at 1064 nm and AR coated at 532

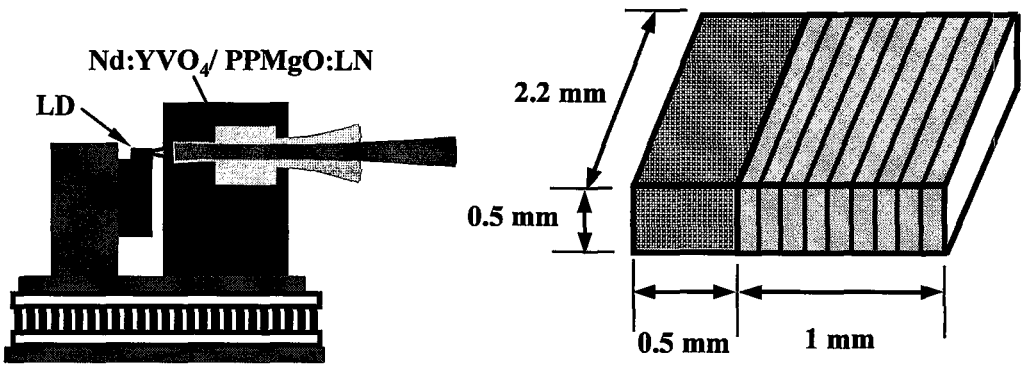

(a) (b)

Fig.4.1. (a) Packages of optical contact green lasers; and (b) the 3D device structure.

Table 4.1. Material parameters used in the simulation and experiment.

Parameters	Values
MgO:PPLN nonlinear coefficient (d_{33})	22 pm/V
Pump beam waist radius (ω_{P0})	70 μm
Total pump excitation efficiency (η)	70%
Fundamental absorption coefficient in Nd:YVO_4 (a_0)	0.01 cm^{-1}
Fundamental absorption coefficient in MgO:PPLN (a_1)	0.002 cm^{-1}
SH absorption coefficient in MgO:PPLN (a_2)	0.01 cm^{-1}
Green induced infrared absorption coefficient (a_{NL})	0.004 cm^{-1}
Saturation intensity of Nd:YVO_4 (I_s):	1260 W/cm^2
Fluorescence life time of Nd:YVO_4 (τ):	90 μs
Emission cross section of Nd:YVO_4 (σ)	30×10^{-19} cm^2

nm (R>99.85%@1064 nm, R<5%@532 nm). Due to the very small refractive index difference between the two materials, the optical contact interface between the Nd:YVO_4 and MgO:PPLN had a very small reflection coefficient (<0.002%). A TEC was used to control the temperature of the Nd:YVO_4/MgO:PPLN

structure.

Fig. 4.2 presents the comparison between measured green SHG power with respect to the 808-nm pump power, calculated SHG power from numerical simulations and analytical results. By adjusting the device parameters both numerical and analytical results are in good agreement with the experimental data.

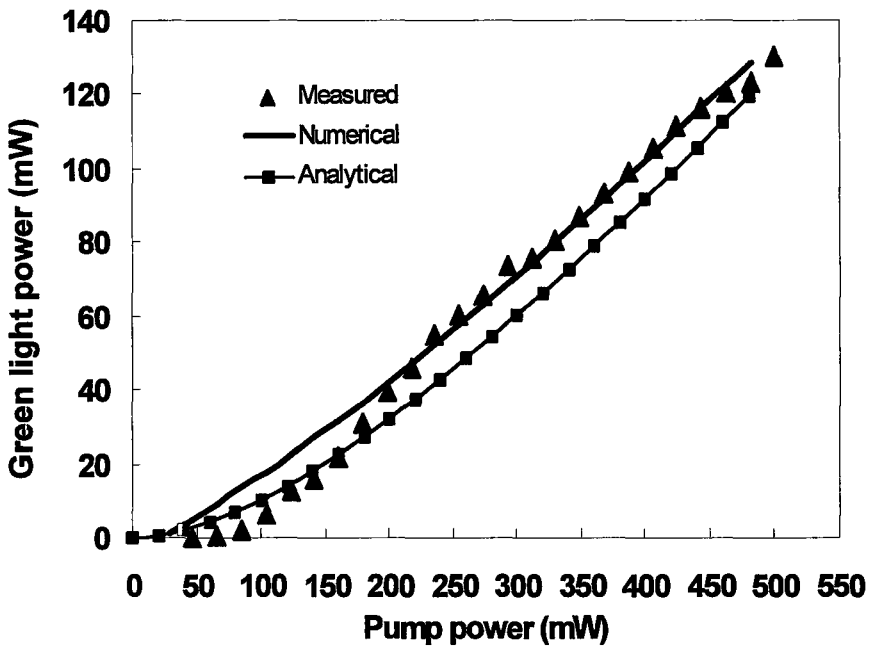

Fig. 4.2. Measured and calculated (numerical and analytical) green light power with pump power.

Heat dissipation problem may possibly explain the discrepancy at the low power region. Unfortunately it cannot be readily simulated by the plane-wave based model and analytical method. Fig. 4.3 presents the measured and calculated temperature tuning curves for the Nd:YVO_4/MgO:PPLN. We find that the experimental curve falls within the profile of the simulated one with the exception of multiple peaks in the former. We will examine this effect in the next section. Based on the comparisons we can generally conclude that the plane-wave model has the potential to simulate optical contact Nd:YVO_4/MgO:PPLN green lasers.

4.4 Phase Problem and Model Simulation

As discussed in section 4.3, for the optical contact Nd:YVO_4/MgO:PPLN green lasers, the simulated temperature tuning curve does not fit the experimental one very well at the top region as shown in Fig. 4.3. The experimental curve is not symmetric and has multiple peaks. Furthermore, by measuring different Nd:YVO_4/MgO:PPLN chips, or even measuring different positions of the input facet with the same chip, we find that their temperature tuning curves are different and not matched. Ideally for a perfect intra-cavity frequency doubled laser, the temperature tuning curve is approximately similar to that of a single nonlinear crystal. For the MgO:PPLN it should be a sinc-like curve.

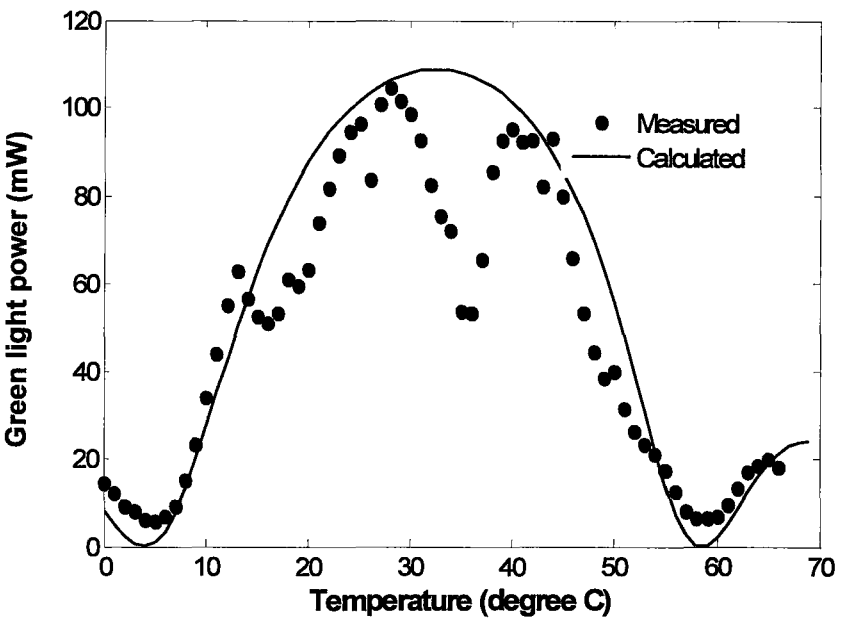

Fig. 4.3 Measured and calculated temperature tuning curve for the optically contacted device.

On the one hand we suspect that the mismatch may come from the fabrication problem of the device. This may be possibly true since both optical contacting fabrication process and MgO:PPLN poling technique are not quite mature [75]. For example, if the optical contacting quality is not perfect, the contacting interface between the Nd:YVO_4 and MgO:PPLN may result in some optical scattering or reflections. Consequently this region will have larger loss for the fundamental wave in the cavity and lead to low conversion efficiency. In addition, if the periodic poling aspect ratio is not perfect 1:1 somewhere in the MgO:LN, the effective nonlinear coefficient is not as high as the theoretical value.

However, these two fabrication-related problems should give lower SHG power within the whole temperature range instead of the pattern we have observed.

Then we expect that the mismatch may be caused by the phase problem in the IC-FD process in lasers [19]. In the modeling of intra-cavity frequency doubled Nd:YVO_4/MgO:PPLN green lasers, the relative phase of the fundamental and SH waves traveling back and forth in the cavity has significant impact on conversion efficiency and temperature bandwidth in the IC-FD. However, this phase problem has not received much attention. In the following part we will study the phase problem in further details based on the coupled-wave model. As will be explained below, the issue of mismatch between experimental temperature tuning curve and simulated curve is well addressed by the model.

4.4.1 Single-pass SHG Related Phase Problem

In common intra-cavity frequency doubled DPSS lasers, the SH wave is double-passed in the cavity, since one cavity end mirror at SH wavelength is AR coated while the other is HR coated. Therefore there may exist total power fluctuations because of the summation of forward and backward SH waves in the nonlinear crystals, if the HR coating and/or the gap between the nonlinear crystal and the HR coated end mirror introduce a phase difference of 0 to 2π between the forward and backward SH waves [19]. In the IC-FD process, the traveling of forward and backward SH waves can be treated equivalently as a double-pass SHG. The phase problem of double-pass SHG in a QPM crystal has been investigated [103]. It has been shown that due to the residual phase differences introduced in the last domain section (the last domain section is polished wedged, as schematically indicated in Fig. 4.4(a), the SHG power fluctuates periodically with the pump beam spot scanning along the transverse position of the periodically poled nonlinear crystal (y direction). In the experiment, we do not know exactly the last residual domain dimension at the edge of the MgO:PPLN crystal, because the end fact is assumed to be parallel to the domain boundary (YZ plane) in the crystal polishing process. Practically they are not ideally parallel and should show some residual phase difference when the pump beam scans along y direction, as is sketched in Fig. 4.4.

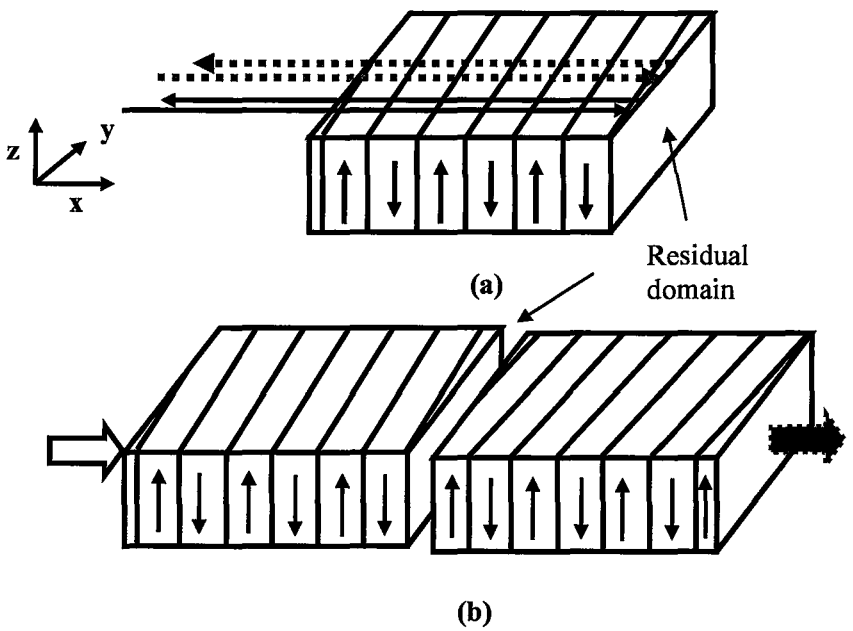

Fig. 4.4. Schematic double-pass SHG in a single MgO:PPLN crystal. Solid lines: fundamental waves; Dotter lines: SH waves. (b) Two identical MgO:PPLN chips in series.

In the experiment we tried to repeat the double-pass SHG, similar to the one in [103]. However, due to the critical beam alignment problem, the forward and backward fundamental beams could not overlap perfectly throughout the MgO:PPLN crystal. Thus the generated forward and backward SH beams could not add constructively or destructively. Alternatively, in the experiment we chose to use single-pass SHG, where two MgO:PPLN chips (with AR coatings at both facets) with the same period (QPM temperature at 60°C) were used in series to mimic the double-pass SHG. The schematic chip dimensions of the two MgO:PPLN chips are shown in Fig. 4.4(b). Such an arrangement has the

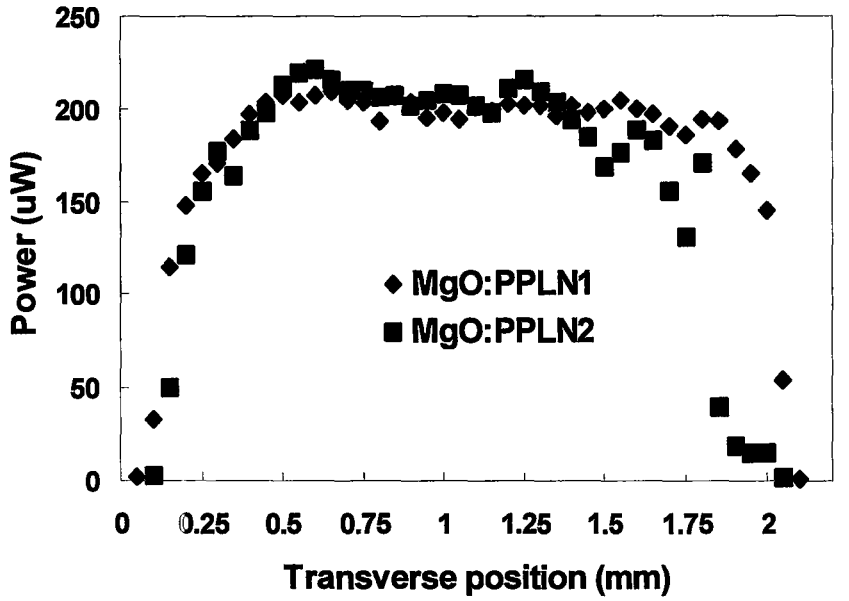

Fig. 4.5. (a) Single-pass SHG power with y direction scanning for two MgO:PPLN chips.

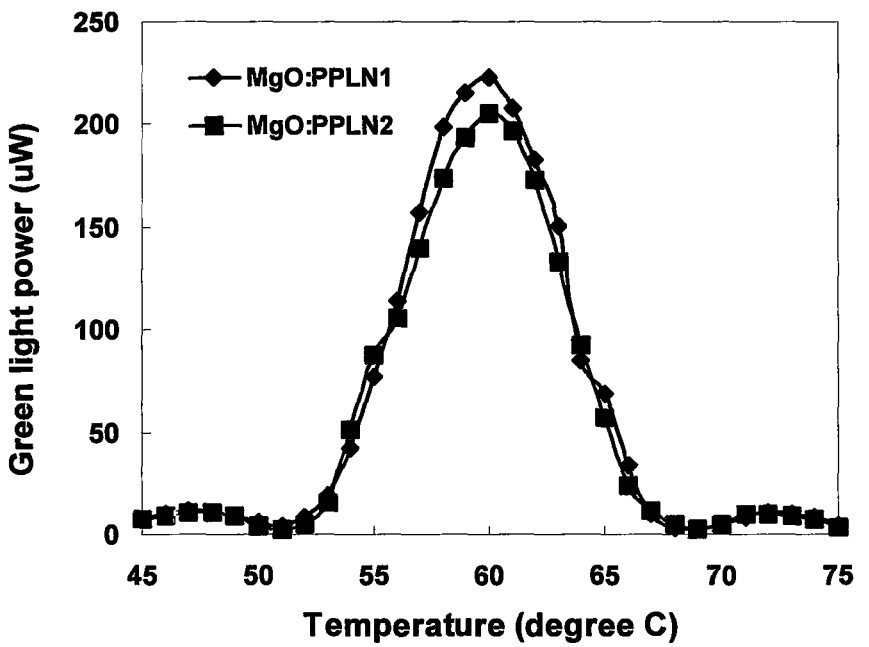

Fig. 4.5. (b) Temperature tuning curves for these two chips, respectively.

advantage of easy alignment over the double-pass SHG experiments, because the

fundamental Gaussian beam passing through the successive chips is "continuous", contrary to the double-pass SHG where the backward beam is reflected by the flat facet and will usually changes the shape of the forward beam, making the forward and backward beams non-overlapping.

Fig. 4.5(a) shows the single-pass SHG power by y direction scanning of two 3-mm-long MgO:PPLN chips at fixed temperature of 60°C (QPM temperature for the two chips). Fig. 4.5 (b) shows the temperature tuning curves for these two chips, respectively. It seems that the two chips are roughly identical and the periodical poling along y direction is of good quality since the SHG powers are relatively flat. Next, the two chips are placed in series and we again scan the pump beam along y direction at two temperatures 60°C and 57°C, respectively, as shown in Fig. 4.6. It can be seen that the SH power fluctuates periodically along y direction, contrast to that in Fig. 4.5(a). From Fig. 4.5(b) we can also notice that these two temperatures are corresponding to the maximum (60°C) and one HWFM temperature point (57°C).

We further investigate the temperature tuning curve at certain y positions. The pump beam has been focused at four equally spaced points on the y-axis between 1 mm and 1.5 mm, denoted as a, b, c, d of the 60°C curve in Fig. 4.6. This corresponds to the four phase differences (0, $\pi/2$, π, and $3\pi/2$) between the two propagating SH waves in two MgO:PPLNs at 60°C. The corresponding temperature tuning curves with respect to phase difference are illustrated in Fig. 4.7(a). Due to the constructive or destructive summation of the SH waves, the temperature tuning curves do not resemble a sinc function. At the QPM temperature (60°C), the SHG power for the two MgO:PPLN chips in series may even be minimized (when the phase difference for the two SHG waves are π). In Fig. 4.7 (b), we applied the plane-wave model to calculate the temperature tuning

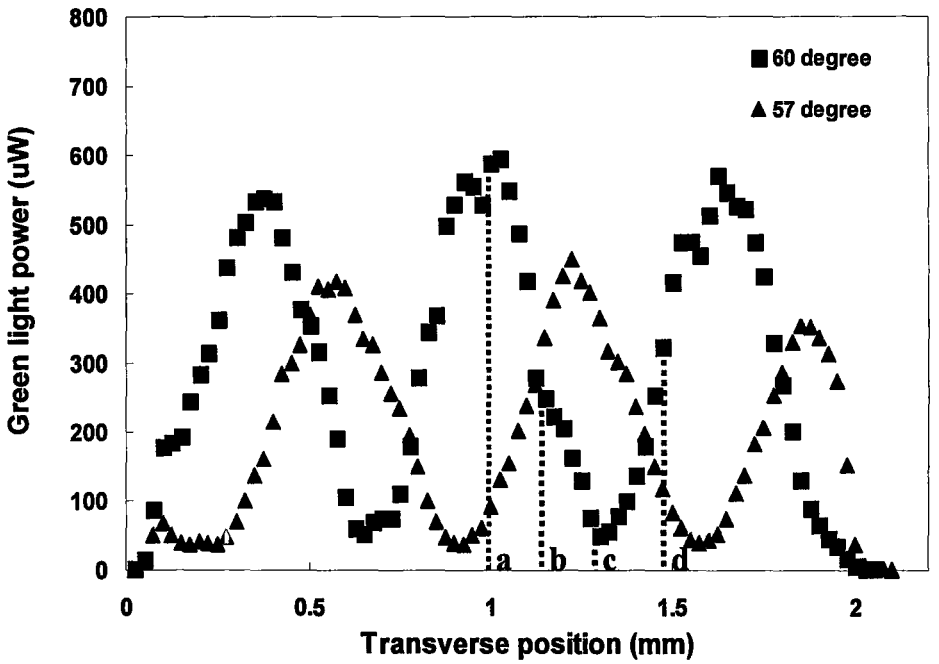

Fig. 4.6. SHG power by scanning y direction of the two MgO:PPLN in series, at two different temperatures.

curve with two MgO:PPLN in series. In the simulation the phase of the

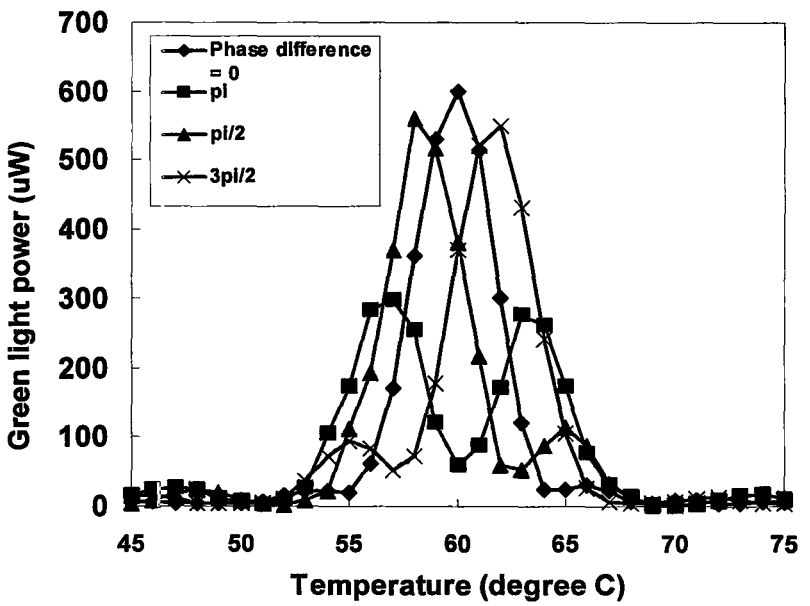

Fig.4.7. (a) Temperature tuning curves at 4 points indicated in Fig. 4.6.

fundamental and SH waves was considered and the calculation was performed

domain by domain. We varied the residual domain length for one MgO:PPLN and calculated the associated temperature tuning curve. We find that by changing the residual domain of the first PPLN, the associated phase difference for the two SH waves changes as well. As a result, the temperature tuning curves in Fig. 4.7 (b) fit the measured curves reasonably well.

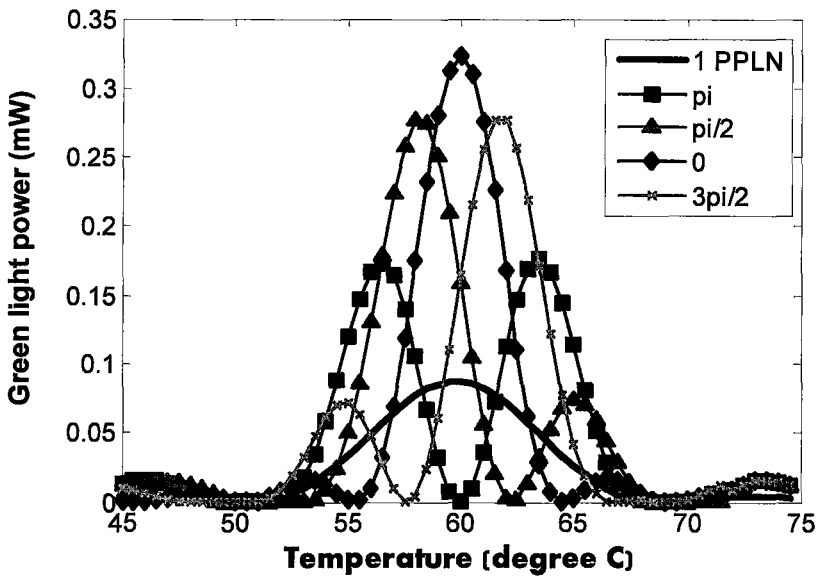

Fig.4.7. (b) Simulated temperature tuning curves with 4 phase corresponding to the 4 different positions in Fig. 4.6.

4.4.2 Phase Problem in Optical Contact Nd:YYO_4/MgO:PPLN Green Lasers

Since the SH wave in the QPM grating for the IC-FD process is inherently the same as that in the double-pass SHG, we expect to observe such temperature tuning curve phenomenon in the intra-cavity frequency doubled DPSS lasers as well. We investigated the optical contact Nd:YYO_4/MgO:PPLN green laser as an example since the device dimension is small and more compact, which helps to eliminate mechanical alignment problem during experiments. Fig. 4.8 shows the

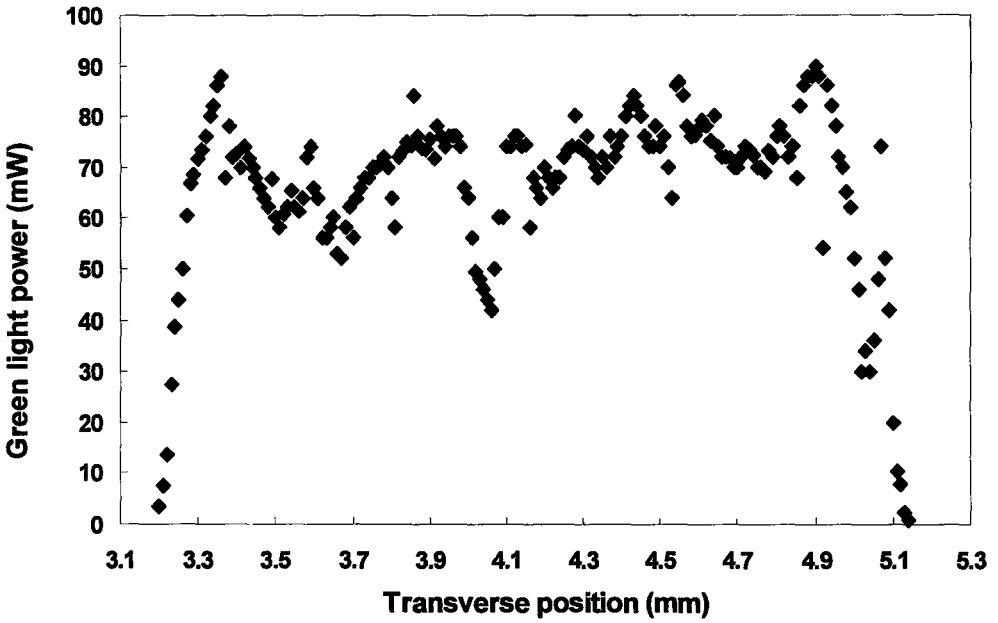

Fig. 4.8. Green power with the scanning of y direction for the optical contact green laser.

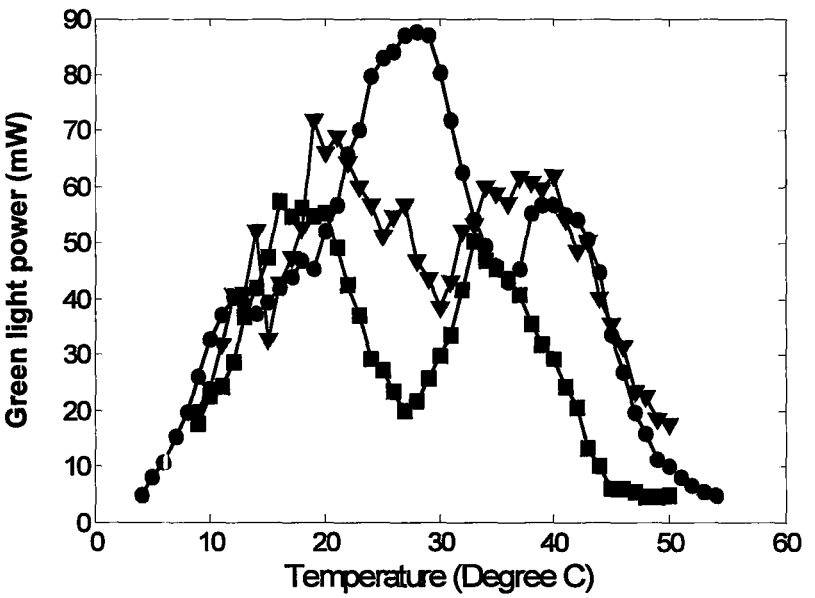

Fig. 4.9. Measured temperature tuning curves at three different y positions.

green light power with y direction scanning of the pump beam (500 mW) at a fixed temperature (30°C). From this figure it is not clear whether periodic power oscillations exist or not as in Fig. 4.6, therefore it is not clear if the fluctuation is

related to the phase problem or due to optical contacting interface imperfection, or both.

Additionally temperature tuning curves are measured at several positions, as shown in Fig. 4.9. Although not as clear as that in Fig. 4.7(a), we are confident that there exists phase problem in the optical contact Nd:YYO_4/MgO:PPLN green laser chips.

To further confirm our expectation, we use the plane-wave model to simulate the temperature tuning curves with and without taking into account the phase problem. The calculated results in Fig. 4.10 qualitatively show that by varying the residual domain phase difference, the induced temperature tuning curve deviates from that without considering phase difference in the calculation. The temperature bandwidth is essentially the single-pass curve without phase consideration. With properly chosen residual phase ($11\pi/6$), the temperature tuning curve has three peaks within the single-pass bandwidth profile and roughly coincides with the measured curve.

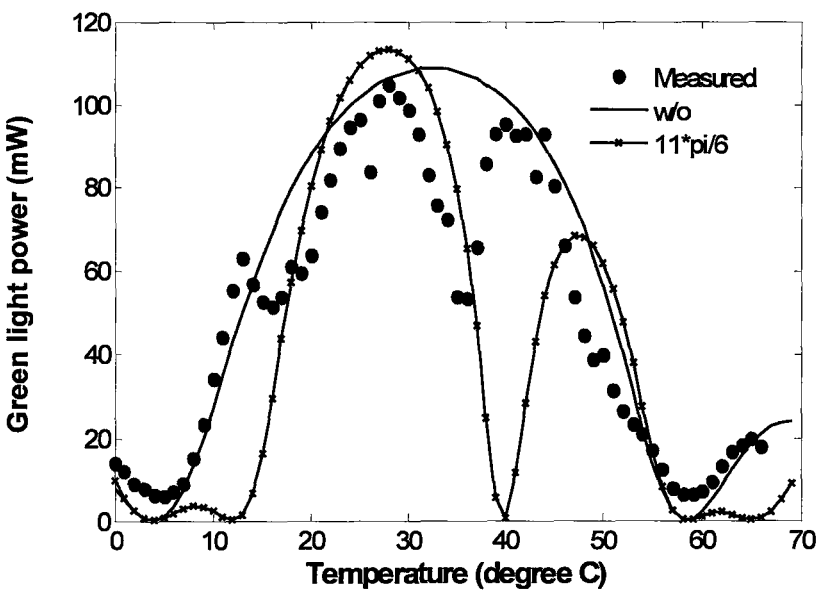

Fig. 4.10. Simulated temperature tuning curves with and without considering residual phase difference for the SH waves introduced at the end residual domain. The measured result in Fig. 4.2 is also shown in the figure for comparison.

Fig. 4.11 shows the forward and backward SH power distributions in the optical contact structure for one residual phase ($8\pi/6$), when the device is operated under the QPM temperature (32°C). This clearly shows power "flow-back" from

second-harmonic to fundamental when the backward SH wave is reflected back in the forward direction.

The unusual temperature tuning curves for optical contact Nd:YVO_4/MgO:PPLN green lasers add to operation complexity in real applications. However, as a result of imperfect alignments during facet polishing, we can always find a proper area or positions that have more symmetric temperature tuning curves.

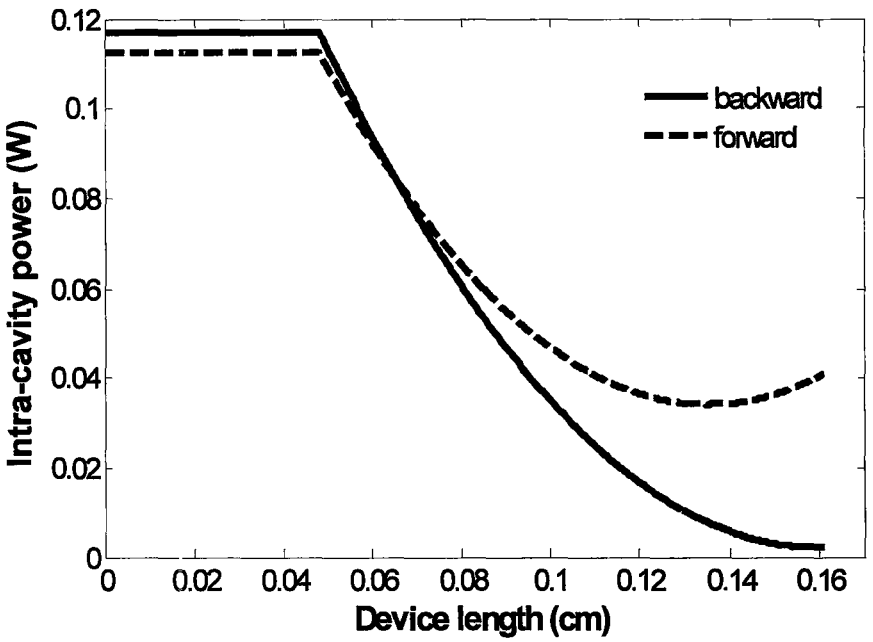

4.5 Design of Wide Temperature Operated Nd:YVO_4/MgO:PPLN Green Lasers

As we have seen, the plane-wave based coupled-wave equations have been successfully employed to model the performance of low power and miniaturized Nd:YVO_4/MgO:PPLN green Lasers. Furthermore, we can use this model to design various QPM gratings and the related intra-cavity frequency doubled lasers. In particular, it is well known that with specially designed QPM gratings, their temperature tolerance can be enlarged. For example, for the multiple-section QPM grating, several gratings with different grating periods are cascaded such that the spectral and temperature bandwidths are broadened. Chirped QPM

gratings [98, 99] and aperiodic QPM gratings [100] are also investigated, however, their fabrication is more difficult. In this section, we use the numerical model to calculate the temperature bandwidth of such QPM gratings within the DPSS laser cavity.

As one example, we calculate a multiple-section QPM grating with 3 periods of 6.95-μm, 6.97-μm and 6.99-μm. Each period corresponds to the QPM temperature of 17°C, 30°C and 43°C. Each QPM grating consists of 360 periods (2.5 mm). The total cascaded device is 7.5-mm long. Fig. 4.12 shows the calculated temperature tuning curves of the associated DPSS laser with the designed multiple-section grating. The total temperature bandwidth is roughly 40°C. As a comparison, each grating curve representing the period of 6.95-μm, 6.97-μm and 6.99-μm is also presented in the figure. This clearly demonstrates the coherent summation of the three QPM gratings in the cavity. In practical design special care should be taken to ensure that the grating period, grating length (domain numbers), and grating numbers are properly chosen. In contrast, a bad design of multiple-section QPM grating is also shown in Fig. 4. 13. The three gratings have the same periods as those in Fig. 4.12, but the number of periods is 320 (2.32-mm) for all of them.

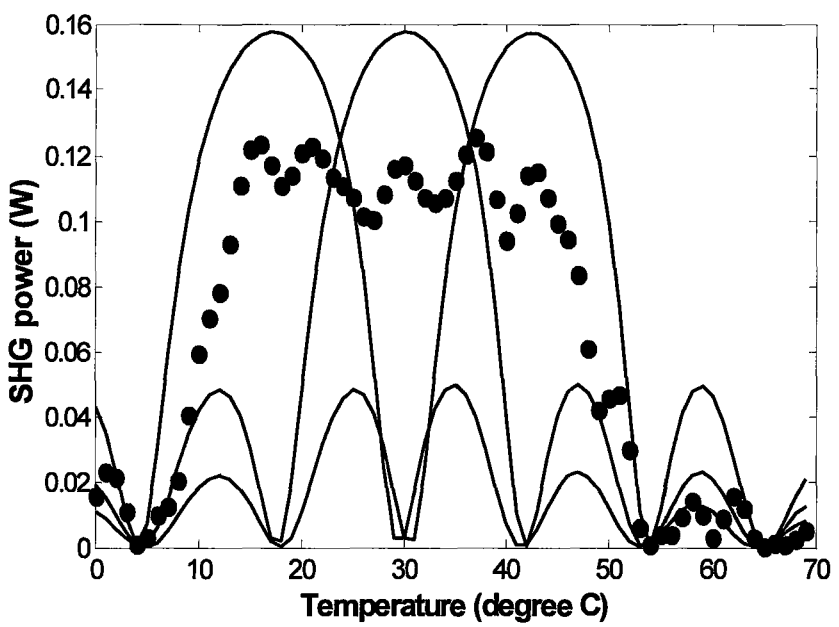

Fig. 4.12. Calculated temperature tuning curve (dotted) for the IC-FD process with a multiple-section QPM grating. Solid lines represent tuning curves of three individual gratings.

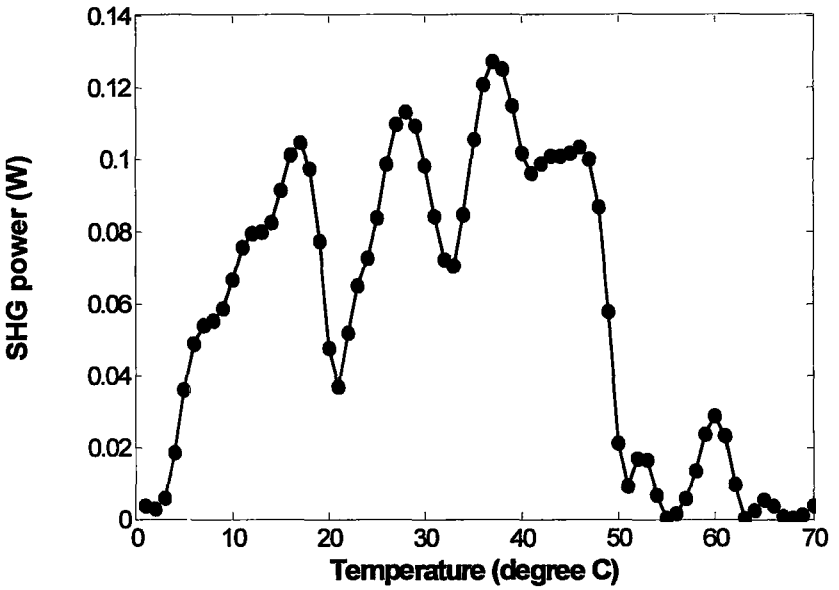

Fig. 4.13. Calculated temperature tuning curve for the IC-FD process with another multiple-section QPM grating. The temperature tuning curve is not good.

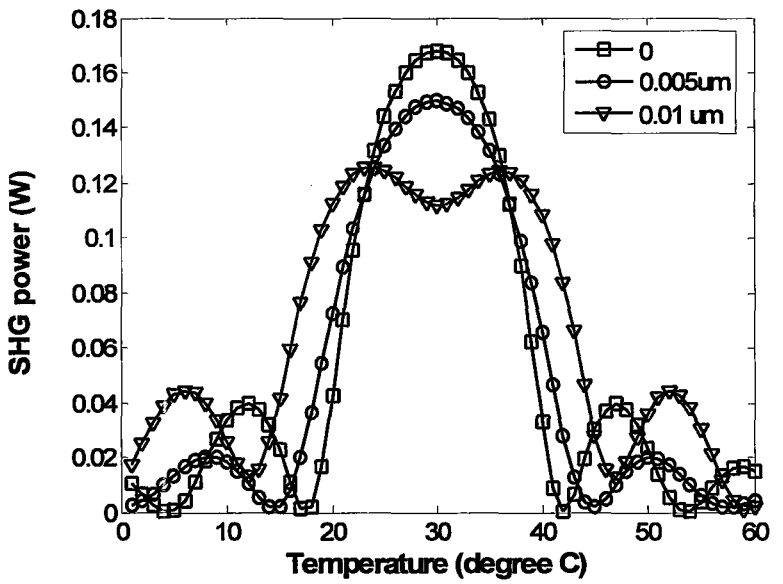

Fig. 4.14. Calculated temperature bandwidth for 2.5-mm-long un-chirped and chirped QPM gratings.

As a second example, a linear chirped QPM grating is calculated. The QPM grating of 2.5-mm-long has an average period of 6.97 μm. The total period chirp amount is set to be 0.005 μm and 0.01 μm. Fig. 4.14 shows the temperature tuning

curves with the defined chirp values. A broadened temperature bandwidth is associated with decreased power. It is also found that with the increasing of chirp amount, the curve peak is more flat or even drops.

In practice, the lithography accuracy limits the fabrication of linear chirped QPM grating and an alternative method considered here is an equivalent 'chirping" of the QPM grating. This can be accomplished by introducing a temperature gradient along the QPM grating direction. Suppose the temperature along the QPM grating direction is linearly distributed, the temperature dependent dispersion of the nonlinear crystal will introduce an effective grating period chirp. This temperature gradient could be accomplished with appropriate metal holder design. Based on this assumption and without loss of generality, we simply introduce temperature gradients of 0.1°C and 0.2°C along the MgO:PPLN crystal, and calculate the temperature tuning curves. The MgO:PPLN is 3 mm and the pump power is 0.5 W. Fig. 5.15 shows the temperature tuning curves of the 3-mm MgO:PPLN in the cavity with and without temperature chirp. It is found that with a slight temperature chirp of 0.3°C, the temperature tuning bandwidth enlarges from 12°C to 22°C. The associated peak power decreases from 130 mW down to 90 mW. Larger temperature chirp along z direction of the nonlinear crystal could be achieved with proper metal holder and heat sink design.

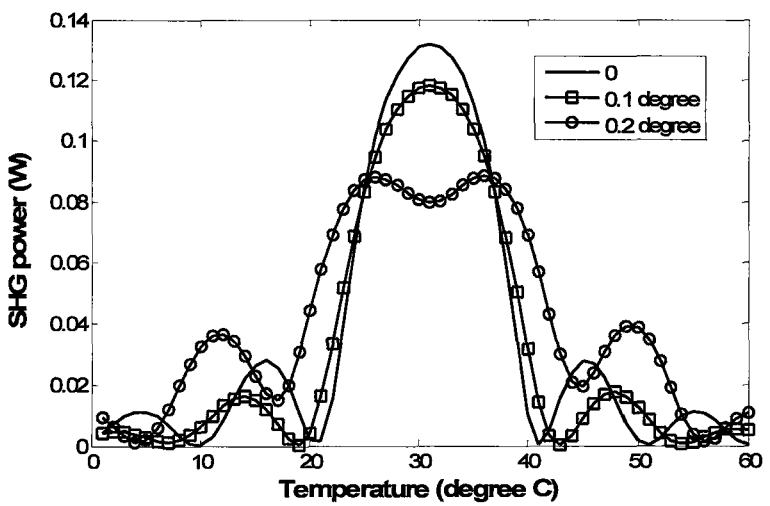

Fig. 4.15. Calculated temperature bandwidth for the 3-mm-long QPM grating.

4.6 Summary

In this chapter, plane-wave based coupled-wave equations are implemented to model intra-cavity frequency doubled Nd:YVO_4/MgO:PPLN green lasers. The model is validated by the experimental results. Based on this numerical model, phase problem in the optical contact Nd:YVO_4/MgO:PPLN green laser is explored in detail. In particular, the temperature tuning curve is calculated and agrees with the measured curve fairly well after the phase is taken into account, which reinforces the accuracy of our model. Finally three design examples of wide temperature operated Nd:YVO_4/MgO:PPLN green lasers have been demonstrated with the derived numerical model.

CHAPTER 5

BULK Nd:YVO_4/MgO:PPLN GREEN LASER MODELING AND DESIGN

5.1 Introduction

In addition to the miniature Nd:YVO_4/MgO:PPLN green lasers described in the previous chapter, we have carried out bulk Nd:YVO_4/MgO:PPLN green lasers as well. The bulk Nd:YVO_4/MgO:PPLN green laser can generate Watt-level power, especially suitable for high power laser display applications. Due to its plano-concave cavity structure, the optical modal field formed in the cavity generally varies along the beam propagation direction. Therefore assuming plane waves in the cavity is not valid any more. This chapter employs a three-dimensional (3D) coupled wave model to investigate this type of intra-cavity frequency doubled DPSS laser. Some experimental results on the constructed bulk Nd:YVO_4/MgO:PPLN green lasers are presented to compare with numerical calculations from the 3D model. Thermal effects including thermal lensing and thermal de-phasing, present in the laser crystal and nonlinear crystal, is also modeled with the 3D model incorporating a two-dimensional (2D) heat equation.

Currently analytical solutions are widely adopted to design intra-cavity frequency doubled DPSS lasers [19, 80, 102]. However, the analytical expression can only give limited information on optimizing the performances of such lasers. Only lumped device parameters such as effective nonlinear coefficient, cavity loss, and nonlinear crystal length are considered in the analytical results. Other important specifications, such as temperature tolerance, pump beam size and cavity length, cannot be easily derived by this method. In addition, rate equations considering spatial distributions for the fundamental and SH beams have been employed [104] to simulate the passive/active Q-switched, intra-cavity frequency doubled Nd:$GdVO_4$/KTP laser, however, the phase matching condition and pump non-depletion approximation are always assumed in the simulation.

As discussed in Chapter 2, we have derived the full 3D time-domain traveling wave (TDTW) equations in both the laser and nonlinear media, which can be used to model solid state lasers. However, because of the low spontaneous

emission lifetime (μs) of DPSS lasers, the TDTW model is not that efficient as it requires long calculation time by marching both in time and space before convergence is reached. Therefore, the time-independent 3D coupled wave equations neglecting the time dependent derivatives are more efficient and appropriate. This 3D model can fully describe the interaction of fundamental and SH waves in the cavity, and provide much more useful information on the optimization design of such lasers. 3D coupled-wave model has already been established to simulate CO_2 lasers [64] and solid-state lasers [65]. To the best of our knowledge, 3D description of IC-FD process of DPSS lasers has not been previously studied and developed.

Compared with analytical and traditional rate equations, a 3D coupled-wave model has the following merits. First, it can trace characteristics along the propagation direction (z direction), which is especially suitable for analyzing a variety of QPM grating structures (This can also be treated by the plane-wave model implemented in the previous chapter). Second, it can simulate various solid-state laser cavity structures, e.g. concave-concave, plano-concave, and plano-parallel cavities. Third, other dimension-dependent characteristics, for example, thermal lensing and thermal de-phasing, as will be briefly discussed in the last section of this chapter, can be incorporated into the 3D model to explain thermal related problems.

5.2 Three-Dimensional Coupled-Wave Model

5.2.1 Laser Crystal

Let's consider a birefringent, uniaxial laser crystal such as Nd:YVO_4, which is arranged in such configuration that the light propagates along the a-axis and polarizes along the c-axis, and a uniaxial nonlinear crystal such as MgO:PPLN which is arranged in such orientation that the light propagates along the x-axis and polarizes along the z-axis. Using the time-domain traveling equations in Chapter 2 (2.21, 2.26), and neglecting the time-dependent terms by assuming time-independent slow varying envelope amplitudes (2.16), the spatially-dependent forward and backward fundamental amplitudes in the laser are [65]:

$$\pm\frac{\partial A_1^{\pm}(r,z)}{\partial z}=\frac{1}{2jk_1}\nabla_T^2 A_1^{\pm}(r,z)+\left[\frac{1}{2}g(r,z)-\frac{1}{2}\alpha_0-jk_1\left(n^2(r,z)-n_0^2\right)/n_0\right]A_1^{\pm}(r,z), \tag{5.1}$$

where $r = (x, y)$ is the transverse coordinate and z is the longitudinal coordinate.

The saturated gain in the laser crystal reads:

$$g=\frac{g_0}{1+I_1/I_{sat}}, \tag{5.2}$$

where I_1 is the total intensity of the fundamental wave in the cavity which relates to the forward and backward fundamental intensities by $I_i(r,z)=I_i^+(r,z)+I_i^-(r,z)$ and g_0 is the small-signal gain, related to the population inversion density ΔN (cm^{-3}) in the laser crystal through $g_0=\sigma\Delta N$.

Considering a four-level laser such as Nd:YVO_4 lasing at 1064 nm, the population inversion density ΔN is written as a spatially-dependent rate equation

$$\frac{d\Delta N(r,z)}{dt}=R_P(r,z)-\frac{\Delta N(r,z)}{\tau}-cg\left(\phi^+ +\phi^-\right), \tag{5.3}$$

where R_P is the pump rate ($cm^{-3}s^{-1}$), ϕ is the photon density in the cavity (cm^{-3}), which is related to the envelop fields

$$\phi^{\pm}=I^{\pm}/ch\nu=\frac{1}{2}\varepsilon_0 cn\left|A^{\pm}\right|^2/h\nu c=\frac{\varepsilon_0 n}{2h\nu}\left|A^{\pm}\right|^2, \tag{5.4}$$

where h is the Plank's constant, ν is the frequency of the fundamental wavelength, n is the refractive index of the active material, and ε_0 is the permittivity in vacuum. The total power along the cavity is related to the intensity by

$$P^{\pm}(z)=\int_0^{+\infty} I^{\pm}(r,z)\cdot 2\pi r dr. \tag{5.5}$$

For end pump scheme, the 3D CW pump rate in the cavity is assumed to be a super Gaussian beam distribution [105]:

$$R_P(r,z)=\frac{P_{in}}{h\nu_P}\frac{2\alpha\exp(-\alpha z)}{\pi\omega_P^2(z)[1-\exp(-\alpha l_1)]}\exp\left[-\frac{2r^2}{\omega_P^2(z)}\right], \tag{5.6}$$

where P_{in} is the incident pump power, α is the absorption coefficient at the pump wavelength, h is the Plank constant, ν_p is the pump frequency, and $\omega_P(z)$ is the radius of the pump beams at z. On the basis of paraxial approximation, the radius of the pump beam in the cavity may be given by

$$\omega_P(z)=\omega_{P0}\left\{1+\left[\frac{M^2\lambda_P(z-z_0)}{\pi\omega_{P0}}\right]^2\right\}^{1/2}, \tag{5.7}$$

where ω_{P0} is the pump beam waist radius, z_0 is the position of the pump beam waist, λ_P is the pump wavelength, and M^2 is the pump beam quality factor.

5.2.2 Nonlinear Crystal

According to Eq. (2.23), (2.24), (2.27), (2.28) and using the same procedure of deriving (5.1), the nonlinear interactions for the forward and backward fundamental and SH waves in the QPM grating read [106]

$$\begin{aligned}\pm\frac{\partial A_1^{\pm}(r,z)}{\partial z}&=\frac{1}{jk_1}\nabla_T^2A_1^{\pm}(r,z)\\&\quad-jk_1\chi^{(2)}A_1^{\pm*}(r,z)E_2^{\pm}(r,z)e^{\mp j\Delta_{SH}z}-\frac{1}{2}(\alpha_1+\alpha_{NL})A_1^{\pm}(r,z)\end{aligned}, \tag{5.8}$$

$$\begin{aligned}\pm\frac{\partial A_2^{\pm}(r,z)}{\partial z}&=\frac{1}{jk_2}\nabla_T^2A_2^{\pm}(r,z)\\&\quad-jk_1\chi^{(2)}\left[A_1^{\pm}(r,z)\right]^2e^{\pm j\Delta_{SH}z}-\frac{1}{2}\alpha_2A_2^{\pm}(r,z)\end{aligned}. \tag{5.9}$$

5.2.3 Curved Mirror

For most conventional solid-state lasers, concave mirrors are introduced in various laser cavity configurations to model the curved end mirror boundary. The beam propagating towards it can be simplified as a change of the phase front [66],

$$E_i^-(r,L) = E_i^+(r,L)\sqrt{R_2}\exp\left(\frac{jk_i r^2}{2f}\right), \tag{5.10}$$

where f is the focal length of the concave mirror and R_2 is the power reflectivity. The left planar facet boundary condition is given by

$$E_i^-(r,0) = E_i^+(r,L)\sqrt{R_1}\,. \tag{5.11}$$

5.3 Numerical Implementation and Device Parameters

A schematic plano-concave cavity structure is shown in Fig. 5.1 (a). In the first step of simulation, starting from an arbitrary forward propagating electrical field profile at the left facet, the transverse mode profile is calculated through the diffraction term ∇_T^2 in Eq. (5.1), with the beam propagation method [64-66, 106]. Here a fast Fourier transform method is employed [64, 67]. The second step is to deal with gain/loss and phase terms in Eq. (5.1), which is calculated by the fourth-order Runge-Kutta method. Pump rate equation (5.6) and steady state population inversion equation (5.3) are pre-calculated in each section of the laser crystal by letting $d\Delta N/dt = 0$, forming a steady population inversion distribution. The same procedure is used at the time when the electrical fields propagate in the MgO: PPLN, where both fundamental and SH waves are calculated simultaneously through Eq. (5.8) and (5.9). After the forward propagating fields reach the output coupler (OC) and get reflected by (5.11), the generated backward propagation fields are repeatedly calculated through (5.1)-(5.9). In the numerical method, we assume a single longitudinal mode lasing at the fundamental wavelength and neglect the spatial hole burning effect due to the slow-varying envelope approximation.

Table 5.1. Material parameters used in the simulation and experiment

Parameters	Values
MgO:PPLN nonlinear coefficient (d_{33})	22 pm/V
Pump beam waist radius (ω_{P0})	120 μm
Pump beam quality factor (M^2)	10
Total pump excitation efficiency (η)	70%
Fundamental absorption coefficient in Nd:YVO_4 (a_0)	0.01 cm^{-1}
Fundamental absorption coefficient in MgO:PPLN (a_1)	0.01 cm^{-1}
SH absorption coefficient in MgO:PPLN (a_2)	0.01 cm^{-1}
Green induced infrared absorption coefficient (a_{NL})	0.004 cm^{-1}
Two-photon absorption coefficient (β)	$2\text{-}5\times10^{-9}$cm/W
Thermal conductivity of Nd:YVO_4 (K_1)	6 $W\cdot cm^{-1}K^{-1}$
Thermal conductivity of MgO:PPLN (K_2)	4 $W\cdot cm^{-1}K^{-1}$
Saturation intensity of Nd:YVO_4 (I_s):	1260 W/cm^2
Fluorescence life time of Nd:YVO_4 (τ):	90 μs
Emission cross section of Nd:YVO_4 (σ)	30×10^{-19} cm^2

Table 5.2. Device parameters used in the simulation and experiment

Parameters	Values
Nd:YVO_4 length (L_1)	2 mm
MgO:PPLN length (L_2)	1, 2, 3 mm
Total cavity length (L)	1 cm
Coating of left facet of Nd:YVO_4 (S_1)	T= 98%@808 nm R=99.85%@1064 & 532 nm
Coating of right facet of Nd:YVO_4 (S_2)	R=99.85%@532 nm T=99.85%@1064 nm
Coating of both facets of MgO:PPLN (S_3&S_4)	T=99.85%@ 532 &1064 nm
Coating of the OC (S_5)	R=99.85%@1064 nm T=95%@532 nm

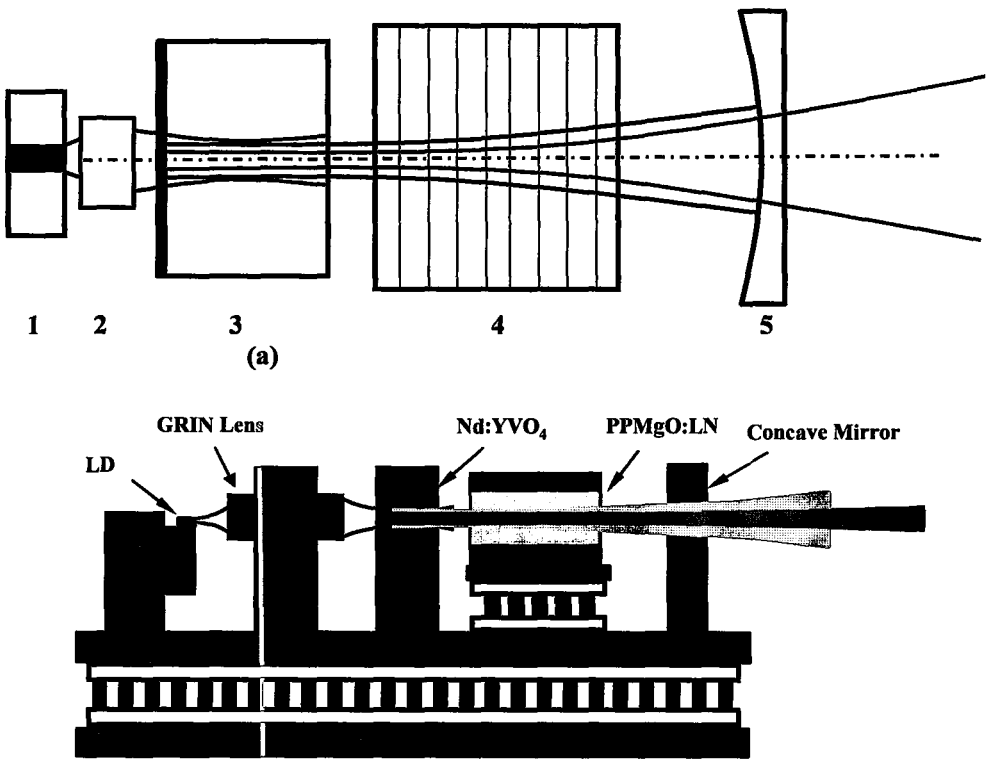

Fig.5.1 (a) Schematic device structure of the Nd:YVO_4/MgO:PPLN green laser: 1. pump LD, 2 GRIN lens, 3. Nd:YVO_4, 4. MgO:PPLN, 5. Output coupler; and (b) schematic package of the Nd:YVO_4/MgO:PPLN green laser. Metal holders are made of copper.

A schematic package of the device is shown in Fig. 5.1(b). An 808 nm pump LD with power of 2.8 W (at 3A) was collimated by a fast-axis cylindrical micro-lens. The resulting square beam spot of approximately 100 by 100 μm with a divergence angle of 7 degree in both directions was then focused by a GRIN lens with a 0.29 pitch. A 1% doped, 2-mm-long, and a-cut Nd:YVO_4 crystal was used as the gain medium.

MgO:PPLNs of several millimeters long were used as frequency doublers. The input facet of the Nd:YVO_4 was AR coated at 808 nm and HR coated at both 1064 nm and 532 nm. The output facet of the Nd:YVO_4 and both facets of the MgO:PPLN were AR coated at both 1064 nm and 532 nm. The OC had a radius of curvature (ROC) of -50 mm and was HR coated at 1064 nm and AR coated at 532 nm. Material parameters of the 1% doped Nd:YVO_4 and MgO:PPLN used in the numerical simulation are listed in Table 5.1 while device structure parameters are in Table 5.2.

The generally calculated SHG power iterations with round trips of beam propagating in the cavity is shown in Fig. 5.2. Typically the iteration converges after several tens of round trips. Fig. 5.3 illustrates the calculated 2D beam profiles at the exit of the OC for the fundamental and SH waves, respectively.

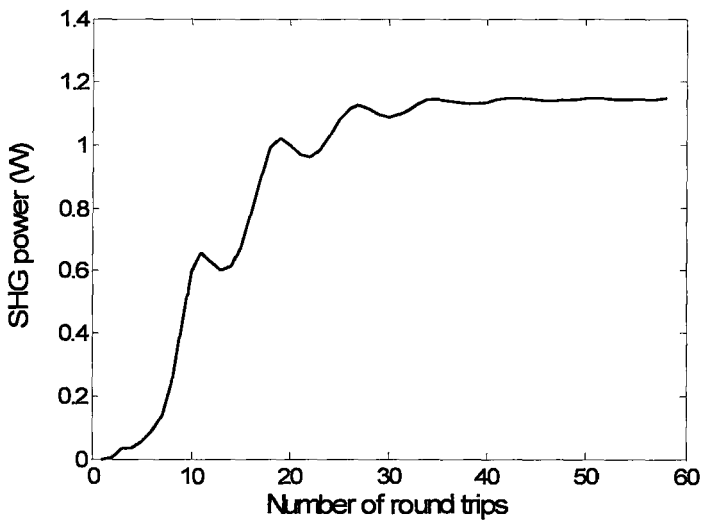

Fig. 5.2. Calculated SHG power with iteration round trips.

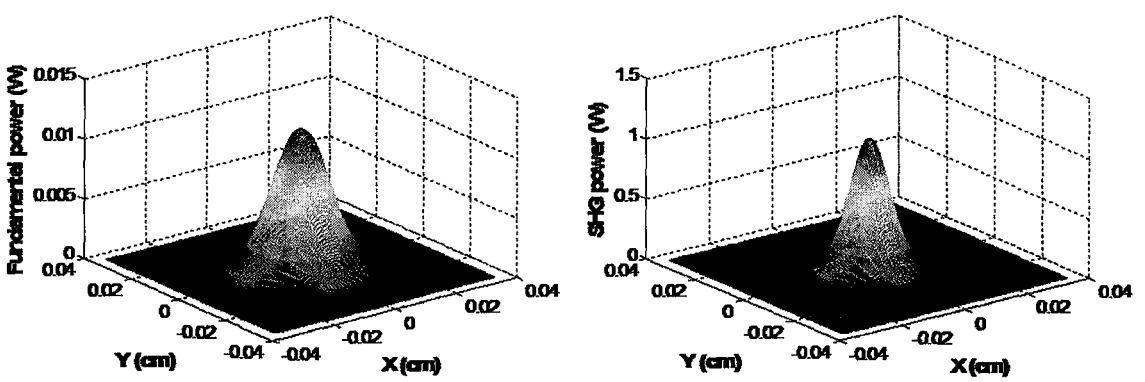

Fig. 5.3. Calculated typical 2D beam profiles for the fundamental and SH beams at the OC, respectively.

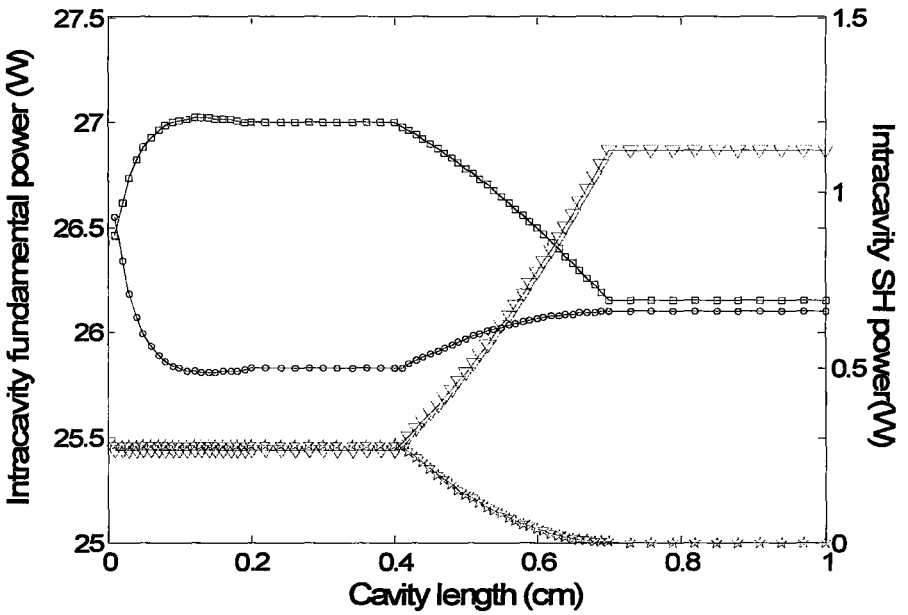

Fig. 5.4. Intra-cavity power distributions for forward and backward fundamental and SH waves. (Square: forward fundamental; circle: backward fundamental; triangle: forward SH; star: backward SH.)

5.4 Calculation Results and Model Validation

5.4.1 SHG Power with Pump Power

A typical power distribution in the cavity at a 2.8-W pump power is shown in Fig.5.4. The total cavity is 1-cm long, and the MgO:PPLN is 3 mm. It shows slightly non-uniform distributions (slight pump-depletion) for the forward and backward fundamental waves. Fig.5.5 shows the calculated green light power with the power of the 808-nm pump LD up to 2.8 W. The MgO:PPLN used was 2.38-mm-long. The experimental and analytical results are also plotted in the figure. The two calculated curves are in good agreement with the experimental curve. A slight deviation of the analytical model curve from the experimental curve at high power level is observed.

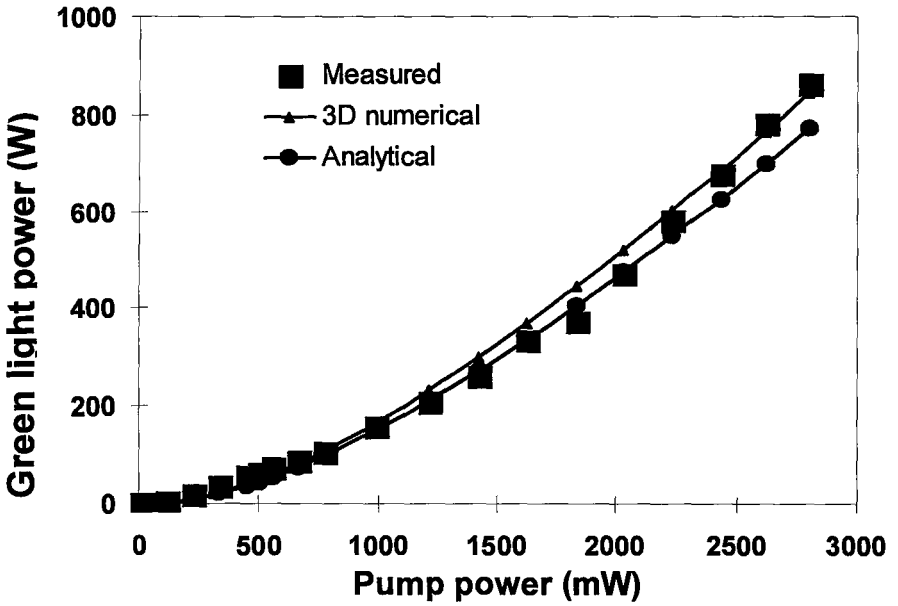

Fig. 5.5. Comparison of experimental phase matched pump-SHG curve with our numerical method and analytical results.

5.4.2 SHG Power Dependence on MgO:PPLN Length

The SHG powers with different MgO:PPLN lengths were also calculated by the numerical method, as shown in Fig. 5.6. The total cavity length is still kept at 1 cm. It is evident that the SHG power increases with the MgO:PPLN length and tends to saturate with longer MgO:PPLN.

In the experiments five MgO:PPLN crystals of 1.38-mm, 2.38-mm and 3.38-mm were used. Their maximum powers were achieved by fine adjusting the experimental setup (pump beam focusing, MgO:PPLN position, and OC alignment). The measured values are also marked as triangles in Fig. 5.6. During the experiment we kept the cavity geometric parameters constant, and only change different MgO:PPLN crystals. Thus only the material and fabrication parameters of MgO:PPLN crystals were variable from chip to chip during the

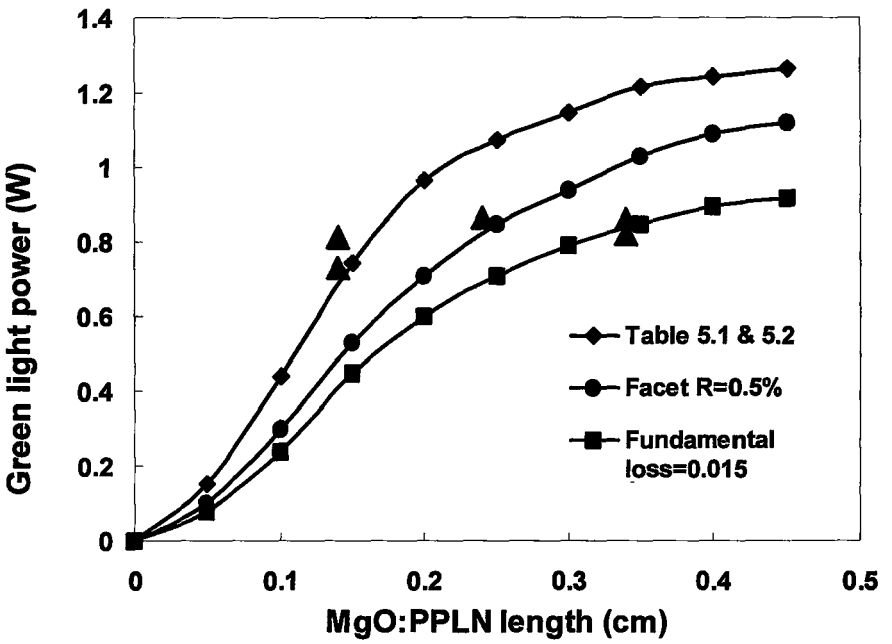

Fig. 5.6. MgO:PPLN length dependent on the green power, for three different parameters.

measurement and eventually associated with the measurement results. From the experimental results shown in Fig. 5.6, it is clear that the green light power does not change too much with varying crystal length, which is not predicted by the calculated curve (diamond) when all the device and geometric parameters are set according to Table 5.1 and Table 5.2. One possible explanation is that different MgO:PPLN crystals have slightly different AR coating quality, propagation loss, and effective nonlinear coefficient and these parameters may contribute to the discrepancy. To confirm this, we modified two of the parameters above in our numerical simulation. By changing the facet reflectivity from 0.15% to 0.5%, the second curve (dot) fit the measured value using the 2.38-mm-long crystal, while by further changing an additional fundamental loss coefficient from 0.01 cm^{-1} to 0.015cm^{-1}, the third curve (square) fits the measured values using the 3.38-mm crystal. The fact that our numerical calculation predicts the green light power quantitatively by adjusting parameters further reinforces the accuracy of our model.

5.4.3 Temperature Tuning Curves

Temperature tuning bandwidth of the device is a critical factor in applications requiring wider temperature tolerance. The temperature dependence of the extraordinary refractive index of the MgO:LN determines the phase mismatching factor. In the experiment the MgO:PPLN was hold by a copper

holder and was kept at fixed temperatures by the thermal electrical controller (TEC). Therefore it was assumed that the temperature of the MgO:PPLN crystal was set by the TEC. The temperature tuning curve was recorded by varying the TEC temperature. Fig. 5.7 shows measured temperature tuning curves for the 1.38-mm and 2.38-mm MgO:PPLN crystals. The calculated temperature tuning curve for the 1.38-mm MgO:PPLN crystal is also presented for comparison. The disagreement between the calculation and experimental results occurs at the first minimum points (13°C and 48°C) where the actual green light power near these regions is not zero (about 180 mW). One possible reason for the discrepancy can be attributed to the thermal effect in the MgO:PPLN crystal, as will be discussed in Section 5.6.

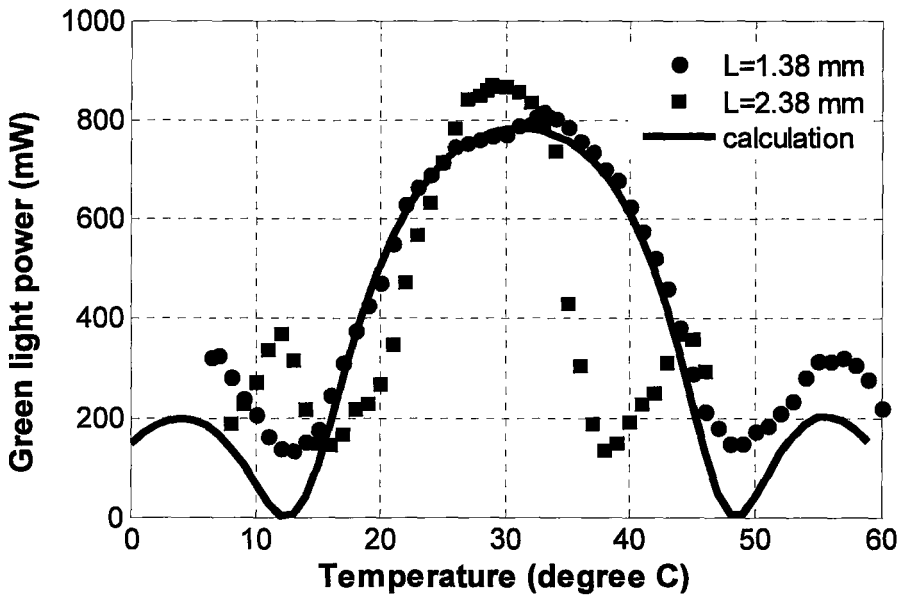

Fig. 5.7. Temperature tuning curves for the 1.38-mm and 2.38-mm MgO:PPLNs in the cavity. Solid line is the numerical simulation to fit the 1.38-mm MgO:PPLN. The QPM temperature is 30^0C.

5.5 Design of Cavity Parameters

This section presents numerical design of two key device parameters in intra-cavity frequency doubled DPSS lasers. In particular the SHG power with typical device geometric parameters is calculated, which would provide useful guidance to future experiments. For laser cavity design, when a cavity is fixed by its cavity length and ROC of the OC, the cavity mode is therefore unchanged. The

pump beam spot size is one characteristic of the pump laser beam quality and determined by the focusing lens. It has been widely recognized that the ratio of cavity mode to pump beam spot size has an effect on the laser threshold, slope efficiency, and expected output power [107]. In the simulation, we first calculate the fundamental power with different pump beam spot sizes, without the MgO:PPLN crystal. The pump power is 2.8 W, the cavity length is 1cm, ROC of the OC is -50 mm and reflectivity is 80%. Fig. 5.8 shows the variation of fundamental power with pump beam spot sizes, which is consistent with the published results [107] (without considering the thermal lensing effect). In Fig. 5.8 we also plot the variation of the SHG power as a function of the pump beam spot size when a 3-mm MgO:PPLN is inserted into the cavity. When the pump beam size is increased, the SHG power decreases. Fig. 5.9 shows the green light power versus cavity length. It is found that the SHG power decreases with the cavity length as a result of increasing cavity mode spot size. As the fundamental mode area increases with cavity length, the fundamental intensity in the

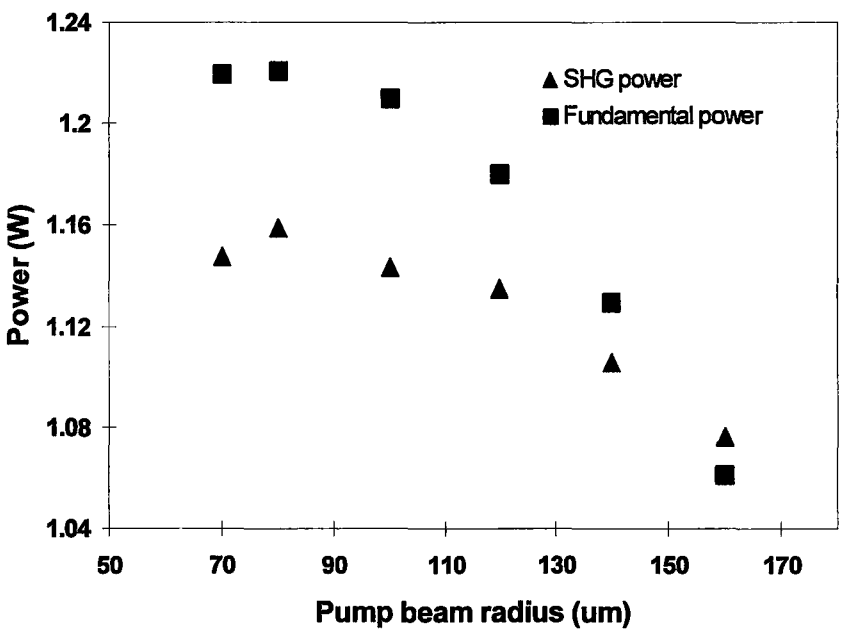

Fig. 5.8. Fundamental and green powers for different pump beam spot sizes.

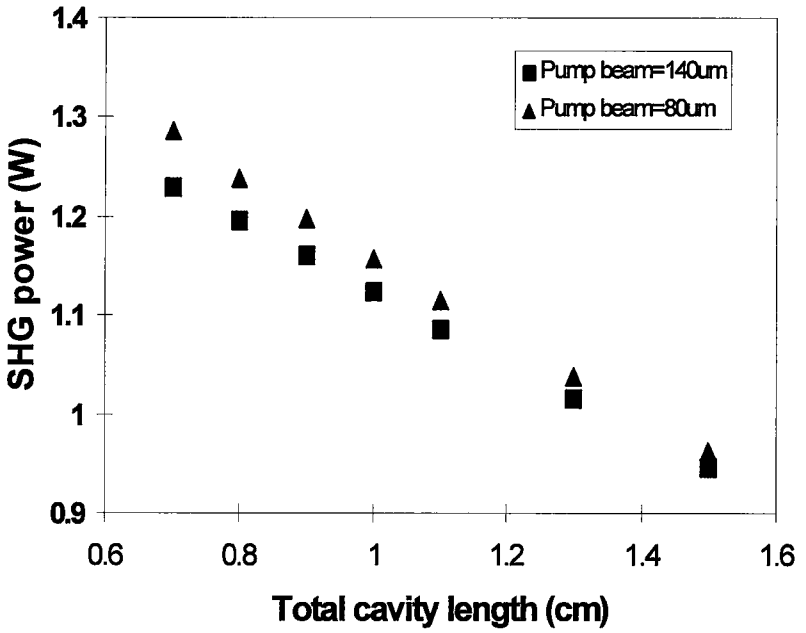

Fig. 5.9. Green light power with different cavity lengths, for two pump beam spot sizes.

nonlinear crystal is decreased. This results in the low conversion efficiency in the nonlinear crystal. We can also see from Fig. 5.9 that with a larger pump beam spot size the laser will generate less SHG power, which is consistent with Fig. 5.8. Here we can conclude that in an ideal cavity structure, there is a strong relationship between the SHG power, pump beam spot size and cavity length.

5.6 Thermal Effects

In intra-cavity frequency doubled DPSS lasers, the thermal property of nonlinear crystal is present in addition to that in the laser crystal (thermal lensing). Heat generated in nonlinear crystals can result in thermal de-phasing, due to the temperature dependent refractive index dispersion of nonlinear crystal materials.

In this section we further performed the numerical calculation of thermal de-phasing in intra-cavity frequency doubled DPSS lasers that include MgO:PPLN. The thermally induced refractive index for the MgO:PPLN crystal is investigated numerically to describe the temperature tuning characteristics. Furthermore, a 2D thermal equation is coupled with the 3D optical envelope field equations in the laser cavity through the thermal-optical effects of laser crystal and nonlinear

optical crystal, which gives a complete description of the coupled-wave propagation in the laser cavity.

5.6.1 Thermal Equations

According to the heat conduction theory [108], time dependent thermal conduction equation is

$$\rho_i C_i \frac{\partial T_i}{\partial t} = K_i \nabla^2 T_i + Q_i(r,z,t), \tag{5.12}$$

where ρ_i, C_i are the density and specific heat of the material, respectively. Thermal dynamics in the DPSS is expected to be slow as compared with the fast oscillating electric field, therefore the time-independent thermal equation can be included to account for thermal lensing and thermal de-phasing effects in the laser crystal and the nonlinear crystal, respectively. For the bulk Nd:YVO_4/MgO:PPLN green laser, if the transverse boundaries of the laser crystal and nonlinear crystal are held by a conductive metal such as Al or Cu with proper temperature T_0, we can assume a simple boundary condition $T|_{r=r0} = T_0$. The end facets of laser crystal and nonlinear crystal are both exposed to ambient temperature and it is assumed that they are isothermal. Therefore the heat flow is essentially radial (along transverse directions), and the thermal equation is described as a 2D thermal equation [108]

$$K_i \nabla_T^2 T_i + Q_i(x,y,z) = 0, \tag{5.13}$$

where K_i (in $W \cdot cm^{-1}K^{-1}$) and Q_i (in $W \cdot cm^{-3}$) are the heat conductance and generated heat density respectively. Heat generation in laser crystals is mainly due to the unabsorbed pump power, which reads [105] (in steady state):

$$Q_i(r,z) = \frac{2\alpha\eta_Q P_{in}}{\pi\omega_P^2(z)} \exp\left(-\frac{2r^2}{\omega_P^2(z)}\right) \exp(-\alpha z), \tag{5.14}$$

where $\eta_Q = 1 - \lambda_P / \lambda_L$ is the thermal conversion coefficient due to the quantum defect. In addition, heat generated in the nonlinear crystal is mainly due to linear absorption (α_1), nonlinear absorption (α_2), green induced infrared absorption (GIIRA) (α_{NL}), and two photon absorption (β) of the fundamental and SH waves by the nonlinear crystal [109]. The total heat generated in the MgO:PPLN is

$$Q_2(x,y,z) = \alpha_1 I_1 + \alpha_{NL} I_1 + \alpha_2 I_2 + \beta I_1^2 . \quad (5.15)$$

5.6.2. Modeling Thermal Effects in Nd:YVO$_4$ Lasers and Single-pass SHG in MgO:PPLN

In this section, we focus on the thermal effects in the laser crystal and nonlinear crystal respectively. Fig. 5.10 shows the Nd:YVO_4 lasing characteristics without the MgO:PPLN crystal, when the reflectivity of the OC is 80%. We can see from this figure that with the presence of thermal lensing, the extracted power gradually drops at higher pump powers. This is a well known result [105, 107]: if the pump beam is too small, the generated heat will result in serious thermal

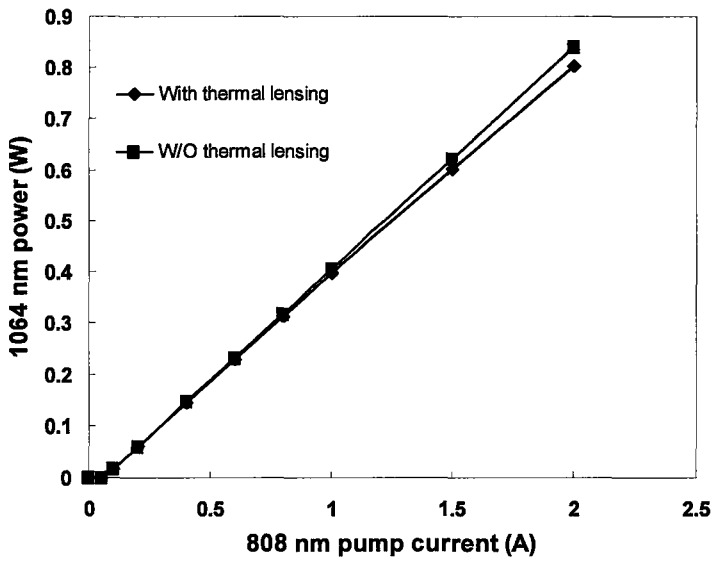

Fig. 5.10. Thermal lensing effect for the DPSS laser.

lensing and focusing of the laser beam in the cavity. The reduced optical volume has a negative effect on reducing light extraction efficiency from the laser cavity. As is shown in Fig. 5.11, with thermal lensing effect, the extracted power has an optimized pump beam spot size. In Fig. 5.11, the curve without thermal lensing from Fig. 5.8 is also presented for further comparison. In this simulation, due to the low pump power, thermal lensing effect is not significant and slight power degradation is observed.

Additionally we calculated the temperature tuning curves for single-pass SHG in the MgO:PPLN crystal. The input Gaussian beam is 1 W with the beam waist (60 μm) located in the center of the 1 cm long MgO:PPLN. Fig. 5.12 shows the calculated temperature tuning curves with different fundamental loss coefficients. It can be seen that the QPM temperature shifts towards low

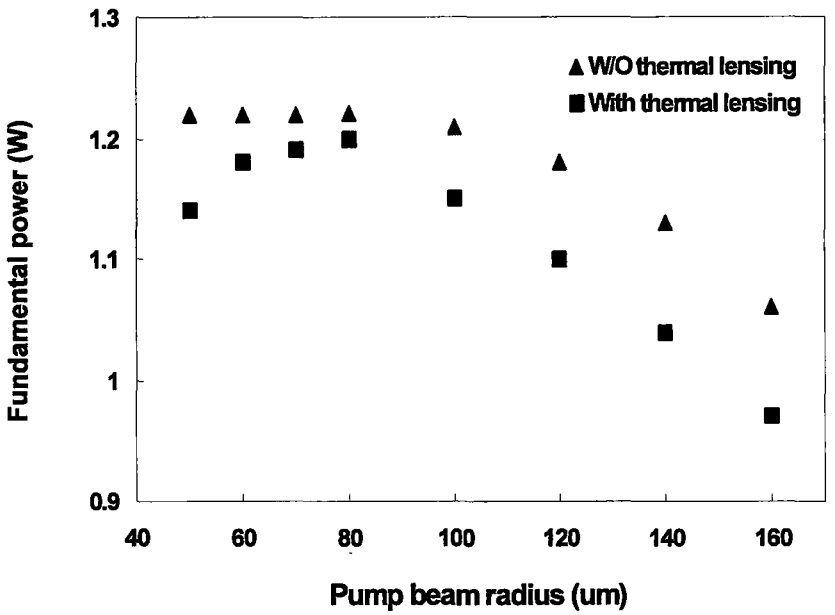

Fig. 5.11. Extracted power with pump beam radius for the Nd:YVO_4 laser, operated under fundamental mode.

temperature with the increasing loss coefficient, which indicate thermal de-phasing effect. This is true because higher absorption contributes to higher heat generation. The pumping region of the MgO:PPLN crystal, therefore, has higher temperature. An environmental temperature controller is needed to lower the crystal's central temperature down to the QPM temperature (30°C in this calculation). Another thermal de-phasing effect is clearly illustrated in Fig. 5.12. As the absorption coefficient increases, the first two zero points in the temperature tuning curve also increase and become non-zero. This phenomenon is also shown in the measured curves in Fig. 5.7. From Fig. 5.12 we may know that the thermal induced de-phasing in the MgO:PPLN accounts for the "lifting" of side lopes in the temperature tuning curve.

5.6.3 Modeling Bulk Nd:YVO_4/MgO:PPLN Green Lasers

Furthermore, we modeled bulk Nd:YVO_4/MgO:PPLN green lasers, by incorporating the thermal equations in both the laser and nonlinear crystal. All the parameters adopted are from Table 5.1 and 5.2 as well. Fig. 5.13 displays the

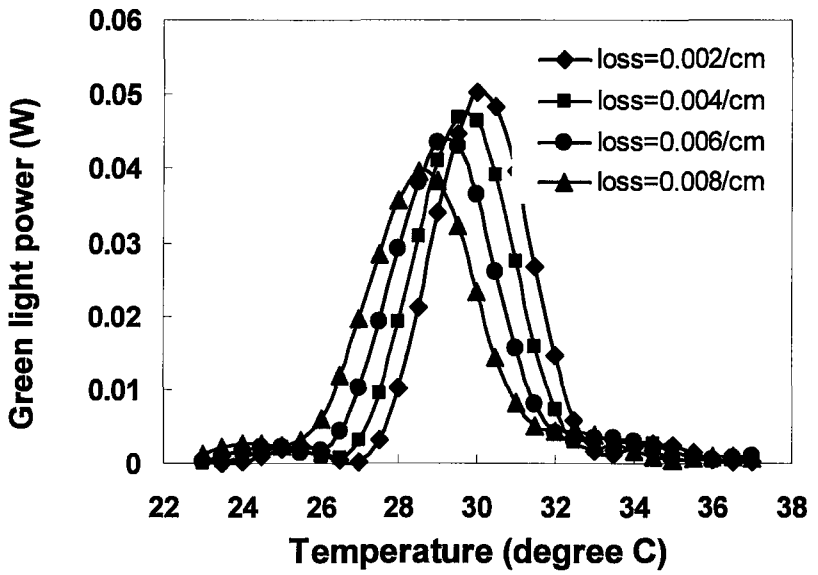

Fig. 5.12. Calculated temperature tuning curves for single-pass SHG, with different fundamental losses in the MgO:PPLN crystal.

green light power with and without considering the thermal lensing and de-phasing effects. It can be seen from these curves that the thermal de-phasing will influence the SHG process more than the thermal lensing to the laser itself. In the calculation we set the QPM temperature of the MgO:PPLN at 30°C. Without calculating the thermal lensing and de-phasing effects, the green light power is 1.15 W at the 2.8-W pump power. Considering the thermal effects and setting the environment temperature to be the QPM temperature (30°C), we find that at low pump power, due to less heat generation in the MgO:PPLN crystal, the green light power curve is approximately the same as that without the thermal effect, as shown in Fig. 5.13.

At high pump power levels, however, due to heat generation inside the MgO:PPLN, the crystal's central temperature is higher than that of the environment, i.e. deviating from the QPM temperature. This leads to the transition from the roughly quadratic dependence of the SH power on the pump power into

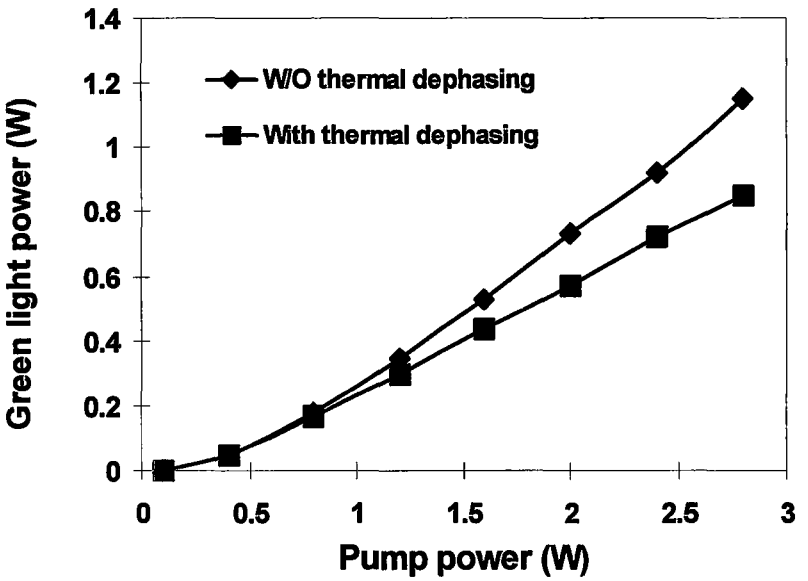

Fig. 5.13. Calculated green light power with pump power with and without thermal de-phasing in the MgO:PPLN, for the Nd:YVO_4/MgO:PPLN green laser.

the less efficient thermal de-phasing regime, where the generated SH power starts to deviate from the quadratic curve, and eventually becomes close to linear.

5.7 Summary

In this chapter, we have implemented a general 3D coupled-wave model to simulate intra-cavity frequency doubled DPSS lasers. Typical experimental results on the bulk Nd:YVO_4/MgO:PPLN green laser validate the numerical model. Besides, several other typical laser design parameters such as pump beam spot size and cavity length have been calculated to predict the power performance of intra-cavity frequency doubled DPSS lasers. As a versatile numerical model, it can be extended to model and design other intra-cavity nonlinear processes as well, such as intra-cavity optical parametric oscillators (IC-OPO).

In addition, thermal effects including thermal lensing and thermal de-phasing, present in the laser crystal and nonlinear crystal, have been modeled. The 3D numerical model that incorporates the 2D thermal equation has demonstrated deteriorated power performance caused by the thermal effects.

CHAPTER 6

CONCLUSION AND FUTURE WORK

6.1 Conclusion

In this thesis, the modeling and design of intra-cavity frequency doubled green lasers have been accomplished. Depending on the general TDTW model, governing equations for modeling DBR-LD/MgO:PPLN green lasers, optical contact Nd:YVO_4/MgO:PPLN green lasers and bulk Nd:YVO_4/MgO:PPLN green lasers have been derived respectively. Based on the implemented numerical models, new devices have been designed and new methods have been proposed to model different devices. The main conclusions are summarized as follows:

In chapter 3, the TDTW model is implemented to investigate a proposed intra-cavity frequency doubled green laser. The TDTW model has been validated by performances of the currently developed green lasers, which are based on single-pass FD of the MgO:PPLN waveguide with a high power DBR laser diode (single-pass frequency doubled DBR-LD/MgO:PPLN green lasers). With properly chosen device and material parameters based on the reported results, we find the TDTW is accurate enough for the modeling of FD process as well. The proposed new device, which is based on the IC-FD of a high power DBR laser diode with the MgO:PPLN waveguide (which is called intra-cavity frequency doubled DBR-LD/MgO:PPLN green lasers), is modeled and designed. Compared with the reported single-pass frequency doubled DBR-LD/MgO:PPLN green laser, the new device has demonstrated superiority in the generation of 530 nm green light. We have found by the numerical design that the intra-cavity frequency doubled semiconductor green laser may generate the same power (250 mW) with a half MgO:PPLN waveguide length (6 mm) at 700 mA pump current, as compared with the reported results. Furthermore, we also found that the temperature tolerance is larger than the single-pass FD device. Most importantly, the semiconductor laser-to-waveguide coupling tolerance is much larger than the single-pass FD device. High speed modulation with injection current at 100 MHz has also been modeled to show the equal modulation capability of this intra-cavity frequency doubled devices. At last, we found theoretically that further fabrication cost reduction is possible by designing a bulk green laser. The proposed device is

composed of a DBR laser and a bulk MgO:PPLN crystal. With enhancement of the SH wave in the cavity by increasing the facet reflectivity of the MgO:PPLN right facet > 85%, green light power more than 200 mW at 700 mA pump current can be extracted.

In chapter 4, we have modeled miniature optical contact Nd:YVO_4/MgO:PPLN green lasers. The plane-wave based coupled-wave model has been validated by comparison with the experiments performed on the optical contact Nd:YVO_4/MgO:PPLN green lasers. In addition, we have studied the phase problem in the intra-cavity frequency doubled DPSS lasers, by numerically investigating the temperature tuning curves of the single MgO:PPLN chips and the optical contact Nd:YVO_4/MgO:PPLN green lasers respectively. The numerical results agree with the experiments fairly well when phase difference between the SH waves are considered, which further verifies our model. Several examples have been presented for the design of wide temperature operated Nd:YVO_4/MgO:PPLN green lasers based on the numerical model. Multiple-section MgO:PPLN gratings and chirped MgO:PPLN gratings have been calculated in the Nd:YVO_4 laser cavity, demonstrating the flexible application of our plane-wave model.

In chapter 5, in order to characterize the high power bulk intra-cavity frequency doubled solid-state green laser, a 3D coupled-wave model has been implemented. Experimental results on the bulk Nd:YVO_4/MgO:PPLN green laser validated the numerical model. Besides, several other typical laser design parameters have been calculated to predict the intra-cavity frequency doubled Nd:YVO_4/MgO:PPLN green lasers. Furthermore thermal problems, present in both laser crystal and nonlinear crystal in the intra-cavity frequency doubled Nd:YVO_4/MgO:PPLN green laser, have been modeled. The 3D numerical model that incorporates the 2D thermal equation has demonstrated the deteriorated power performance caused by the thermal effects, and suggested the necessity of thermal management in intra-cavity frequency doubled DPSS lasers.

6.2 Future Work

Based on the implemented numerical models, which have been successfully employed in the simulation of typical intra-cavity frequency doubled green lasers, further work still needs to be explored.

(1) Employ the TDTW model to simulate more complex semiconductor IC-FD device.

As reviewed in Chapter 1, a vertical extended cavity surface emitting laser (VECSEL) or semiconductor disk laser has been demonstrated to generate efficient visible light in recent years. Fast carrier lifetime facilitates the device operated under modulation mode. Therefore, the TDTW model can be easily extended to model and design the intra-cavity frequency doubled VECSEL. Alternatively, the full TDTW model in 3D can also be used to understand the dynamic behaviors of the intra-cavity frequency doubled VECSEL.

(2) Device optimization and design with the complete 3D model.

In Chapter 5, we incorporate a 2D thermal equation into the 3D model. We have calculated the basic thermal lensing and thermal de-phasing effects in intra-cavity frequency doubled DPSS lasers. A further modeling of the thermal de-phasing properties in this laser and further thermal management is beneficial through the complete numerical model.

(3) Design of new QPM structures for the IC-SHG of DPSS lasers.

Advanced QPM gratings, such as aperiodical QPM (AQPM) gratings, can be introduced into both the plane-wave and 3D numerical model to predict their performances. Experimental work on the intra-cavity frequency doubled Nd:YVO_4 laser with specially designed AQPM MgO:PPLN grating has been demonstrated, however, device optimization design has not been done so far. Both plane-wave coupled model and 3D model can be utilized to design this device.

(4) Experimental work

From an experiment point of view, this thesis does not focus much on the experimental work. Experimental results obtained from the published papers in Chapter 3 and by our own in Chapter 4 and Chapter 5 are used to validate the numerical models. There is certainly more work to do, in particular, experimental demonstration of the intra-cavity frequency doubled DBR-LD/MgO:PPLN green lasers in Chapter 3.

References

1. T. H. Maiman, "Stimulated optical radiation in Ruby," *Nature*, vol.187, no.4736, pp. 493-494, 1960.
2. W.P. Risk, T. R.Gosnell, and A. V. Nurmikko, "Compact blue-green lasers," Cambridge University Press, 2003.
3. D. Graham-Rowe, "Projectors get personal,", *Nature Photonics,* vol. 1, pp. 677-679, 2007.
4. H. Moench, "New markets and new light-sources for projection," *Proc. SPIE*, Vol.6911, 69110Y, 2008.
5. Yole Development, "Green laser market for projection devices," http://www.i-micronews.com/upload/Rapports/Green_Laser_Market_for_Projection_Devices.pdf.
6. M. Ikeda, Y. Mori, H. Sato, K. Kaneko, and N. Watanabe, "Room temperature continuous wave operation of an AlGaInP double heterostructure laser grown by atmospheric pressure metal–organic chemical vapor deposition," *Appl. Phys. Lett.*, vol. 47, no. 10, pp. 1027–1028, Nov. 1985.
7. B. Qiu, O.P. Kowalski, S. McDougall, B. Schmidt, and J.H. Marsh, "High-Performance Visible Semiconductor Lasers Operating at 630 nm," *IEEE Photonics Journal*, vol.2, no.4, pp.563-570, Aug. 2010.
8. S. Nakamura, M. Senoh, S. Nagahama, N. Iwasa, T. Yamada, T. Matsushita, H. Kiyoku and Y. Sugimoto, "InGaN-Based Multi-Quantum-Well-Structure Laser Diodes," *Jpn. J. Appl. Phys.*, vol. 35, L74-L76, 1996.
9. R. N. Hall, G. E. Fenner, J. D. Kingsley, T. J. Soltys, and R. O. Carlson, "Coherent Light Emission From GaAs Junctions," *Phys. Rev. Lett.,* vol. 9, pp. 366–368, 1962.
10. Marshall I. Nathan, William P. Dumke, Gerald Burns, Frederick H. Dill, and Gordon Lasher, "Stimulated Emission of Radiation from GaAs p-n Junctions," *Appl. Phys. Lett.*, vol.1, pp. 62-64, 1962.
11. S. Nakamura, N. Iwasa, M. Senoh and T. Mukai, "Hole Compensation Mechanism of P-Type GaN Films," *Jpn. J. Appl. Phys,* vol. 31, pp. 1258-1266, 1992.
12. Y.-D. Lin, M. T. Hardy, P. S. Hsu, K. M. Kelchner, C.-Y. Huang, D. A. Haeger, R. M. Farrell, K. Fujito, A. Chakraborty, H. Ohta, J. S. Speck, S. P.

DenBaars and S. Nakamura, "Blue-Green InGaN/GaN Laser Diodes on Miscut *m*-Plane GaN Substrate," *Appl. Phys. Exp.*, vol. 2, pp. 082102, 2009.

13. Y. Enya, Y. Yoshizumi, T. Kyono, K. Akita, M. Ueno, M. Adachi, T. Sumitomo, S. Tokuyama, T. Ikegami, K. Katayama, and T. Nakamura, "531nm green lasing of InGaN based laser diodes on semi-polar {2021} free-standing GaN substrates," *Appl. Phys. Exp.*, vol. 2, no. 8, pp. 082101, Aug. 2009.
14. A. Avramescu, T. Lermer, J. Müller, S. Tautz, D. Queren, S. Lutgen, and U. Strauß, "InGaN laser diodes with 50 mW output power emitting at 515 nm," *Appl. Phys. Lett.*, vol. 95, no. 7, pp. 071103, Aug. 2009.
15. T. Miyoshi, S. Masui, T. Okada, T. Yanamoto, T. Kozaki, S. Nagahama, T.Mukai, "InGaN-based 518 and 488 nm laser diodes on *c*-plane GaN substrate," *Physica Status Solidi (a)*, vol. 207, no. 6, pp. 1389–1392, June 2010.
16. T. Miyoshi, T. Kozaki, T. Yanamoto, S. Nagahama, T. Mukai, "GaN-based 1-W continuous-wave blue-laser diodes," *SID 2008 Digest*, 63.3, pp.966-968, 2008.
17. P.A. Franken A. E. Hill, C. W. Peters, and G. Weinreich, "Generation of optical harmonics," *Phys. Rev. Lett.*, vol.7, p. 118 Aug. 1961.
18. J. E. Geusie, H. J. Levenstein, S. Sigh, R.G. Smith, and L. G. Van Uitert, "Continuous 0.532-μ solid-state source using $Ba_2NaNb_5O_{15}$," *Appl. Phys. Lett.*, vol.12 no.9, pp.306-309, 1968.
19. R. G. Smith, "Theory of intracavity optical second harmonic generation," *IEEE J. Quantum Electron.*, vol.6, no.4, pp. 215-130, Apr. 1970.
20. Y. Q. Zheng, H. Y. Zhu, L. X. Huang, H. B. Chen, Y. M. Duan, R. B. Su, C. H. Huang, Y. Wei, J. Zhuang, and G. Zhang, "Efficient 532 nm laser using high gray-tracking resistance KTP crystal," *Laser Physics*, vol. 20, no. 4, pp. 756-760, 2010.
21. N. Pavel, T. Taira, Y. Tamaoki, and H. Kan, " Continuous-wave high-power intracavity frequency-doubled Nd:GdVO4-LBO green laser," in *Nonlinear Optics: Materials, Fundamentals and Applications*, Technical Digest (CD) (Optical Society of America, 2004), paper WD6.
22. Y. Hirano, T. Sasagawa, T. Yanagisawa, S.Yamamoto, A. Nakamura, T. Yagi, and H. Sugiura, "Solid-state SHG green laser for laser TV," *CLEO/QELS*, 1-2, 2009.
23. M. Zhou, B. X. Yan, G. Bao, Y. Zhang, C. Gawith, D. D. Wang, Y. Qi, and Y. Bi, "52% optical-to-optical conversion efficiency in a compact 1.5 W 532 nm second harmonic generation laser with intracavity periodically-poled MgO:$LiNbO_3$," *Laser Physics*, vol. 20, no. 7, pp. 1568-1571, 2010.

24. Y. Qi, B. Yan, S. Chu, Y. Wang, T. Fang, Y. Bi, W. Yan, H. Min, and Y. Liu, "High Power green laser with PPMgLN intracavity doubled," in *CLEO Pacific Rim* (2009).
25. T. Yokoyama, K. Mizuuchi, K. Nakayama, A. Kurozuka, T. Sugita, A. Morikawa, and K. Yamamoto, "Compact intracavity green light source with wide operation temperature range using periodically poled Mg:$LiNbO_3$," *Jan. J. Appl. Phys.*, vol. 47, no. 8, pp. 6787-6789, Aug. 2008.
26. V. G. Dmitriev, G. G. Gurzadyan, and D. N. Nikogosyan, "Handbook of Nonlinear optical crystals," 3rd Rev. Ed., Springer Series in Optical Sciences, Vol. 64, 1999
27. A.Jechow, R. Menzel, K. Paschke, and G. Erbert, "Blue-green light generation using high brilliance edge emitting diode lasers," *Laser Photon. Rev.*, vol. 4, no. 5, pp. 633–655, 2010.
28. O. B. Jensen, P. E. Andersen, B. Sumpf, K.-H. Hasler, G. Erbert, and P. M. Petersen, "1.5 W green light generation by single-pass second harmonic generation of a single-frequency tapered diode laser," *Opt. Expr.*, vol. 17, no.8, pp. 6532–6539, Apr. 2009.
29. C. Fiebig, G. Blume, M. Uebernickel, D. Feise, C. Kaspari, K. Paschke, J. Fricke, H. Wenzel, and G. Erbert, "High-power DBR-tapered laser at 980 nm for single-path second harmonic generation," *IEEE J. Sel. Top. Quantum Electron.*, vol. 15, no. 3, pp. 978–983, May-June 2009.
30. M. H. Hu, H. K. Nguyen, K. Song, Y. Li, N. J. Visovsky, X. Liu, N. Nishiyama, S. Coleman, L. C. Hughes, J. Gollier, W. Miller, R. Bhat, and C.-E. Zah, "High-power high-modulation-speed 1060-nm DBR lasers for green-light emission," *IEEE Photon. Technol. Lett.*, vol. 18, no. 4, pp. 616–618, Feb. 2006.
31. H. K. Nguyen, M. H. Hu, N. Nishiyama, N. J. Visovsky, Y. Li, K. Song, X. Liu, J. Gollier, L. C. Hughes, R. Bhat, and C.-E. Zah, "107-mW low-noise green-light emission by frequency doubling of a reliable 1060-nm DFB semiconductor laser diode," *IEEE Photon. Technol. Lett.*, vol. 18, no. 5, pp. 682–684, Mar. 2006.
32. C.-E. Zah, Y. Li, R. Bhat, K. Song, N. visovsky, H. K. Nguyen, X. Liu, M. Hu, and N. Nishiyama, "High power 1060-nm raised-ridge strained single-quantum-well lasers," in *IEEE Int. Semiconductor Laser Conf.*, Matsue, Japan, ThA3, pp. 39–40, Sep. 2004.
33. H. K. Nguyen, M. H. Hu, Y. Li, K. Song, N. J. Visovsky, S. Coleman, and C.-E. Zah, "304 mW green light emission by frequency doubling of a high-power 1060-nm DBR semiconductor laser diode," in *Proc. SPIE*, vol. 6890, pp. 6890I, 2008.

34. M. H. Hu, H. K. Nguyen, K. Song, Y. Li, N. J. Visovsky, X. Liu, N. Nishiyama, S. Coleman, L. C. Hughes, J. Gollier, W. Miller, R. Bhat, and C.-E. Zah, "High-power distributed Bragg reflector lasers for green-light generation," in *Proc. SPIE*, vol. 6116, pp. 61160M, 2006.
35. M. Kuznetsov; F. Hakimi; R. Sprague; A. Mooradian; , "High-power (>0.5-W CW) diode-pumped vertical-external-cavity surface-emitting semiconductor lasers with circular TEM_{00} beams," *IEEE Photon. Technol. Lett.*, vol.9, no.8, pp.1063-1065, Aug. 1997.
36. M. Kuznetsov, F. Hakimi, R. Sprague, A. Mooradian, "Design and characteristics of high-power (>0.5-W CW) diode-pumped vertical-external-cavity surface-emitting semiconductor lasers with circular TEM_{00} beams," *IEEE Selected Top. in Quantum Electron.*, vol.5, no.3, pp.561-573, May/Jun 1999.
37. L.E. Hunziker, C. Ihli, D.S. Steingrube, "Miniaturization and Power Scaling of Fundamental Mode Optically Pumped Semiconductor Lasers," *IEEE Selected Top. in Quantum Electron.*, vol.13, no.3, pp.610-618, May-June 2007.
38. J. Lee , S. Lee , T. Kim and Y. Park "7 W high-efficiency continuous-wave green light generation by intracavity frequency doubling of an end-pumped vertical external-cavity surface emitting semiconductor laser", *Appl. Phys. Lett.*, vol. 89, pp. 241107 2006.
39. M. Fallahi, F. Li Y. Kaneda, C. Hessenius, J. Hader, Li H. J.V. Moloney, B. Kunert, W. Stolz, S.W. Koch, J. Murray, and R. Bedford, "5-W yellow laser by intracavity frequency doubling of high-power vertical-external-cavity surface-emitting laser," *IEEE Photon. Technol. Lett.*, vol.20, no.20, pp.1700-1702, Oct.15, 2008.
40. E. U. Rafailov, W. Sibbett, A. Mooradian, J. G. McInerney, H. Karlsson, S. Wang, and F. Laurell, "Efficient frequency doubling of a vertical-extended-cavity surface-emitting laser diode by use of a periodically poled KTP crystal," *Opt. Lett.*, vol.28, no.21, pp. 2091-2093, 2003.
41. M. Jansen, S. Brittain, G. Giaretta, J. Green, G. Niven, C. Stuart, and W. Wu, "Large venue laser-based projectors," *SID 2007*, vol. 4, pp. 1879-1882, 2007.
42. F. Laurell, "Stable blue second-harmonic generation in a KTP waveguide with a diode laser in an external cavity," *Electron. Lett.*, vol.29, no.18, pp.1629-1630, Sept. 1993.
43. J. Zimmermann, Jens Struckmeier, Martin R. Hofmann, and Jan-Peter Meyn, "Tunable blue laser based on intracavity frequency doubling with a fan-structured periodically poled $LiTaO_3$ crystal," *Opt. Lett.*, vol. 27, no.8, pp. 604-606, 2002.
44. K. Li, A. Yao, N. J. Copner, C. B. E. Gawith, I. G. Knight, H.-U. Pfeiffer, and B. Musk, "Compact 1.3 W green laser by intracavity frequency doubling of a

multi-edge-emitter laser bar using a MgO: PPLN crystal," *Opt. Lett.*, vol. 34, no. 22, pp. 3472–3474, Nov. 2009.

45. T. Suhara and M. Fujimura, "Waveguide Nonlinear-Optic Devices," Springer, Berlin, Germany, 2003.
46. N. Iyi, K. Kitamura, F. Izymi, K. Kimura, J.K.Yamamoto, *J. Solid State Chem.* vol.101, p.340, 1992.
47. D. A. Bryan, R. Gerson, and H. E. Tomaschke, "Increased optical damage resistance in lithium niobate," *Appl. Phys. Lett.*, vol. 44, no. 9, pp. 847–849, 1984.
48. Y. Furukawa, K. Kitamura, E.Suzuki, K.Niwa, "Stoichiometric LiTaO3 single crystal growth by double crucible Czochralski method using automatic powder supply system," *J. Crystal Growth*, vol.197, pp.889-895,1999.
49. K. Kawano and T. Kitoh, "Introduction to optical waveguide analysis: solving Maxwell's equations and the Schrodinger equation," John Wiley & Sons, 2001.
50. RSoft Photonic Component Design Suite, RSoft Design Group, Inc., http://www.rsoftdesign.com/products.php?sub=Component+Design
51. Optiwave Component Design, Optiwave Systems Inc., http://www.optiwave.com/products/index.html
52. Apollo APSS, Apollo Inc., http://www.apollophoton.com/apollo/page.php?id=10
53. Apollo ALDS, Apollo Inc., http://www.apollophoton.com/apollo/page.php?id=9
54. X. Li, "Optoelectronic devices: design, modeling, and simulation," Cambridge University Press, 2009, ch. 1.
55. W. Streifer, D. R. Scifres, and A. D. Burnham, "Coupled wave analysis of DFB and DBR lasers," *IEEE J. Quantum Electron.*, vol. 13, no. 4, pt.2, pp. 134-41, April 1977.
56. A. Yariv, "Optical electronics in modern communications," 5 Edition, chapter 8, Oxford University Press, USA, 2006.
57. L. M. Zhang, S. F. Yu, M. C. Nowell, D. D. Marcenac, J. E. Carroll, and R. G. S. Plumb, "Dynamic analysis of radiation and side-mode suppression in a second-order DFB laser using time-domain large-signal traveling wave model," *IEEE J. Quantum Electron.*, vol. 30, pp. 1389-1395, Jun. 1994.
58. Q.-Y. Xu, X. Li, C.-Q. Xu, and W.-P. Huang, "Modulation crosstalk and reduction in distributed feedback laser diode and monitor photodiode monolithically integrated optical transceivers," *IEEE J. Quantum Electron.*, vol. 46, no. 3, pp. 323–331, Mar. 2010.

59. Yu, S.F., "Improved time-domain traveling-wave model for vertical-cavity surface-emitting lasers," *IEEE J. Quantum Electron.*, vol. 34, no. 10, pp. 1938-1948, Oct 1998.
60. B. S. Kim, Y. Chung, and J. S. Lee, "An efficient split-step time-domain dynamic modeling of DFB/DBR laser diodes," *IEEE J. Quantum Electron.*, vol. 36, pp. 787-794, July 2000.
61. J. Park, X. Li, and W.-P. Huang, "Performance simulation and design optimization of gain–clamped semiconductor optical amplifiers based on distributed Bragg reflectors," *IEEE J. Quantum Electron.*, vol. 39, pp. 1415-1423, Nov. 2003.
62. A. G. Fox and T. Li, "Computation of optical resonator modes by the method of resonance excitation", *IEEE J. Quantum Electron.*, vol. QE-4, pp. 460, 1968.
63. M. Hodgon and H. Weber, "Laser resonators and beam propagation: fundamentals, advanced concepts and applications," Second Ed., Springer Science+Business Media, Inc., 2005, ch. 16, pp. 549.
64. E. A. Sziklas and A. E. Siegman, "Mode calculations in unstable resonators with flowing saturation gain. 2: fast Fourier transform method," *Appl. Opt.*, vol. 14, no. 8, pp. 1874-1889, Aug. 1975.
65. H. Shu and M. Bass, "Three-dimensional computer model for simulating realistic solid-state lasers," *Appl. Opt.*, vol. 46, no. 23, pp. 5687-5697, Aug. 2007.
66. G. R. Hadley, A. Owyoung, P. Esherick, and J. P. Hohimer, "Numerical simulation and experimental studies of longitudinally excited miniature solid-state lasers," *Appl. Opt.*, vol. 27, no. 5, pp. 819-827, Mar. 1988.
67. LASCAD, LAS-CAD GmbH, http://www.las-cad.com/index.php
68. G. Li, S. Zhao, K. Yang, and J. Zou, "Laser-diode end-pumped passively Q-switched intracavity-frequency-doubling Nd:$GdVO_4$/KTP green laser with GaAs saturable absorber," *IEEE J. Sel. Top. Quantum Electron.*, vol.11, no.3, pp. 638-643, May/Jun. 2005.
69. R. W. Boyd "Nonlinear optics," 3rd Edition, Academic Press, 2008.
70. Y. R. Shen, "The principles of nonlinear optics," John Wiley & Sons, 1984.
71. O. Gayer, Z. Sacks, E. Galun, and A. Arie, "Temperature and wavelength dependent refractive index equations for MgO-doped congruent and stoichiometric $LiNbO_3$," *Appl. Phys. B*, vol. 91, no. 2, pp. 343–348, May 2008.
72. H. Ito, C. Takyu, and H. Inaba, "Fabrication of periodic domain grating in LiNbO3 by electron beam writing for application of nonlinear optical processes," *Electron. Lett.*, vol. 27, pp. 1221–1222, 1991.
73. A. Harada and Y. Nihei, "Bulk periodically poled MgO-LiNbO3 by corona discharge method," *Appl. Phys. Lett.*, vol. 69, no. 18, pp. 2629–2631, 1996.

74. M. Yamada, N. Nada, M. Saitoh, and K. Watanabe, "First-order quasi-phase matched LiNbO3 waveguide periodically poled by applying an external field for efficient blue second-harmonic generation," *Appl. Phys. Lett.*, vol. 62, no. 5, pp. 435–436, 1993.
75. K. Nakamura, J. Kurz, K. Parameswaran, and M. M. Fejer, "Periodic poling of magnesium-oxide-doped lithium niobate," *J. Appl. Phys.*, vol. 91, no. 7, pp. 4528–4534, 2002.
76. K. Kintaka, M. Fujimura, T. Suhara, and H. Nishihara, "High-efficiency LiNbO3 waveguide second-harmonic generation devices with ferroelectric-domain-inverted gratings fabricated by applying voltage," *J. Lightwave Technol.*, vol. 14, no. 3, pp. 462–468, 1996.
77. Yang Lu, Qingyang Xu, Yi Gan, and Changqing Xu, "Field-Sequential Operation of Laser Diode Pumped Nd :YVO4/PPMgLN Microchip Green Laser," *IEEE Photon. Technol. Lett.*, vol. 22, no. 13, pp.990-992, July 2010.
78. J. Khaydarov, A. Shchegrov, S. Essaian, G. Nemet, S. Soghomonyan, M. Simonyan, H. Danielyan, and G. Gabrielyan, "High-efficiency green laser source for compact projectors," in *Proc. SID*, San Antonio, June 2 - 5, paper 20.2 (2009).
79. U. Steegmuller, M. Kuhnelt, H. Unold, T. Schwarz, R. Schulz, K. Auen, C. Walter, and M. Schmitt, "Visible lasers for mobile projection," in *Proc. SPIE*, vol. 7001, pp. 70010D, 2008.
80. K. Ito, K. Kawamoto, and H. Momiji, "Theoretical study on intra-cavity distributed-Bragg-reflection quasi-phase-matched second-harmonic lasers," *Opt. Rev.*, vol. 2 no. 5, pp. 371–376, Sept. 1995.
81. Q.-Y. Xu, Y. Gan, Y. Lu, X. Li and C.-Q. Xu, "Theoretical analysis of intra-cavity second-harmonic generation of semiconductor lasers by a periodically poled nonlinear crystal waveguide," Accepted by *IEEE J. Quantum Electron.*
82. M. Iwai, T. Yoshino, S. Yamaguchi, M. Imaeda, N. Pavel, I. Shoji, and T. Taira, "High-power blue generation from a periodically poled MgO:$LiNbO_3$ ridge-type waveguide by frequency doubling of a diode end-pumped Nd:$Y_3Al_5O_{12}$ laser," *Appl. Phys. Lett.*, vol. 83, no.18, pp. 3659–3661, Nov. 2003
83. Y. Furukawa, K. Kitamura, A. Alexandrovski, R. K. Route, M. M. Fejer, and G. Foulon, "Green-induced infrared absorption in MgO doped LiNbO3," *Appl. Phys. Lett.*, vol. 78, no. 14, pp. 1970–1972, Apr. 2001.
84. K. Sakai, Y. Koyata, and Y. Hirano, "Planar-waveguide quasi-phase-matched second-harmonic-generation device in Y-cut MgO-doped LiNbO3," *Opt. Lett.*, vol. 31, no. 21, pp. 3134–3136, Nov. 2006.

85. 25. D. Botez, "Design considerations and analytical approximations for high continuous-wave power, broad-waveguide diode lasers," *Appl. Phys. Lett.*, vol. 74, no. 21, pp. 3102–3104, May 1999.
86. G. Yang, G. M. Smith, M. K. Davis, A. Kussmaul, D. A. S. Loeber, M. H. Hu, H.-K. Nguyen, C.-E. Zah, and R. Bhat, "High-performance 980-nm ridge waveguide lasers with a nearly circular beam," *IEEE Photon. Technol. Lett.*, vol.16, no.4, pp. 981–983, Apr. 2004.
87. D. Botez, "Simple design rules for single-lobe operation of (evanescently coupled) index-guided phase-locked arrays of diode lasers," *IEEE J. Quantum Electron.*, vol.24, no.10, pp. 2034–2038, Oct. 1988.
88. A. Al-Muhanna, L. J. Mawst, D. Botez, D. Z. Garbuzov, R. U. Martinelli, and J. C. Connolly, "High-power (>10W) continuous-wave operation from 100- μ m-aperture 0.97- μ m-emitting Al-free diode lasers," *Appl. Phys. Lett.*, vol. 73, no. 9, pp. 1182–1184, Aug. 1998.
89. G. W. Yang, J. Y. Xu, Z. T. Xu, J. M. Zhang, L. H. Chen, and Q. M. Wang, "Theoretical investigation on quantum well lasers with extremely low vertical beam divergence and low threshold current," *J. Appl. Phys.*, vol. 83, no. 1, pp. 9–14, Jan. 1998.
90. M. Yuda, T. Sasaki, J. Temmyo, M. Sugo, and C. Amano, "High-power highly reliable 1.02-1.06-μm InGaAs strained-quantum-well laser diodes," *IEEE J. Quantum Electron.*, vol. 39, no. 12, pp. 1515–1520, Dec. 2003.
91. Y. Lu, Q. Xu, Y. Gan, C. Xu, "Compact High Power Modulated Green Laser for Laser Display," *SID 2010*, pp.1170-1172.
92. Y. Lu, Q. Xu, Y. Gan, C.Xu, "Over 500 mW Laser-Diode Pumped Green Laser Using Optical Contact Nd:YVO_4/Periodically Poled MgO:$LiNbO_3$ Crystal, *OSA / CLEO/QELS* 2010, JTuD110.pdf.
93. T. Harimoto and J. Watanabe, "Efficient and stable 532 nm microchip laser pumped by single-longitudinal-mode laser-diode," *Electron. Lett.*, vol.41, no.12, pp.702-704. June 2005.
94. C. Jung, B.-A. Yu, I.-S. Kim, Y. L. Lee, N. E. Yu, and D.-K. Ko, "A linearly-polarized Nd:YVO_4/KTP microchip green laser," *Opt. Exp.*, vol. 17, no.12, pp. 19611-19616, 2009.
95. C. Jung, B.-A. Yu, K. Lee, Y. L. Lee, N. E. Yu, D.-K. Ko, and J. Lee, "A compact diode-pumped microchip green light source with a built-in thermoelectric element," *Appl. Phys. Exp.*, vol. 1, pp. 062005, 2008.
96. B.-A. Yu, C. Jung, I.-S. Kim, Y. L. Lee, N. E. Yu, and D.-K. Ko, "Temperature-controlled efficient microchip green laser for mobile projection displays," *Electron. Lett.*, vol. 45, no. 18, pp.943–945, 2009.
97. Y.F. Chen, C.F. Kao, T.M. Huang, C.L. Wang, L.J. Lee, and S.C. Wang, "Single-mode oscillation of compact fiber-coupled laser-diode-pumped

Nd:YVO_4/KTP green laser," *IEEE Photon. Technol. Lett.*, vol.9, no.6, pp.740-742, June 1997.

98. K. Mizuuchi, K. Yamamoto, M. Kato, and H. Sato, "Broadening of the phase-matching bandwidth in quasi-phase-matched second-harmonic generation," *IEEE J. Quantum Electron.*, vol.30, no.7, pp. 1596-1603, July 1994.
99. T. Suhara and H. Nishihara, "Theoretical analysis of waveguide second-harmonic generation phase matched with uniform and chirped grating," *IEEE J. Quantum Electron.*, vol.26, no.7, pp. 1265-1276, July 1990.
100. S. Zhu, Y. Zhu, Y. Qin, H. Wang, C. Ge, and N. Ming "Experimental Realization of Second Harmonic Generation in a Fibonacci Optical Superlattice of $LiTaO_3$," *Phys. Rev. Lett.*, vol. 78, 2752–2755 (1997).
101. Q.-Y. Xu, Y. Lu, Y. Gan, X. Li and C.-Q. Xu, "Experimental and theoretical characterization of Nd:YVO_4/PPMgO:LN green lasers," *Proceedings of the SPIE*, vol. 7750, pp. 775016-775016-7, 2010.
102. J. Y. Kim, and J. Shim, "An analytical model of the intracavity optical second harmonic generation in a vertical-external-cavity surface-emitting laser," *IEEE J. Quantum Electron.*, vol.44, no.8, pp. 755-762, Aug. 2008.
103. G. Imeshev, M. Proctor, and M. M. Fejer, "Phase correction in double-pass quasi-phase-matched second-harmonic generation with a wedged crystal," *Opt. Lett.*, vol. 23, no. 3, 165-167, 1998.
104. G. Li, S. Zhao, K. Yang, and J. Zou, "Laser-diode end-pumped passively Q-switched intracavity-frequency-doubling Nd:$GdVO_4$/KTP green laser with GaAs saturable absorber," *IEEE J. Sel. Top. Quantum Electron.*, vol.11, no.3, pp. 638-643, May/Jun. 2005.
105. Y. F. Chen, T. M. Huang, C. F. Kao, C. L. Wang, S. C. Wang, "Optimization in scaling fiber-coupled laser-diode end-pumped lasers to higher power: influence of thermal effect," *IEEE J. Quantum Electron.*, vol. 33 no. 8, pp.1424 – 1429, Aug. 1997.
106. H.-F. Chou, C.-F. Lin, and G.-C. Wang, "An iterative finite difference beam propagation method for modeling second-order nonlinear effects in optical waveguides," *IEEE/OSA J. Lightwave Technol.*, vol. 16, no. 9, pp. 1686-1693, Sept. 1998.
107. P. Laporta and M. Brussard, "Design criteria for mode size optimization in diode-pumped solid-state lasers", *IEEE J. Quantum Electron.*, vol. 27, pp. 2319 - 2326, 1991.
108. M. E. Innocenzi, H. T. Yura, C. L. Fincher, and R. A. Fields, "Thermal modeling of continuous-wave end-pumped solid-state lasers," *Appl. Phys. Lett.*, Vol. 56, No. 19, May 1990, pp. 1831-1833.
109. O. A. Louchev, N. E. Yu, S. Kurimura, and K. Kitamura, "Nanosecond pulsed laser energy and thermal field evolution during second harmonic

generation in periodically poled $LiNbO_3$ crystals," *J. Appl. Phys.*, vol. 98, no. 11, pp.113103, 2005.

APPENDIX A

LIST OF PUBLICATIONS

Journals:

1. **Qing-Yang Xu**, Yi Gan, Yang Lu, Xun Li, and Chang-Qing Xu, "Theoretical Analysis of Intra-Cavity Second-Harmonic Generation of Semiconductor Lasers by a Periodically Poled Nonlinear Crystal Waveguide," accepted by *IEEE J. Quantum Electron.*
2. **Qing-Yang Xu**, Xun Li, Chang-Qing Xu, Wei-Ping Huang, "Modulation crosstalk and reduction in distributed feedback laser diode and monitor photodiode monolithically integrated optical transceivers," *IEEE J. Quantum Electron.*, vol. 46, no 3, pp. 323-31, March 2010.
3. **Qing-Yang Xu**, Minhui Yan, Chang-Qing Xu, and Xun Li, "Direct modulation of multimode fiber Bragg grating external cavity lasers," accepted by *Microwave and Optical Technology Letters.*
4. Yang Lu, **Qingyang Xu**, Yi Gan, and Changqing Xu, "Field-Sequential Operation of Laser Diode Pumped Nd:YVO4/PPMgLN Microchip Green Laser," *IEEE Photon. Electron. Lett.*, vol. 22, no. 13, pp. 990-993, July 2010.
5. Minhui Yan, **Qing-Yang Xu**, Chih-Hung Chen, Wei-Ping Huang, Xiaobin Hong, "Schemes of optical power splitter nodes for direct ONU-ONU intercommunication," *Microwave and Optical Technology Letters*, vol. 51, no. 12, pp. 2814-2817, Dec. 2009.
6. Minhui Yan, Chih-Hung Chen, **Qing-Yang Xu**, Wei-Ping Huang, "A dual continuous- and burst-mode clock recovery module utilizing fiber dispersion," *Microwave and Optical Technology Letters*, vol. 52, no. 8, pp. 1747-1750, Aug. 2010.
7. Minhui Yan, Chih-Hung Chen, **Qing-Yang Xu**, Wei-Ping Huang, "Experimental demonstration of a clock recovery scheme utilizing nonlinear relaxation oscillation in directly modulated lasers," *Microwave and Optical Technology Letters*, vol. 51, no. 7, pp. 1654-1657, July 2009.
8. Hong-Gang Yu, Yong Wang, **Qing-Yang Xu**, Chang-Qing Xu, "Characteristics of multimode fiber Bragg gratings and their influences on external-cavity semiconductor lasers," *J. Lightwave Technol.*, vol. 24, no. 4,

pp. 1903-1912, April 2006.

Conference papers:

9. **Qing-Yang Xu**, Yang Lu, Yi Gan, Xun Li and Chang-Qing Xu, "Experimental and theoretical characterization of Nd:YVO_4/PPMgO:LN green lasers," *Proceedings of the SPIE*, vol. 7750, pp. 775016-775016-7, 2010.
10. **Qing-Yang Xu**, Jian-Wei Mu, Chang-Qing Xu, Xun Li, "Experimental and theoretical characterization of multimode fiber Bragg grating external cavity lasers," *Proceedings of the SPIE*, vol. 7386, pp. 73862O, 2009
11. **Qingyang Xu**, Xiaobin Hong, Wanguo Liang, Xun Li, Chang-Qing Xu, Wei-Ping Huang, "Simulation of crosstalk in integrated distributed feedback laser-photodiode optical transceivers," *Proceedings of the SPIE*, vol. 6343, pp. 63431D-1-9, Sept. 2006.
12. Yang Lu, **Qingyang Xu**, Yi Gan, Changqing Xu, "Compact High Power Modulated Green Laser for Laser Display," *SID 2010*, pp.1170-1172
13. Yang Lu, **Qingyang Xu**, Yi Gan, Changqing Xu, "Over 500 mW Laser-Diode Pumped Green Laser Using Optical Contact Nd:YVO_4/Periodically Poled MgO:$LiNbO_3$ Crystal," *CLEO/QELS 2010*, JTuD110, 2010
14. Xiaobin Hong, **Qingyang Xu**, Wanguo Liang, Weiping Huang, Xun Li, Chang-Qing Xu, "Crosstalk analysis in in-line transceiver," *Proceedings of the SPIE*, vol. 6796, 2008.
15. Hong-Gang Yu, Yong Wang, Chun Yang, **Qing-Yang Xu**, Xiao-Le Yang, Chang-Qing Xu, "Effects of the asymmetric refractive index change profile on the reflection spectra of multimode fiber Bragg gratings," *Proceedings of the SPIE*, vol. 5970, no. 1, pp. 597008-1-8, Sept. 2005.